

ZEOLITE SODIUM Y SYNTHESIZED BY ADDING COGON GRASS FOR  
PARAQUAT ADSORPTION AND BY ADJUSTING WATER CONTENT  
FOR TRANSESTERIFICATION OF PALM OIL



A Thesis Submitted in Partial Fulfillment of the Requirements for the  
Degree of Doctor of Philosophy in Chemistry  
Suranaree University of Technology  
Academic Year 2023

การสังเคราะห์ซีโอไลต์โซเดียมวายเป็นการเติมหน่วยซ้ำสำหรับการดูดซับพาราควอต  
และโดยการปรับปริมาณน้ำสำหรับปฏิกิริยาทรานส์เอสเทอร์ิฟิเคชัน  
ของน้ำมันปาล์ม



นางสาวภควรรณ เสรีรัตนาคกร

วิทยานิพนธ์นี้เป็นส่วนหนึ่งของการศึกษาตามหลักสูตรปริญญาวิทยาศาสตรดุษฎีบัณฑิต

สาขาวิชาเคมี

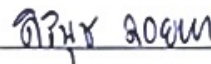
มหาวิทยาลัยเทคโนโลยีสุรนารี

ปีการศึกษา 2566

ZEOLITE SODIUM Y SYNTHESIZED BY ADDING COGON GRASS FOR  
PARAQUAT ADSORPTION AND BY ADJUSTING WATER CONTENT FOR  
TRANSESTERIFICATION OF PALM OIL

Suranaree University of Technology has approved this submitted in partial fulfillment of the requirements for the Degree of Doctor of Philosophy.

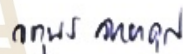
Thesis Examining Committee



---

(Ast. Prof. Dr. Sirinuch Loiha)

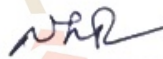
Chairperson



---

(Prof. Dr. Jatuporn Wittayakun)

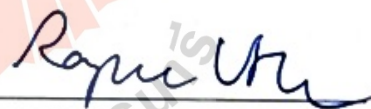
Member (Thesis Advisor)



---

(Assoc. Prof. Dr. Sanchai Prayoonpokarach)

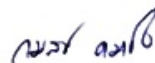
Member (Thesis Co-Advisor)



---

(Assoc. Prof. Dr. Rapee Utke)

Member



---

(Assoc. Prof. Dr. Kamonwad Ngamchuea)

Member



---

(Prof. Dr. Santi Maensiri)

Dean of the Institute of Science



---

(Assoc. Prof. Dr. Yupaporn Ruksakulpiwat)

Vice Rector for Academic Affairs  
and Quality Assurance

ภควรรณ เสรีรัตนาคกร : การสังเคราะห์ซีโอไลต์โซเดียมวายโดยการเติมหญ้าคาสำหรับการดูดซับพาราควอตและโดยการปรับปริมาณน้ำสำหรับปฏิกิริยาทรานส์เอสเทอร์ฟิเคชันของน้ำมันปาล์ม (ZEOLITE SODIUM Y SYNTHESIZED BY ADDING COGON GRASS FOR PARAQUAT ADSORPTION AND BY ADJUSTING WATER CONTENT FOR TRANSESTERIFICATION OF PALM OIL). อาจารย์ที่ปรึกษา : ศาสตราจารย์ ดร.จตุพร วิทยาคุณ, 104 หน้า

คำสำคัญ : ซีโอไลต์วาย หญ้าคา การบำบัดด้วยกรด การดูดซับพาราควอต ทรานส์เอสเทอร์ฟิเคชัน น้ำมันปาล์ม ไบโอดีเซล โพลีเอสเตอร์บิโอดีเซล

งานวิจัยนี้เกี่ยวข้องกับการสังเคราะห์ การระบุลักษณะ และการประยุกต์ใช้ซีโอไลต์โซเดียมวาย (NaY) โดยวิทยานิพนธ์นี้ประกอบด้วยสองส่วนหลัก ในส่วนแรก เป็นการสังเคราะห์ของซีโอไลต์วาย โดยใส่หญ้าคาลงในเจลของซีโอไลต์ ก่อนนำไปตกผลึกแบบไฮโดรเทอร์มอล ส่วนของหญ้าที่เติมเข้าไปประกอบด้วยใบที่ไม่มีการรีฟลักซ์ (Y-NB) ใบที่ผ่านการรีฟลักซ์ด้วยกรด (Y-RB) ต้นที่ไม่มีการรีฟลักซ์ (Y-NT) และต้นที่ผ่านการรีฟลักซ์ด้วยกรด (Y-RT) โดยได้เปรียบเทียบลักษณะทางกายภาพเคมี และรูปร่างของซีโอไลต์กับ NaY จากการสังเคราะห์ปกติโดยไม่ใส่หญ้า (Y-WG) ซึ่งซีโอไลต์ Y-TG Y-RTG และ Y-RG ที่สังเคราะห์ได้มีความเป็นผลึกต่ำกว่าและการกระจายขนาดไม่ดีเท่ากับ Y-NG นอกจากนี้ Y-NG สามารถดูดซับพาราควอตได้มากที่สุดในตัวอย่างี่สังเคราะห์โดยการเติมหญ้าและมากกว่า Y-WG ด้วย

ในส่วนที่สอง เป็นการสังเคราะห์ซีโอไลต์ NaY สามตัวอย่างโดยใช้ความเป็นเบสที่ต่างกันเพื่อผลิตซีโอไลต์ที่มีขนาดเล็กในระดับนาโนเมตร แบบผสม และผลึกขนาดใหญ่ในระดับไมโครเมตร จากนั้นนำไปทำให้เอิบชุ่มด้วยสารละลายบัฟเฟอร์ของโพลีเอสเตอร์บิโอดีเซลเพื่อผลิตตัวเร่งปฏิกิริยาบนตัวรองรับสำหรับการเปลี่ยนน้ำมันปาล์มให้เป็นไบโอดีเซล ตัวเร่งจากซีโอไลต์ขนาดเล็กให้ผลผลิตไบโอดีเซลสูงที่สุด ตามด้วยวัสดุผสมซีโอไลต์และตัวเร่งขนาดไมโครเมตร ตัวเร่งจากซีโอไลต์ที่มีขนาดเล็กทำให้เร่งปฏิกิริยาได้ดี เพราะตัวเร่งและสารตั้งต้นสัมผัสกันได้ดีกว่า

สาขาวิชาเคมี  
ปีการศึกษา 2566

ลายมือชื่อนักศึกษา ภควรรณ เสรีรัตนาคกร  
ลายมือชื่ออาจารย์ที่ปรึกษา จตุพร วิทยาคุณ  
ลายมือชื่ออาจารย์ที่ปรึกษาร่วม นพพร

PAKAWAN SEREERATTANAKORN : ZEOLITE SODIUM Y SYNTHESIZED BY ADDING  
COGON GRASS FOR PARAQUAT ADSORPTION AND BY ADJUSTING WATER  
CONTENT FOR TRANSESTERIFICATION OF PALM OIL. THESIS ADVISOR :  
PROF. JATUPORN WITTAYAKUN, Ph.D. 104 PP.

Keywords: Zeolite Y; Cogon grass; Acid treatment; Paraquat adsorption;  
Transesterification; Palm oil; Biodiesel; Potassium carbonate

This work involved the synthesis, characterization, and application of zeolite sodium Y (NaY). The thesis consisted of two main parts. In the first part, cogon grass was added to the synthesis gel of zeolite Y prior to the hydrothermal crystallization. Parts of the added grass included non-refluxed blade (Y-NB), acid-refluxed blade (Y-RB), non-refluxed trunk (Y-NT), and acid-refluxed trunk (Y-RT). Physicochemical properties and morphology of the obtained zeolites were compared with NaY from the regular synthesis, without the grass addition (Y-WG). The obtained zeolites, including Y-NT, Y-RT, and Y-RB, had lower crystallinity and poorer size distribution than Y-NB. Moreover, Y-NB exhibited the highest paraquat adsorption among grass-added samples, which was higher than Y-WG.

In the second part, three zeolite NaY samples were synthesized with different alkalinity to produce nano-sized, hybrid, and micron-sized crystals. They were further impregnated with potassium acetate buffer solution to produce supported potassium carbonate catalysts for transesterification of palm oil. The catalyst from nano-sized zeolite provided the highest biodiesel yield, followed by zeolite hybrid materials, and micro-sized catalysts. The zeolite with nano-sized crystals was proposed to have better interaction contact between catalyst and reactants.

School of Chemistry

Academic Year 2023

Student's Signature พิกานต์ เสรีรัตน์

Advisor's Signature จตุพร วิฏฐ์

Co-Advisor's Signature วิภา

## ACKNOWLEDGEMENTS

I would like to sincerely appreciate my advisor Prof. Dr. Jatuporn Wittayakun for his enormous knowledge, patience, and mentoring during the degree of my graduate study. Moreover, I would like to greatly acknowledge the thesis committee including Assoc. Prof. Dr. Sanchai Prayoonpokarach, Asst. Prof. Dr. Sirinuch Loiha, Assoc. Prof. Dr. Rapee Utke, and Assoc. Prof. Dr. Kamonwad Ngamchuea for their generous contributions of knowledge and expertise, which have greatly enriched this research.

I am deeply grateful for the financial support provided by the Science Achievement Scholarship of Thailand (SAST). Additionally, I would like to thank Suranaree University of Technology (SUT) for their co-financial support, which enable me to pursue my interested research for six months at University of Louisville (UofL), Louisville, United States of America (USA).

During my overseas research experience, I would like to express my appreciation to Assoc. Prof. Dr. Noppadon Sathitsuksanoh from the Chemical Engineering Department at UofL as well as Dr. Teerawit Prasomsri for their motivation and invaluable guidance throughout the process. I am also thankful to the members of the Advanced Renewable Materials (ARM) Lab Group for their unwavering support.

Thank you to all members of the Material & Catalysis group at SUT for their support and assistance. I also thank HRK, my favorite gamer who always helps me unwind.

Last but not least, I extend heartfelt thanks to my sister, parents, and friends for their love, kind support, and encouragement throughout this journey.

Pakawan Sereerattanakorn

# CONTENTS

	Page
ABSTRACT IN THAI.....	I
ABSTRACT IN ENGLISH.....	II
ACKNOWLEDGEMENTS.....	III
CONTENTS.....	IV
LIST OF TABLES.....	VII
LIST OF FIGURES.....	VIII
LIST OF ABBREVIATIONS.....	XI
<b>CHAPTER</b>	
<b>I INTRODUCTION.....</b>	<b>1</b>
1.1 Research objectives.....	2
1.2 Scope and limitation of the study.....	2
1.3 References.....	3
<b>II LITERATURE REVIEW.....</b>	<b>4</b>
2.1 Zeolite Y.....	4
2.2 Biomass-mediated modification of zeolite.....	6
2.3 Paraquat.....	8
2.4 Biodiesel production through transesterification of palm oil.....	9
2.5 Reference.....	10
<b>III EFFECT OF TRUNK COGON GRASS IN ZEOLITE NaY SYNTHESIS.....</b>	<b>14</b>
3.1 Introduction.....	14
3.2 Experiment.....	15
3.2.1 Material and chemicals.....	15
3.2.2 Acid treatment of cogon grass.....	15

## CONTENTS (Continued)

		Page
	3.2.3 Zeolite NaY synthesis with cogon grass .....	16
	3.2.4 Characterization of samples .....	16
3.3	Result and discussion .....	17
3.4	Conclusions .....	27
3.5	References .....	27
<b>IV</b>	<b>THE SYNTHESIS OF WELL-DISPERED AND UNIFORM-SIZED ZEOLITE NaY BY ADDING NON-REFULXED AND ACID-REFLUXED COGON GRASS .....</b>	<b>31</b>
4.1	Introduction .....	31
4.2	Experiment.....	33
	4.2.1 Material and chemicals.....	33
	4.2.2 Preparation of cogon grass.....	33
	4.2.3 Synthesis of zeolite NaY by adding cogon grass .....	34
	4.2.4 Adsorption of paraquat.....	34
	4.2.5 Characterization of materials.....	35
	4.2.6 Synthesis and characterization of zeolite NaY with various amounts of non-refluxed cogon grass .....	36
	4.2.7 Effect of calcination on adsorption capacity .....	36
4.3	Result and discussion .....	36
	4.3.1 Paraquat adsorption on the zeolite samples .....	36
	4.3.2 Characterization of zeolite samples.....	38
	4.3.3 Characterization of Y-NG with various grass content.....	48
	4.3.4 Characterization and paraquat adsorption of non-calcined and calcined Y-NG .....	52
4.4	Conclusions .....	54
4.5	References .....	54

## CONTENTS (Continued)

	Page
<b>V</b>	
<b>POTASSIUM SUPPORTED ON VARIOUS CRYSTAL SIZES OF ZEOLITE NaY FOR TRANSESTERIFICATION OF PALM OIL .....</b>	<b>59</b>
5.1 Introduction .....	59
5.2 Experiment .....	60
5.2.1 Chemicals .....	60
5.2.2 Zeolite NaY synthesis .....	61
5.2.3 Preparation of catalysts through an ultrasound-assisted impregnation .....	61
5.2.4 Catalysts characterization .....	62
5.2.5 Transesterification of palm oil .....	62
5.2.6 Catalyst stability .....	63
5.2.7 Deactivation of catalysts .....	63
5.3 Result and discussion .....	64
5.3.1 Characterization of catalysts .....	64
5.3.2 Catalytic performance on transesterification .....	76
5.3.3 Stability of catalysts .....	80
5.3.4 Catalytic behavior (active site leaching) .....	83
5.4 Conclusions .....	84
5.5 References .....	84
<b>VI</b>	
<b>CONCLUSIONS.....</b>	<b>88</b>
APPENDICES.....	89
APPENDIX A PARAQUAT ADSORPTION .....	90
APPENDIX B TRANSESTERIFICATION OF PALM OIL .....	93
CURRICULUM VITAE.....	104

## LIST OF TABLES

Table	Page
4.1 The parameters of paraquat adsorption fit with Langmuir and Freundlich models.....	38
4.2 Peak assignments of functional groups of samples.....	41
4.3 Chemical compositions of the internal zeolite NaY particles.....	46
5.1 FTIR peak assignments of functional group of zeolite and potassium species.....	70
5.2 Textural properties of zeolite NaY and the catalyst samples.....	73
5.3 Comparison of transesterification of vegetable oil for biodiesel production on zeolite catalysts from literature and this work.....	79
5.4 EDS element composition of fresh and spent catalysts.....	83



## LIST OF FIGURES

Figure	Page
2.1	Structure of zeolite Y and its micropore system and dimension.....5
2.2	Self-assembly mechanism of bio-source directing agent.....7
2.3	Structure of paraquat.....8
2.4	Relationship between the adsorption capacity of paraquat And zeolite crystallinity.....9
2.5	The production of biodiesel through transesterification of triglycerides and methanol.....10
3.1	XRD pattern and FTIR spectra of non-refluxed trunk (NT), acid-refluxed trunk (RT), and NaOH soaked samples (SNT and SRT).....18
3.2	SEM images of NT (a,b), RT (c,d), RNT (e,f), and SRT (g,h) in different magnification.....19
3.3	TGA (a) and DTG (b) curves of NT and modified NT..... 20
3.4	XRD pattern of zeolite NaY using non-refluxed trunk (Y-NT) and acid-treated trunk (Y-RT)..... 21
3.5	SEM images of Y-NT in different magnifications ..... 22
3.6	SEM images of Y-RT in different magnifications.....23
3.7	SEM images and EDS mapping of Y-NT.....24
3.8	SEM images and EDS mapping of Y-RT.....25
3.9	Nitrogen adsorption desorption isotherm of Y-NT and RT; filled symbols = adsorption and hollow symbols = desorption.....26
4.1	Adsorption of paraquat on Y-WG, Y-NB, and Y-RB.....37

## LIST OF FIGURES (Continued)

Figure	Page
4.2 XRD pattern of NaY with refluxed blade (Y-RB) and non-refluxed blade (Y-NB) compared with the original zeolite NaY (Y-WG) .....	39
4.3 XRD pattern (a) and FTIR spectra (b) of non-refluxed (NB), acid-refluxed (RB), and NaOH-soaked blade samples (SNB and SRB) .....	40
4.4 FTIR spectra of Y-WG, Y-NB, and Y-RB.....	42
4.5 SEM images of Y-WG (a-c), Y-NB (d-f), and Y-RB (g-i).....	44
4.6 EDS spectrum of Y-WG (a), Y-NB (b), and Y-RB (c).....	44
4.7 SEM images and EDS spectrum of Y-NB (a-c) and calcined Y-NB (d-f) .....	45
4.8 EDS spectrum of the sponge-like amorphous core of Y-NB: before (a) and after calcination (b) .....	46
4.9 Nitrogen adsorption-desorption isotherm and textural properties of Y-WG, Y-NB, and Y-RB; filled symbols = adsorption, and hollow symbols = desorption. Micropore volume was calculated by the <i>t</i> -plot method .....	47
4.10 XRD pattern of Y-NB synthesized with various grass content.....	48
4.11 SEM images of Y-0.5NB (a-c), Y-1.5NB (d-f), and Y-2.0NB (g-i).....	50
4.12 EDS spectra of Y-0.5NB (a), Y-1.5NB (b,c), and Y-2.0NB (d-f).....	50
4.13 TGA (a) and DTG (b) curves of Y-NB with various grass content .....	51
4.14 XRD patterns of non-calcined and calcined YNB (a) and paraquat adsorption of Y-NB and Y-WG from various initial concentrations (b) .....	53
5.1 TGA/DTG (a-c) and TGA/DSC (e-f) curves of impregnated NaY in various crystal sizes.....	64
5.2 XRD patterns of impregnated (blue line) and calcined K/NaY (red line) compared with bare NaY (black line) on K/NaY0.25 (a), K/NaY1.0 (b), and K/NaY2.0 (c) .....	66

## LIST OF FIGURES (Continued)

Figure	Page
5.3	FTIR spectra of impregnated (blue line) and calcined K/NaY (red line) compared with bare NaY (black line) on K/NaY0.25 (a), K/NaY1.0 (b), and K/NaY2.0 (c) ..... 67
5.4	XRD patterns of bare zeolite (black line) compared with calcined zeolite NaY (red line) on K/NaY0.25 (a), K/NaY1.0 (b), and K/NaY2.0 (c) ..... 69
5.5	SEM images of NaY0.25 (a,b) and K/NaY0.25 (c,d) with different magnitudes including x10k and x30k ..... 71
5.6	SEM images of NaY1.0 (a,b) and K/NaY1.0 (c,d) with different magnitudes including x10k and x30k ..... 72
5.7	SEM images of NaY2.0 (a,b) and K/NaY2.0 (a,b) with different magnitudes including x10k and x30k ..... 72
5.8	Nitrogen adsorption-desorption isotherm of zeolite NaY in various sizes and the catalyst samples ..... 74
5.9	HRTEM images of commercial zeolite NaY (a,b), K/NaY0.25 (c,d) and K/NaY1.0 (e,f) in different magnification ..... 75
5.10	Biodiesel yield from first and second runs on K/NaY0.25, K/NaY1.0, and K/NaY2.0 at 60 °C for 3 h ..... 77
5.11	GC chromatograms of biodiesel products from transesterification of palm oil obtained from (a,b) K/NaY0.25 (1 <sup>st</sup> and 2 <sup>nd</sup> runs), (c,d) K/NaY1.0 (1 <sup>st</sup> and 2 <sup>nd</sup> runs), and (e,f) K/NaY2.0 (1 <sup>st</sup> and 2 <sup>nd</sup> runs) ..... 77
5.12	Comparison of fresh and spent catalysts by FTIR spectra of K/NaY0.25 (a), K/NaY1.0 (b), and K/NaY2.0 (c) ..... 81
5.13	SEM images of spent K/NaY0.25 (a,b), K/NaY1.0 (c,d), and K/NaY2.0 (e,f) ..... 82
5.14	Biodiesel yield of transesterification in first run and leaching test ..... 83

## LIST OF ABBREVIATIONS

FAU	= Faujasite framework
XRD	= X-ray diffraction
FTIR-ATR	= Fourier transform infrared spectroscopy using attenuated total reflectance mode
TGA	= Thermogravimetric analysis
DTG	= Derivative thermogravimetry
DSC	= Differential scanning calorimetry
FE-SEM/EDX	= Field-emission scanning electron microscope with energy-dispersive X-ray spectroscopy
BET	= Brunauer–Emmett–Teller
UV-Vis	= Ultraviolet-Visible
GC-FID	= Gas chromatography equipped with a flame ionization detector

# CHAPTER I

## INTRODUCTION

This thesis focuses on modifying zeolite NaY for adsorption and catalysis. The literature review (Chapter II) provides introduction of zeolite, the incorporation of biomass in zeolite synthesis, paraquat adsorption, the preparation of heterogeneous catalysts, and the detailed condition of the transesterification reaction.

The thesis is divided into two main parts. The first part (Chapter III and IV) involves the crystallization of zeolite NaY with an addition of cogon grass. The synthesis with an addition of trunk and blade grass is compared. Moreover, the influence of acid treatment on the grass is studied. Acid-refluxed trunk (RT) and non-refluxed trunk (NT) hinder zeolite intergrowth, resulting in mixed phases of zeolite crystal and amorphous phase in Y-RT and Y-NT. The grass component has a crucial role in the zeolite formation process. Thus, the effect of blade grass and blade content are further investigated. Moreover, paraquat adsorption is utilized as an indicator to discern the crystallinity and chemical composition.

The second part of this thesis (Chapter V) involves the application of zeolite with different crystal sizes and phases as support materials for potassium catalysts. The supported catalysts are employed in transesterification to produce biodiesel. The study examines the impact of different crystal sizes on catalytic performance. This part further investigates the catalyst reusability and the active site leaching. By analyzing the samples, an array of techniques is employed to characterize the as-prepared, fresh, and spent catalysts, providing insight into their roles.

## 1.1 Research objectives

The aims of this research are outlined as follows:

1. To synthesize and characterize zeolite NaY by adding cogon grass.
2. To investigate the role of trunk and blade grass in zeolite synthesis.
3. To explore the impact of untreated and acid-treated grass on zeolite synthesis and subsequent properties.
4. To prepare zeolite NaY catalysts varying in size and morphology and assess their active sites for the transesterification of palm oil.

## 1.2 Scope and limitation of the study

Cogon grass was divided into trunk and blade. Both grasses were treated with 3 M HCl following the procedure by Bunmai et al. (2018). All grass samples were utilized in the zeolite NaY synthesis. This process was adapted from the literature (Mintova, 2016). Chapter III focused on the existence of trunk and acid-treated trunk. Apart from trunk samples, Chapter IV illustrated the effect of blade and acid-treated blade.

In addition to Chapter IV, a synthesized zeolite NaY incorporating blade grass was employed as an adsorbent for the paraquat solution. The procedure followed the conditions in the methods reported by Rongchapo et al. (2013) and Keawkumay et al. (2019). This process was carried in a water bath to maintain a temperature of 29 °C.

In the Chapter V, nano-sized, hybrid, and micron-sized crystals of zeolite NaY were synthesized, adjusting the water contents using a method modified from Keawkumay et al. (2019). The as-prepared catalysts were prepared using an ultrasound-assisted impregnation method with 12 wt.% of potassium acetate buffers as a precursor. The conversion of palm oil through the transesterification reaction was carried out in a reflux setup at the operating temperature of 60 °C for 3 h, following the method described in the literature by Rakmae et al. (2016) and Kosawatthanakun et al. (2019).

### 1.3 References

- Ardiwinata, A. N., Harsanti, E. S., Kurnia, A., Sulaeman, E., Fauriah, R., and Paputri, D. M. W. (2019). Contamination of paraquat residues in soil and water from several provinces in Indonesia, AIP Conf., AIP Publishing, 2120 (1).
- Ayub, A., Raza, Z. A., Majeed, M. I., Tariq, M. R., and Irfan, A. (2020). Development of sustainable magnetic chitosan biosorbent beads for kinetic remediation of arsenic contaminated water. *Int. J. Biol. Macromol.*, 163, 603-617.
- Bunmai, K., Osakoo, N., Deekamwong, K., Rongchapo, W., Keawkumay, C., Chanlek, N., Prayoonpokarach, S., and Wittayakun, J. (2018). Extraction of silica from cogon grass and utilization for synthesis of zeolite NaY by conventional and microwave-assisted hydrothermal methods. *J. Taiwan Inst. Chem. Eng.*, 83, 152-158.
- Keawkumay, C., Rongchapo, W., Sosa, N., Suthirakun, S., Koleva, I. Z., Aleksandrov, H. A., Vayssilov, G. N., and Wittayakun, J. (2019). Paraquat adsorption on NaY zeolite at various Si/Al ratios: A combined experimental and computational study. *Mater. Chem. Phys.*, 238.
- Kosawatthanakun, S., Pansakdanon, C., Sosa, N., Chanlek, N., Roessner, F., Prayoonpokarach, S., and Wittayakun, J. (2022). Comparative Properties of K/NaX and K/NaY from Ultrasound-Assisted Impregnation and Performance in Transesterification of Palm Oil. *ACS Omega*, 7(11), 9130-9141.
- Mintova, S. (Editor) (2016). Verified synthesis of zeolitic materials. *The Synthesis Commission of the International Zeolite Association*, 215-223.
- Rakmae, S., Keawkumay, C., Osakoo, N., Montalbo, K. D., de Leon, R. L., Kidkhunthod, P., Chanlek, N., Roessner, F., Prayoonpokarach, S., and Wittayakun, J. (2016). Realization of active species in potassium catalysts on zeolite NaY prepared by ultrasound-assisted impregnation with acetate buffer and improved performance in transesterification of palm oil. *Fuel*, 184, 512-517.
- Rongchapo, W., Sophiphun, O., Rintramee, K., Prayoonpokarach, S., and Wittayakun, J. (2013). Paraquat adsorption on porous materials synthesized from rice husk silica. *Water Sci. Technol.*, 68(4), 863-869.

## CHAPTER II

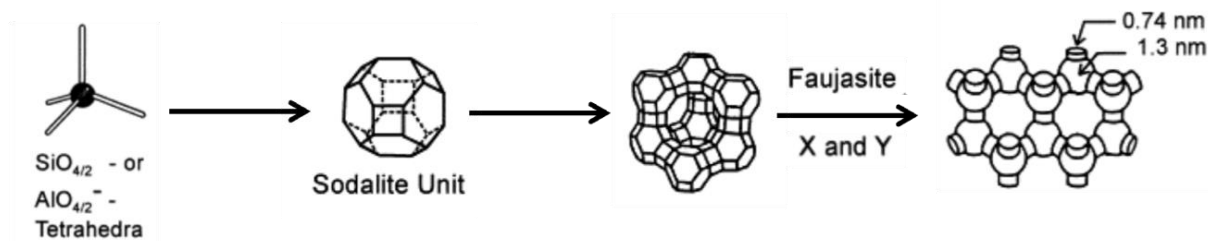
### LITERATURE REVIEW

This literature review emphasizes the synthesis and development of zeolite Y and briefly presents the basis of its formation. It also discusses the modification of synthesized zeolite using renewable biomass and reviews the background of paraquat. Additionally, it notes the preparation conditions of the catalyst for transesterification.

#### 2.1 Zeolite Y

Zeolites are crystalline aluminosilicate. A three-dimensional network structure composes of a porous framework built from  $[\text{AlO}_4]^{5-}$  and  $[\text{SiO}_4]^{4-}$  tetrahedral. Adjacent tetrahedrals are linked through the sharing of oxygen atoms at the corners of each tetrahedral (Feijen et al., 1994; Weitkamp, 2000; Jha et al., 2016).

Zeolite Y is a faujasite-type framework (FAU) topology. Sodalite cages are arranged to create spherical supercages with a diameter of 1.3 nm. Additionally, there is a large cavity comprised of a 12-membered oxygen ring with a diameter approximately 0.74 nm, as shown in **Scheme 2.1**. Zeolite Y is considered one of the most highly desirable materials for various industries including catalysis, adsorption, and ion exchange due to its big cavity, high surface area, and pore volume (Weitkamp, 2000; Mohamed et al., 2015; Reinoso et al., 2018; Mu et al., 2019).



**Scheme 2.1** Structure of zeolite Y and its micropore systems and dimensions (adapted from Weitkamp, 2000).

In zeolite structure, the partial substitute of silicon atom by aluminum atom leads to the introduction of a negative charge into the framework. These negative sites are balanced by counterions to maintain charge neutrality, such as sodium ( $\text{Na}^+$ ), located elsewhere in the structure. The role of  $\text{Na}^+$  cation is a charge balancing. They also can be exchanged with others without damaging the zeolite framework. Examples of these include new cations (potassium, calcium, etc.), water molecules, and organic compounds (Jha et al., 2016; Moshoeseshoe et al., 2017). This enables a significant ion exchange ability. Nevertheless, this behavior is determined by the chemical composition and the crystalline structures of the zeolite.

The tailoring topology and properties of zeolite are typically obtained using chemical additives such as TMAOH, *tert*-butanol, and DOAC (Liu et al., 2013; Zhao et al., 2016; Parsapur and Selvam, 2018). In fact, this poses inherent challenging in term of green chemistry due to its costs and toxicity. Hence, the use of natural additives could provide motivation for more sustainable approaches.

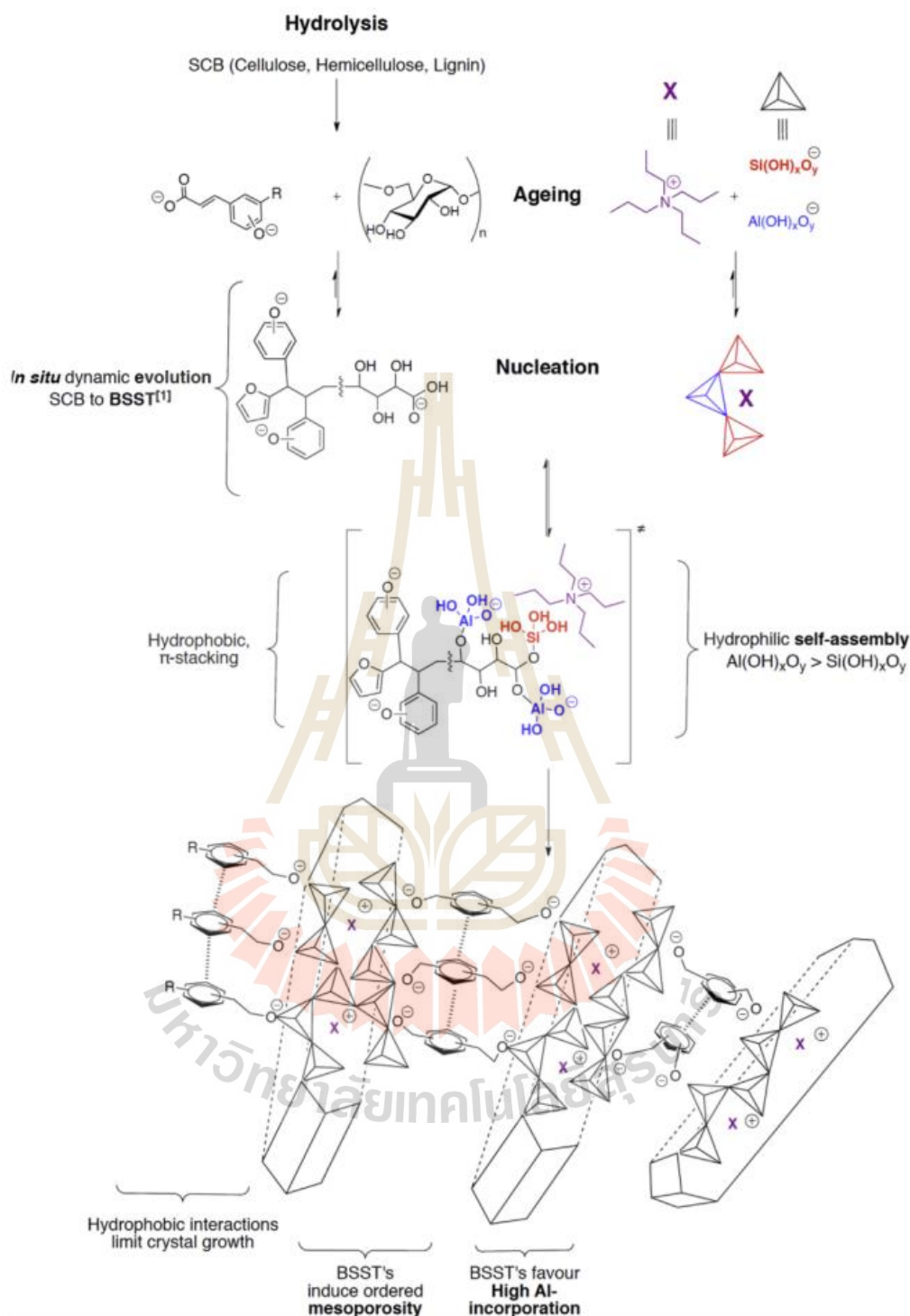
## 2.2 Biomass-mediated modification of zeolite

Previous research groups have emphasized the production of a new morphology for various zeolites using sugarcane bagasse residue. They reported that evidence of a positive impact of biomass in the zeolite morphology and properties.

Louis et al. (2016) and Louis et al. (2017) prepared FAU zeolite in the presence and absence of bagasse. The GIS structure was observed after few hours upon without biomass. Following the synthesis in the presence of biomass, a GIS structure was obtained after 120 h. Biomass residue slows the phase transition of FAU to GIS in short period. Moreover, bagasse has an influence on crystal size, shape, and chemical composition.

Gomes et al. (2017) and Pereira et al. (2018) reported that an alkaline hydrolysis of lignocellulosic biomass usually releases saccharide, degraded sugars, and aromatic lignin products. During aging in alkaline media, those molecules are evolved to form the bio-source directing agent consisting of hydroxyl group (hydrophobic site) and organic molecule (hydrophilic site). These molecules are attached to the zeolite precursors by hydroxyl groups. At the self-assembly process, the organic species limit crystalline growth, leading to control the zeolite particle as illustrated in **Scheme 2.2**.

However, the existence of lignin prohibits the zeolite crystallization (Ocampo et al., 2010; Gomes et al., 2018). Flores et al. (2022) demonstrated that the influence of lignin in MFI synthesis. They observed that ZSM-5 achieved 99% relative crystallinity after 16 h, whilst the use of lignin resulted in 85% crystallinity after 24 h. Thus, alternative biomass with a low lignin content will be utilized for synthesis of zeolite Y in this work.



**Scheme 2.2** Self-assembly mechanism of bio-source directing agent (reprinted with permission from Gomes et al., 2017).

## 2.3 Paraquat

Herbicide paraquat (1,1'-dimethyl-4,4'-bipyridyl dichloride), as shown in **Figure 2.3**, is widely used in global agriculture due to its high efficiency, low cost, and non-selectivity. It is currently banned in more than 50 countries including Thailand in 2020 (Sakchai, 2020; Franco et al., 2022). Paraquat is highly solubility in water at ambient temperature, residue in the environment, and easily enters the food chain of mammals. For humans, it has high toxicity and can damage to lungs, kidneys, and liver of an organism (Berry et al., 2010). In addition, it is also associated with Parkinson's disease (Bastías-Candia et al., 2019).

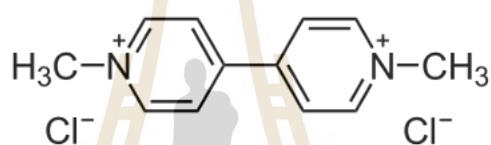


**Figure 2.3** Structure of paraquat.

Several Si-based adsorbents have been studied for paraquat elimination in water, including amorphous SiO<sub>2</sub> (Rongchapo et al., 2013), mesoporous materials (Rongchapo et al., 2015), natural zeolite (Ibrahim and Jbara, 2009), synthetic zeolite (Insuwan and Rangriwatananon, 2017; Osakoo et al., 2017), and activated carbon (Mueanpun et al., 2021). Among those adsorbents, zeolite NaY has attracted wide attention due to its large surface area and Al content, leading to excellent adsorption capacity (Rongchapo et al., 2013; Rongchapo et al., 2015). However, NaY with higher Si/Al has strong crystallinity according to Keawkumay et al. (2019). They reported that the adsorption capacity increased with high crystallinity of zeolite as illustrated in **Figure 2.4**. Hence, the adsorption of paraquat will be further developed to indicate the zeolite topology, crystallinity, and chemical composition.

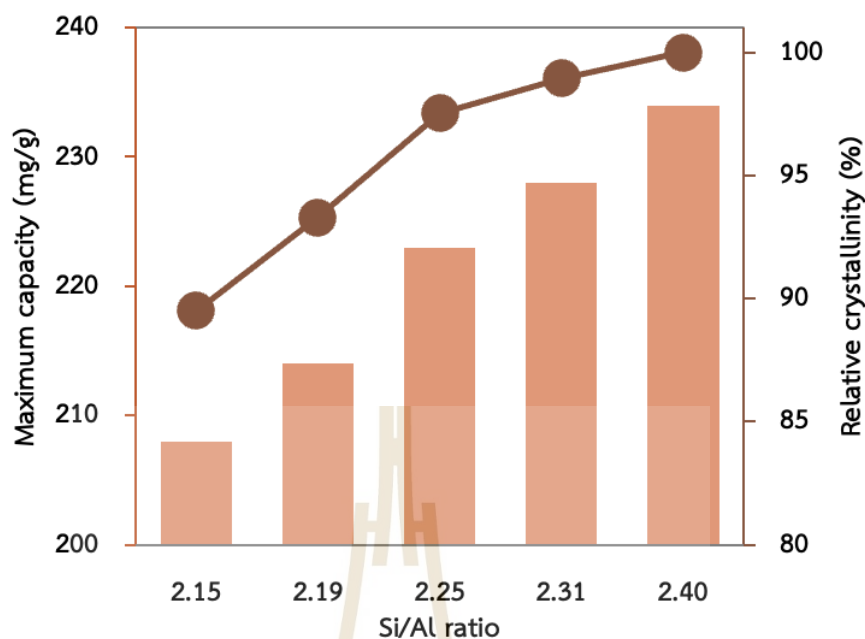
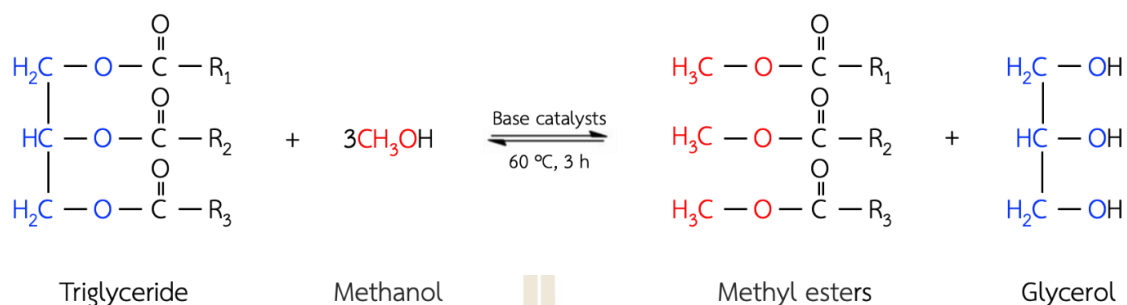


**Figure 2.4** Relationship between the adsorption capacity of paraquat and zeolite crystallinity (adapted from Keawkumay et al., 2019).

## 2.4 Biodiesel production through transesterification of palm oil

Biodiesel is referred to fatty acid methyl esters (FAME) and is usually produced by transesterification process between triglyceride and methanol, as seen in **Scheme 2.5**. During a reaction, vegetable oil, such as palm oil, is transformed using base catalyst over a period of time. Besides, the basicity of catalysts is the predominant effect on the triglyceride conversion. Supamathanon et al. (2011) provided the potassium carbonate supported on NaY (K/NaY) with various loading of 4, 8, and 12 wt.%. The catalysts were prepared by impregnation a potassium acetate buffer solution. The best catalyst was 12K/NaY. It showed 73.4% of biodiesel yield from the reaction time 3 h. Montalbo et al. (2013) demonstrated the 12K/NaY samples that used acetate (A) and acetate buffer (B) as a potassium precursor. The 12K/NaY-B indicated that the zeolite structure was preserved. The yield of biodiesel was 77.2% for 3 h at 65 °C. Moreover, Rakmae et al. (2016) reported the preparation of a catalyst through ultrasound-assisted impregnation using 12 wt.% potassium on NaY from an acetate buffer. This technique promotes better dispersion of potassium carbonate than conventional method. Similarly, Kosawattanakun et al. (2022) confirmed that this catalyst preparation enhanced catalytic performance. The yield from 12K/NaY increased up to 94.4%.

Therefore, 12 wt.% of potassium carbonate from potassium acetate buffer by using ultrasound-assisted impregnation is applied for my catalyst preparation in this work.



**Scheme 2.5** The production of biodiesel through transesterification of triglycerides and methanol.

## 2.5 References

- Alam, T., Krisnandi, Y. K., Wibowo, W., Nurani, D. A., Rahayu, D. U. C., and Haerudin, H. (2018). Synthesis and characterization hierarchical HY zeolite using template and non template methods. *AIP Con. Proc.* 2023, 020094 (2018).
- Bastias-Candia, S., Zolezzi, J. M., and Inestrosa, N. C. (2019). Revisiting the paraquat-Induced sporadic Parkinson's disease-like Model. *Mol. Neurobiol.*, 56(2), 1044-1055.
- Berry, C., La Vecchia, C., and Nicotera, P. (2010). Paraquat and Parkinson's disease. *Cell Death Differ.*, 17(17), 1115-1125.
- Feijen, E. J., Martens, J. A., and Jacobs, P. A. (1994). Zeolites and their mechanism of synthesis. *Stud. Surf. Sci. Catal.*, 84, 3-21.
- Flores, C. G., Schneider, H., and Louis, B. (2022). Lignin as a bio-sourced secondary template for ZSM-5 zeolite synthesis. *Catalysts*, 12(4), 368.
- Franco, D. S. P., Georjgin, J., Lima, E. C., and Silva, L. F. O. (2022). Advances made in removing paraquat herbicide by adsorption technology: A review. *J. Water Process. Eng.*, 49, 102988.
- Gomes, E. S., Aranda, D. A. G., Pereira, M. M., and Louis, B. (2018). ZSM-5 synthesis by the assistance of biomass and biomass-derivate compounds. *Microporous Mesoporous Mater.*, 263, 251-256.

- Gomes, E. S., Lutzweiler, G., Losch, P., Silva, A. V., Bernardon, C., Parkhomenko, K., Pereira, M. M., and Louis, B. (2017). Strategy to design zeolite catalysts in the presence of biomass. *Microporous Mesoporous Mater.*, 254, 28-36.
- Ibrahim, K. M., and Jbara, H. A. (2009). Removal of paraquat from synthetic wastewater using phillipsite-faujasite tuff from Jordan. *J. Hazard. Mater.*, 163(1), 82-86.
- Jha, B., Singh, D. N., Jha, B., and Singh, D. N. (2016). *Fly ash zeolites: Innovations, applications, and directions*. Singapore: Springer, 78, 5-31.
- Insuwan, W., and Rangriwatananon, K. (2017). Removal of paraquat from aqueous solutions onto zeolite LTL. *Eng. J.*, 21(2), 15-23.
- Keawkumay, C., Rongchapo, W., Sosa, N., Suthirakun, S., Koleva, I. Z., Aleksandrov, H. A., Vayssilov, G. N., and Wittayakun, J. (2019). Paraquat adsorption on NaY zeolite at various Si/Al ratios: A combined experimental and computational study. *Mater. Chem. Phys.*, 238, 121824.
- Kosawatthanakun, S., Pansakdanon, C., Sosa, N., Chanlek, N., Roessner, F., Prayoonpokarach, S., and Wittayakun, J. (2022). Comparative properties of K/NaX and K/NaY from ultrasound-assisted impregnation and performance in transesterification of palm oil. *ACS Omega*, 7(11), 9130-9141.
- Liu, X., Zhang, X., Chen, Z., and Tan, X. (2013). Hydrothermal synthesis of zeolite Rho using methylcellulose as the space-confinement additive. *Ceram. Int.*, 39(5), 5453-5458.
- Louis, B., Gomes, E. S., Coelho, T., Lutzweiler, G., Losch, P., Silva, A. V., Faro, A. C., Romero, T., Osman, M. B., Balanqueux, A., Bernardon, C., and Pereira, M. M. (2016). Influence of biomass residues on the metastability of zeolite structures. *Nanosci. Nanotechnol. Lett.*, 8(11), 917-923.
- Louis, B., Gomes, E. S., Losch, P., Lutzweiler, G., Coelho, T., Faro, A., Pinto, J. F., Cardoso, C. S., Silva, A. V., and Pereira, M. M. (2017). Biomass-assisted zeolite syntheses as a tool for designing new acid catalysts. *ChemCatChem*, 9(12), 2065-2079.
- Mohamed, R. M., Mkhalid, I. A., and Barakat, M. A. (2015). Rice husk ash as a renewable source for the production of zeolite NaY and its characterization. *Arab. J. Chem.*, 8(1), 48-53.

- Montalbo, K. D., Leon, R. L. d., Sophiphun, O., Manadee, S., Prayoonpokarach, S., and Wittayakun, J. (2013). Characterization and catalytic performance of potassium loaded on rice husk silica and zeolite nay for transesterification of jatropha seed oil. *Quím. Nova*, *36*, 1116-1120.
- Moshoeshoe, M., Nadiye-Tabbiruka, M. S., and Obuseng, V. (2017). A review of the chemistry, structure, properties and applications of zeolites. *Am. J. Mater. Sci.*, *7*(5), 196-221.
- Mu, L., Feng, W., Zhang, H., Hu, X., and Cui, Q. (2019). Synthesis and catalytic performance of a small crystal NaY zeolite with high SiO<sub>2</sub>/Al<sub>2</sub>O<sub>3</sub> ratio. *RSC Adv.*, *9*(36), 20528-20535.
- Ocampo, F., Cunha, J. A., de Lima Santos, M. R., Tessonnier, J. P., Pereira, M. M., and Louis, B. (2010). Synthesis of zeolite crystals with unusual morphology: Application in acid catalysis. *Appl. Catal. A: Gen.*, *390*(1-2), 102-109.
- Osakoo, N., Pansakdanon, C., Sosa, N., Deekamwong, K., Keawkumay, C., Rongchapo, W., Chanlek, N., Jitcharoen, J., Prayoonpokarach, S., and Wittayakun, J. (2017). Characterization and comprehension of zeolite NaY/mesoporous SBA-15 composite as adsorbent for paraquat. *Mater. Chem. Phys.*, *193*, 470-476.
- Parsapur, R. K., and Selvam, P. (2018). Rational design, synthesis, characterization and catalytic properties of high-quality low-silica hierarchical FAU-and LTA-type zeolites. *Sci. Rep.*, *8*(1), 16291.
- Pereira, M. M., Gomes, E. S., Silva, A. V., Pinar, A. B., Willinger, M. G., Shanmugam, S., Chizallet, C., Laugel, G., Losch, P., and Louis, B. (2018). Biomass-mediated ZSM-5 zeolite synthesis: when self-assembly allows to cross the Si/Al lower limit. *Chem. Sci.*, *9*(31), 6532-6539.
- Rakmae, S., Keawkumay, C., Osakoo, N., Montalbo, K. D., de Leon, R. L., Kidkhunthod, P., Chanlek, N., Roessner, F., Prayoonpokarach, S., and Wittayakun, J. (2016). Realization of active species in potassium catalysts on zeolite NaY prepared by ultrasound-assisted impregnation with acetate buffer and improved performance in transesterification of palm oil. *Fuel*, *184*, 512-517.
- Reinoso, D., Adrover, M., and Pedernera, M. (2018). Green synthesis of nanocrystalline faujasite zeolite. *Ultrason. Sonochem.*, *42*, 303-309.

- Rongchapo, W., Sophiphun, O., Rintramee, K., Prayoonpokarach, S., and Wittayakun, J. (2013). Paraquat adsorption on porous materials synthesized from rice husk silica. *Water Sci. Technol.*, 68(4), 863-869.
- Sakchai Preechajarn, A. S. (2020). *Economic Impact of the Ban on Paraquat and Chlorpyrifos on Thai Industries*.  
[https://apps.fas.usda.gov/newgainapi/api/Report/DownloadReportByFileName?fileName=Economic%20Impact%20of%20the%20Ban%20on%20Paraquat%20and%20Chlorpyrifos%20on%20Thai%20Industries%20\\_Bangkok\\_Thailand\\_05-27-2020](https://apps.fas.usda.gov/newgainapi/api/Report/DownloadReportByFileName?fileName=Economic%20Impact%20of%20the%20Ban%20on%20Paraquat%20and%20Chlorpyrifos%20on%20Thai%20Industries%20_Bangkok_Thailand_05-27-2020) (accessed on 2 January 2024).
- Supamathanon, N., Wittayakun, J., and Prayoonpokarach, S. (2011). Properties of Jatropha seed oil from Northeastern Thailand and its transesterification catalyzed by potassium supported on NaY zeolite. *J. Ind. Eng. Chem.*, 17(2), 182-185.
- Weitkamp, J. (2000). Zeolites and catalysis. *Solid State Ion.*, 131(1-2), 175-188.
- Zhao, J., Yin, Y., Li, Y., Chen, W., and Liu, B. (2016). Synthesis and characterization of mesoporous zeolite Y by using block copolymers as templates. *Chem. Eng. J.*, 284, 405-411.



## CHAPTER III

### EFFECT OF TRUNK COGON GRASS IN ZEOLITE NaY SYNTHESIS

#### 3.1 Introduction

Zeolite NaY is a three-dimensional structure, which is a part of the FAU framework structure. It is mostly applied as adsorbent (Rongchapo et al., 2013; Keawkumay et al., 2019; Kulawong et al., 2020) and catalyst (Rakmae et al., 2016; Kosawatthanakun et al., 2020) because of its crystal size, structure, and chemical composition. The synthesis process is a challenging task in order to facilitate control of their properties.

The use of an additive is widespread for tailoring zeolite properties via a one-pot synthesis. An additive induces the aggregation of the precursor molecules and nucleation of the zeolite particles (Lewis et al., 1995). Recently, Louis's research group has emphasized the production of a new morphology for MFI zeolite using sugarcane bagasse residue (Ocampo et al., 2010; Louis et al., 2016; Louis et al., 2017). They reported that biomass easily impacted the direction of the crystal growth and zeolite formation. In parallel, Pereira et al. (2018) demonstrated that the bagasse was hydrolyzed under base condition to form structure directing agents (SDA) consisting of hydrophilic site (hydroxyl group) and hydrophobic site (organic species). The hydroxyl groups potentially work as binding sites for zeolite precursors (Valtchev et al., 1994; Mintova et al., 1996). SDA prefers the interaction of aluminates over silicates, resulting in a higher Al content in the final product (Gomes et al., 2018; Pereira et al., 2018).

Cogon grass (*Imperata Cylindrica*) is a widespread weed found in various regions worldwide particularly in countries such as Thailand, Indonesia, and USA (Holzmueller and Jose, 2011; Surtiningsih et al., 2018). Cogon grass is considered useless and priceless, leading to its common disposal through burning. It impacts on agricultural and ecological health (Estrada and Flory, 2015). Notable, Bunmai et al. (2018) have highlighted the potential of cogon grass as an alternative silica source.

It has been observed that trunk of cogon grass contains significant silica content, yielding approximately 4 wt.%. This potential alternative use could provide not only economic benefits but also contribute to environmental sustainability.

Hence, the goal of this study is to investigate the synthesis of zeolite using trunk grass. Both untreated and modified grass are examined to assess the impact of acid treatment, alkaline hydrolysis, and the presence of organic components in the synthesis gel.

## 3.2 Experiment

### 3.2.1 Material and chemicals

Cogon grass was gathered at the Suranaree University of Technology (Nakhon Ratchasima, *Thailand*). Chemicals employed in this work were hydrochloric acid (37 %w/v HCl, RCI Labscan, Bangkok, *Thailand*), fumed silica (99.8%, Sigma-Aldrich, *USA*), sodium aluminate (95 %w/w NaAlO<sub>2</sub>, Sigma-Aldrich, *St. Louis, USA*), and sodium hydroxide (97 %w/w NaOH, Carlo Erba, *Germany*).

### 3.2.2 Acid treatment of cogon grass

Fresh cogon grass was cleaned in running water and washed with deionized water (DI) to remove the soil and dust. Then cut it into 0.5 cm in length. Trunk grass or non-refluxed trunk (NT) was dried in an oven at 90 °C for 3 days. Conditions for acid treatment were modified from Bunmai et al. (2018). A 5.0 g of dried NT was refluxed in 67.0 mL of 3.0 M HCl solution at 90 °C for 6 h, cooled down, and filtered. Then acid-refluxed trunk (RT) was washed with DI water until the pH became natural and dried at 90 °C for 24 h.

### 3.2.3 Zeolite NaY synthesis with cogon grass

The synthesis of zeolite NaY was adapted procedure from Keawkumay et al. (2019). At the beginning, 1.0 g of the grass samples (NT or RT) were soaked in 10.0 mL of 2.5 M NaOH for 24 h in centrifuge tube of 15 mL. The samples were labeled as SNT and SRT, respectively. Afterward, the sodium silicate ( $\text{Na}_2\text{SiO}_3$ ) was prepared by slowly adding 28.7 g of fumed silica in NaOH solution (a 11.5 g of NaOH pellet is dissolved in 59.8 g of DI water) with vigorously stirring on water bath at 50-60 °C until clear solution. A seed gel was prepared by following these steps. A 0.4 g of  $\text{NaAlO}_2$  was added in base hydrolysate solution, which stirred until homogeneous gel is obtained. In addition, a 4.8 g of  $\text{Na}_2\text{SiO}_3$  was moderately dropped in the mixture under stirring and continue stirred for 15 minutes. After that it was aged at room temperature for 24 h.

A feedstock gel was performed by liquefying 0.035 g of NaOH in 22.3 g of DI water. Then 2.8 g of  $\text{NaAlO}_2$  was added, stirred, and 30.2 g of  $\text{Na}_2\text{SiO}_3$  were dropped. This gel was used immediately without aging. A feed gel was gently added to seed gel with vigorously stirring until the gel is smooth. The overall gel was capped and crystallized at 90 °C for 24 h. After the hydrothermal, the sample was wash with DI water until natural (pH 7). Finally, zeolite NaY (Y-NT or Y-RT) are dried in an oven at 90 °C for 24 h.

### 3.2.4 Characterization of samples

X-ray diffraction (XRD) patterns of grass samples and synthesized zeolites were acquired X-ray diffraction (XRD, Bruker D8 ADVANCE, Billerica, USA) with  $\text{Cu K}\alpha$  radiation diffractometer operated at 40 kV and 40 mA. XRD patterns were recorded in the  $2\theta$  at 5 - 50° range with a step size of 0.5 s/step and increment of 2.0 s/step.

The functional groups in grass samples were obtained in 4000 to 400  $\text{cm}^{-1}$  regions using Attenuated Total Reflectance (ATR mode) with a Fourier Transform Infrared Spectrometer (FT-IR, Bruker Tensor 27, Ettlingen, Germany).

The textural properties were determined by nitrogen adsorption-desorption isotherm (BelSorp mini II, Microtrac, Pennsylvania, USA). The surface area ( $S_{\text{BET}}$ ) was calculated using a Brunauer-Emmett-Teller (BET) method including micropore ( $S_{\text{micro}}$ ) and mesopore surface area ( $S_{\text{meso}}$ ) at a relative pressure  $P/P_0$  of 0.1 and 0.05-0.3, respectively. The total pore volume ( $V_{\text{total}}$ ) and external surface area ( $S_{\text{ex}}$ ) were estimated using t-plot method.

The morphology of samples was also observed by Field Emission Scanning Electron Microscopy (FE-SEM, AURIGA, Carl Zeiss, Baden-Württemberg, Germany). Elemental compositions of synthesized zeolites were determined by using Scanning Electron Microscope and Energy Dispersive Spectrometer (FE-SEM/EDS, JEOL JSM 7800F, Akishima, Tokyo, Japan).

The thermal degradation of the samples was investigated by thermogravimetric analysis (TGA/DTG, Mettler TGA-DSC1 Schwerzenbach, Switzerland). The analysis was conducted under an air-zero atmosphere with a flow rate of 50.0 mL/min. The samples were heated at a rate of 10.0 °C/min until reaching a temperature of 700 °C.

### 3.3 Result and discussion

**Figure 3.1** presents XRD pattern and FTIR spectra of trunk grass in its original state and after treatment. The treated grass shows the disruption of crystalline cellulose, hemicellulose, and lignin components within the lignocellulose biomass compared to the untreated grass. As a result, the treated grass can more easily access the cellulose (Amin et al., 2017).

**Figure 3.1a** illustrates the distinctive peaks of crystalline cellulose at 15° and 22°, representing the 110 and 200 planes, respectively (Kandhola et al., 2020). These results demonstrate a considerable reduction in the crystallinity of cellulose following the alkaline hydrolysis, which become to amorphous cellulose. Moreover, the FTIR spectra of the alkaline hydrolyzed samples are provided (**Figure 3.1b**). A broad band appears at 3340  $\text{cm}^{-1}$ , indicating an increase in cellulose fraction (Kandhola et al., 2020; Kundu et al., 2021). Following acid treatment, RT showed signals ascribed to the aromatic vibration of lignin at 1511 and 1729  $\text{cm}^{-1}$  (Nandanwar et al., 2016; Khalid et al., 2021). These findings explain the robust structure of trunk grass. Although the

lignin was observed. It was eliminated after alkaline hydrolysis. It is worth noting that the alkaline hydrolysis greatly lowers the complexity of the lignocellulosic fiber.

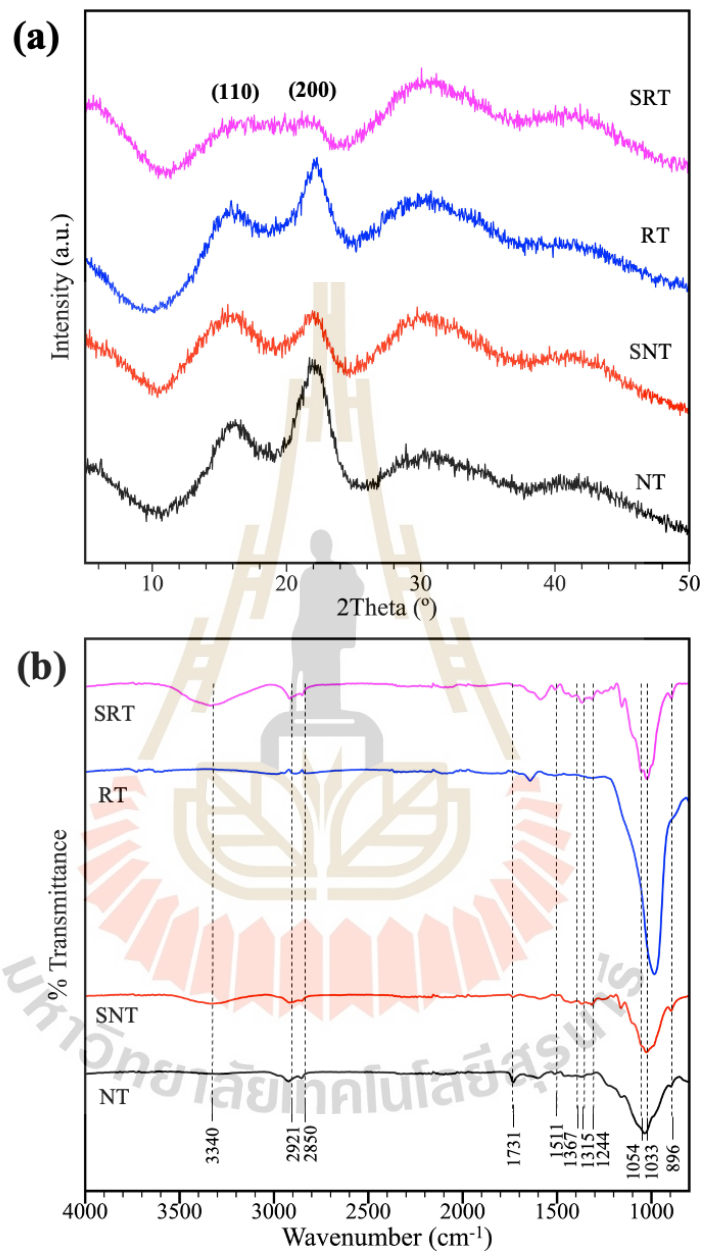


**Figure 3.1** XRD pattern and FTIR spectra of non-refluxed trunk (NT), acid-refluxed trunk (RT), and NaOH soaked samples (SNT and SRT).

Figure 3.2 displays the raw and modified grass after acid treatment and alkaline hydrolysis. The untreated grass (Figure 3.2a) displays a continuous fiber structure and a smooth surface. However, after acid treatment, noticeable disruptions in the fiber structure are observed, leading to a rough surface (Figure 3.2b), which is in line with the finding by Zarib et al. (2020). After alkaline hydrolysis, further distortions in the surface of the trunk become evident (Figure 3.2c-d).

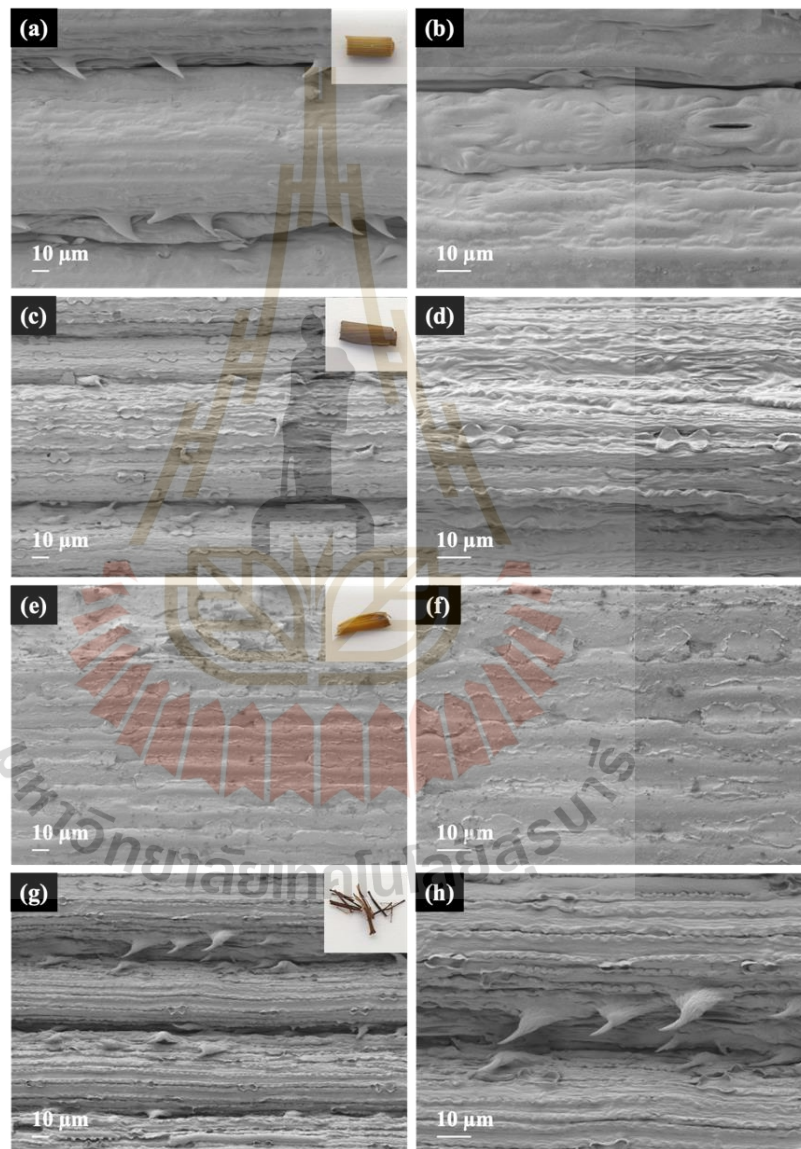


Figure 3.2 SEM images of NT (a,b), RT (c,d), RNT (e,f), and SRT (g,h) in different magnification.

Figure 3.3 depicts the thermogravimetric analysis (TGA) and derivative thermogravimetry (DTG) plots of NT and modified NT by NaOH and HCl treatment. The first stage of weight loss in temperatures up to 250 °C corresponds to the desorption of water (Ribeiro et al., 2019). Additionally, hemicellulose and cellulose started their decomposition easily, with the weight loss happening at 315 to 400 °C (Yang et al., 2007). At above 400 °C, the combustion of the lignin and char occurred. Nevertheless, modified grass revealed that the lignocellulose was pyrolyzed with a very low solid residue (0.85-1.29 wt.%) compared with NG (4.57 wt.%). This finding is consistent with previous XRD and FTIR results.

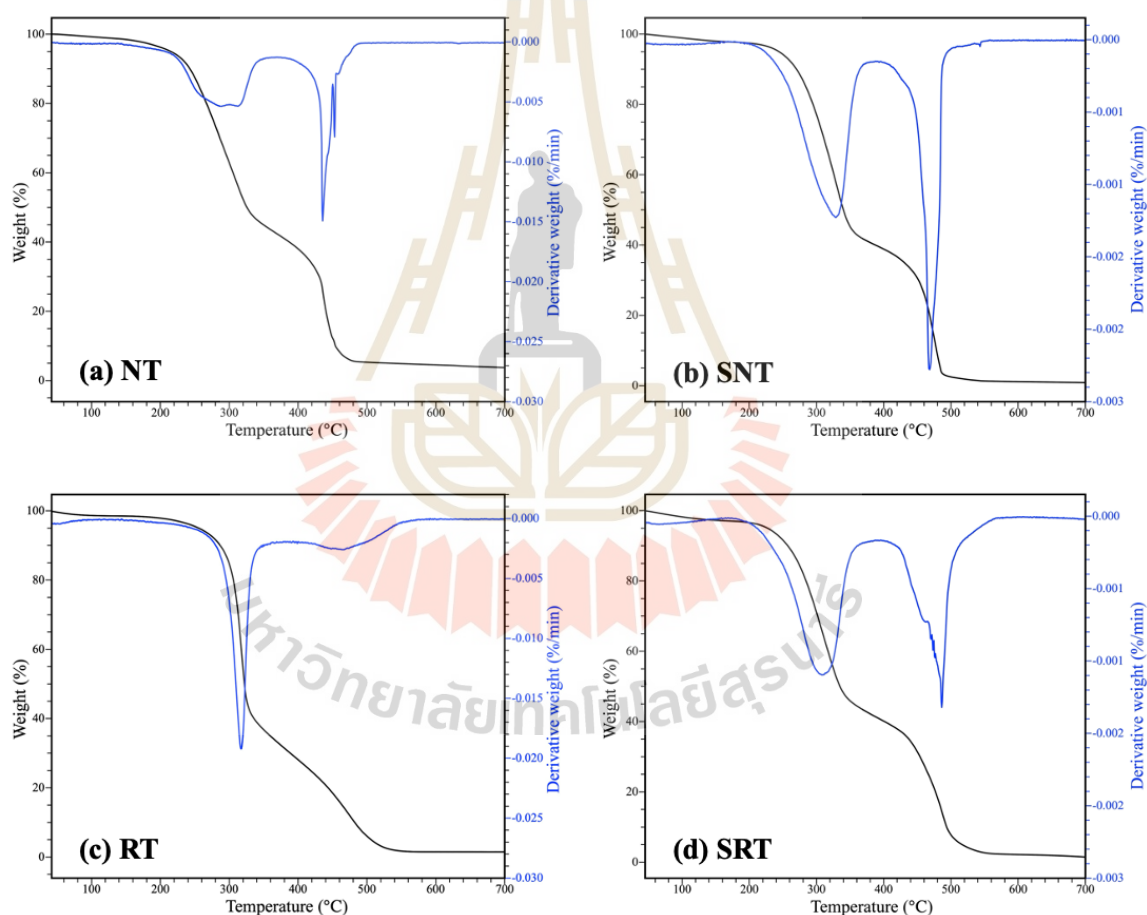
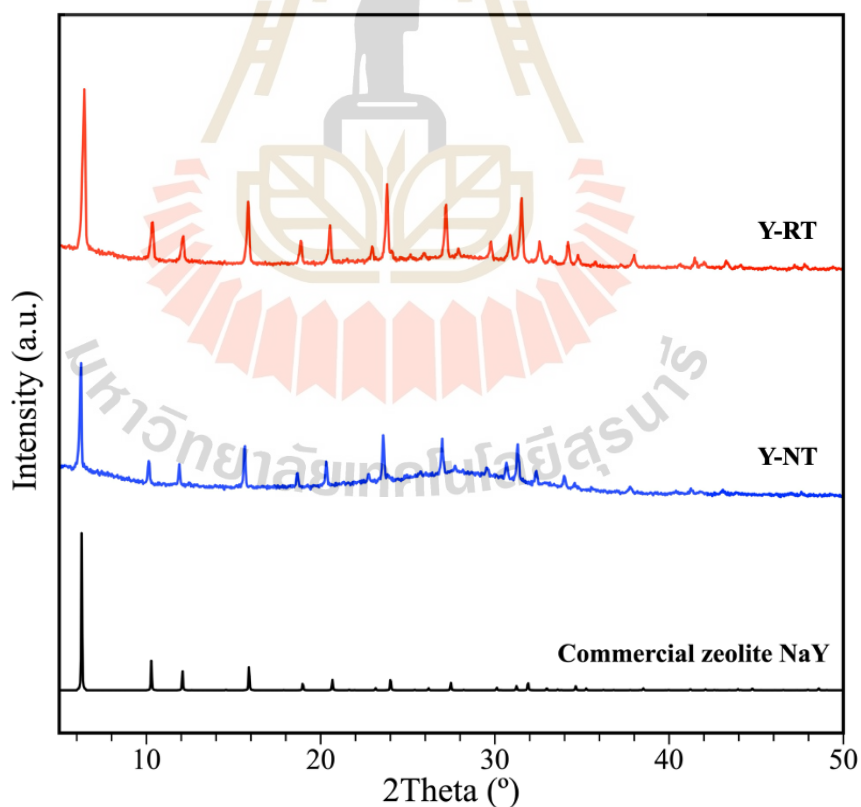


Figure 3.3 TGA (a) and DTG (b) curves of NT and modified NT.

**Figure 3.4** shows the XRD patterns of Y-NT and Y-RT. Both samples expose the characteristic peaks of zeolite NaY. However, a broad peak at  $28^\circ$  attributed to the amorphous aluminosilicate appears, indicating a mixed phase (Popova et al., 2014; Ma et al., 2020). Moreover, Y-NT has lower intensities, indicating a lower degree of crystallinity.

**Figure 3.5-3.8** present SEM images at different magnifications and EDS mapping of Y-NT and Y-RT. The physical morphology of Y-NT is similar to Y-RT, consisting of zeolite particles with an approximate diameter of  $5\ \mu\text{m}$ , sponge-like phase, and residue trunk fiber. In addition, the Si/Al ratios of crystals were 2.13. Their EDS mapping are illustrated in **Figure 3.7-3.8**. These results clearly indicate that the sponge-like phase is amorphous aluminosilicate, corresponding to the XRD results mentioned earlier. Consequently, the trunk grass prevents the growth of zeolite crystals, leading to the persistence of an amorphous phase.



**Figure 3.4** XRD pattern of zeolite NaY using non-refluxed trunk (Y-NT) and acid-refluxed trunk (Y-RT).

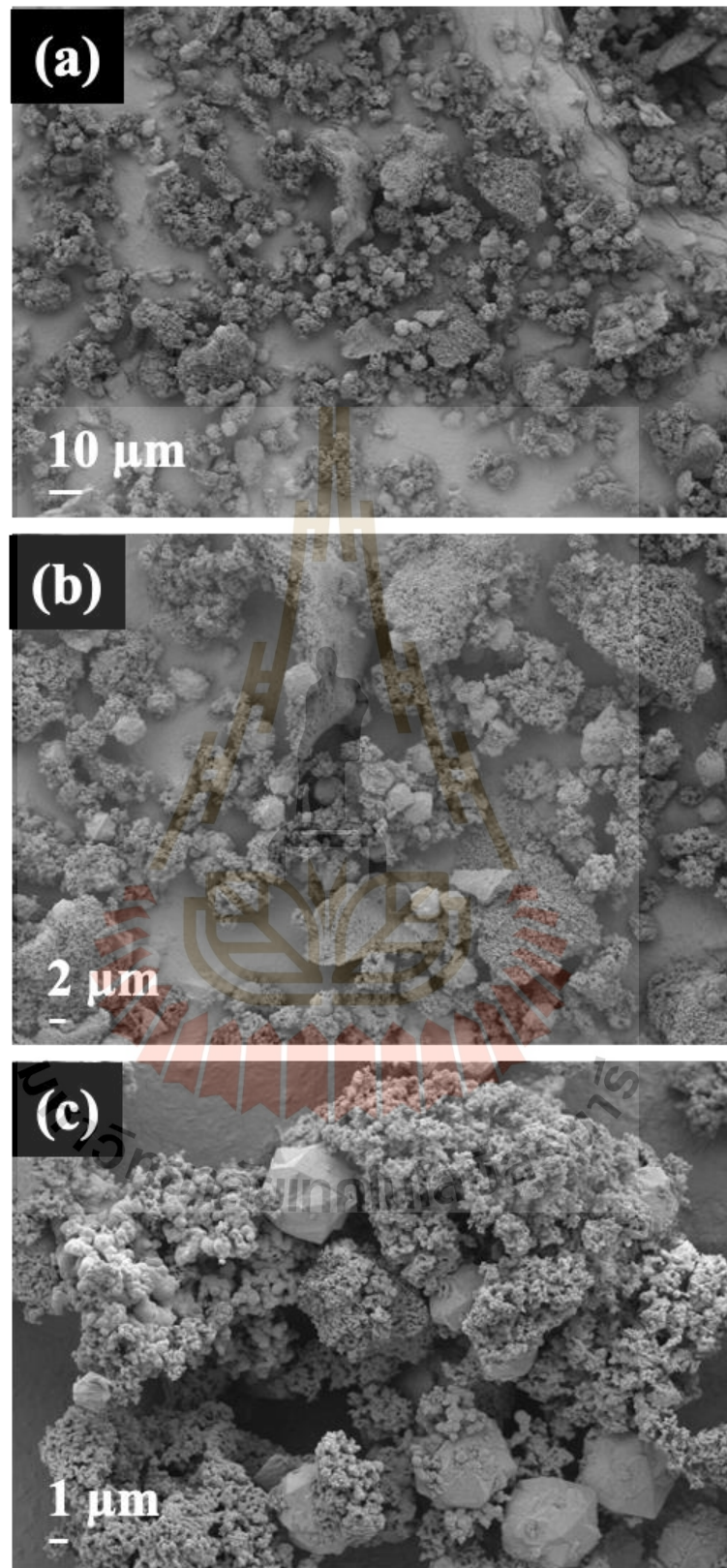


Figure 3.5 SEM images of Y-NT in different magnifications.

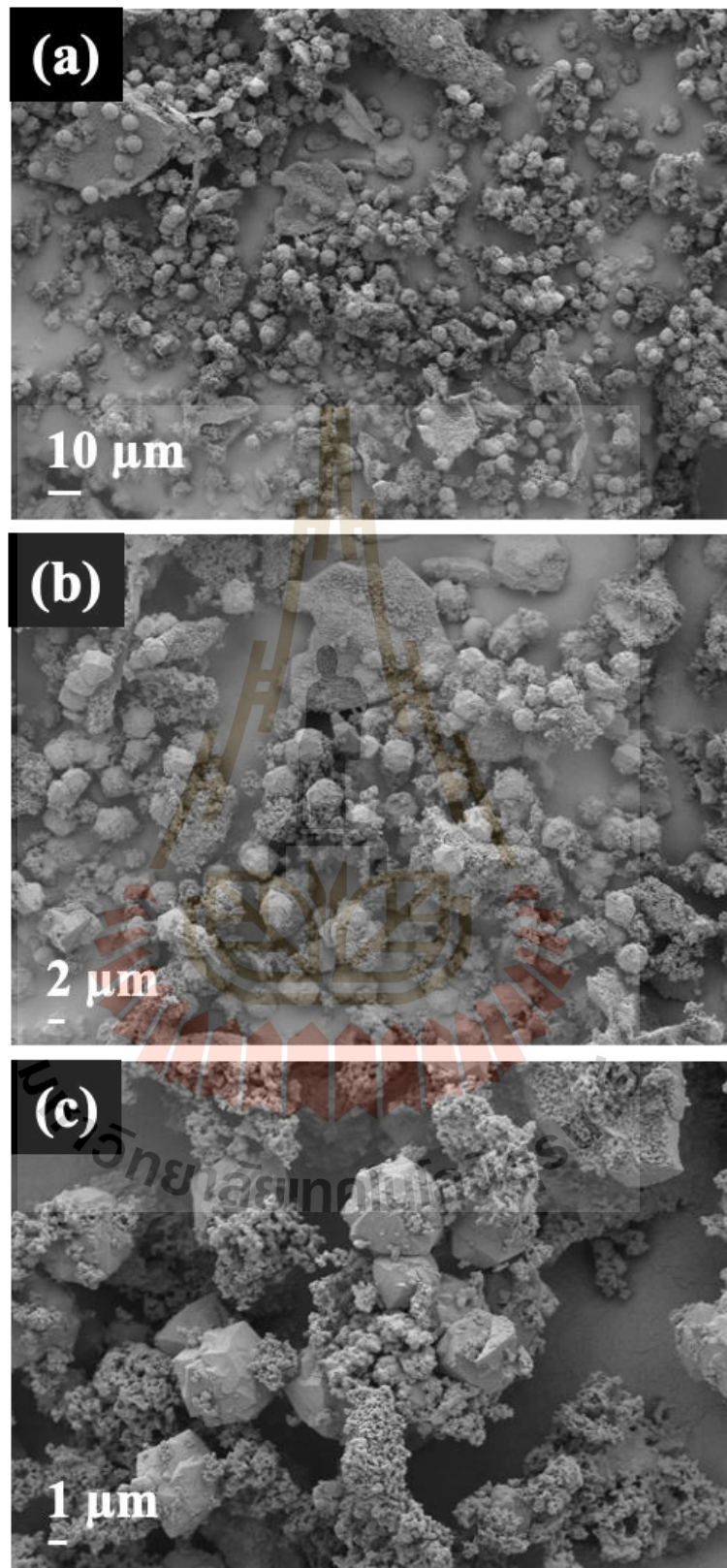


Figure 3.6 SEM images of Y-RT in different magnifications.

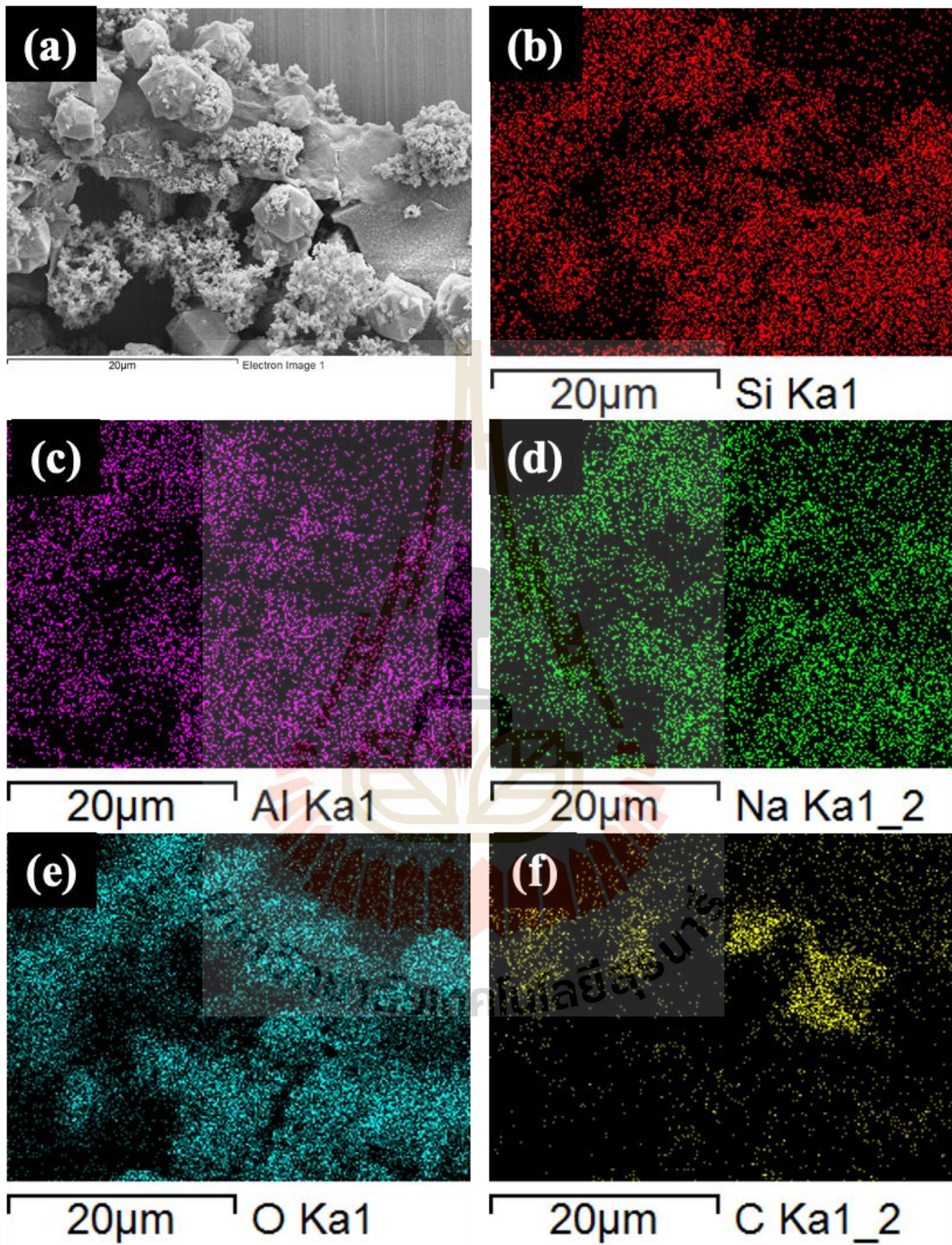


Figure 3.7 SEM images and EDS mapping of Y-NT.

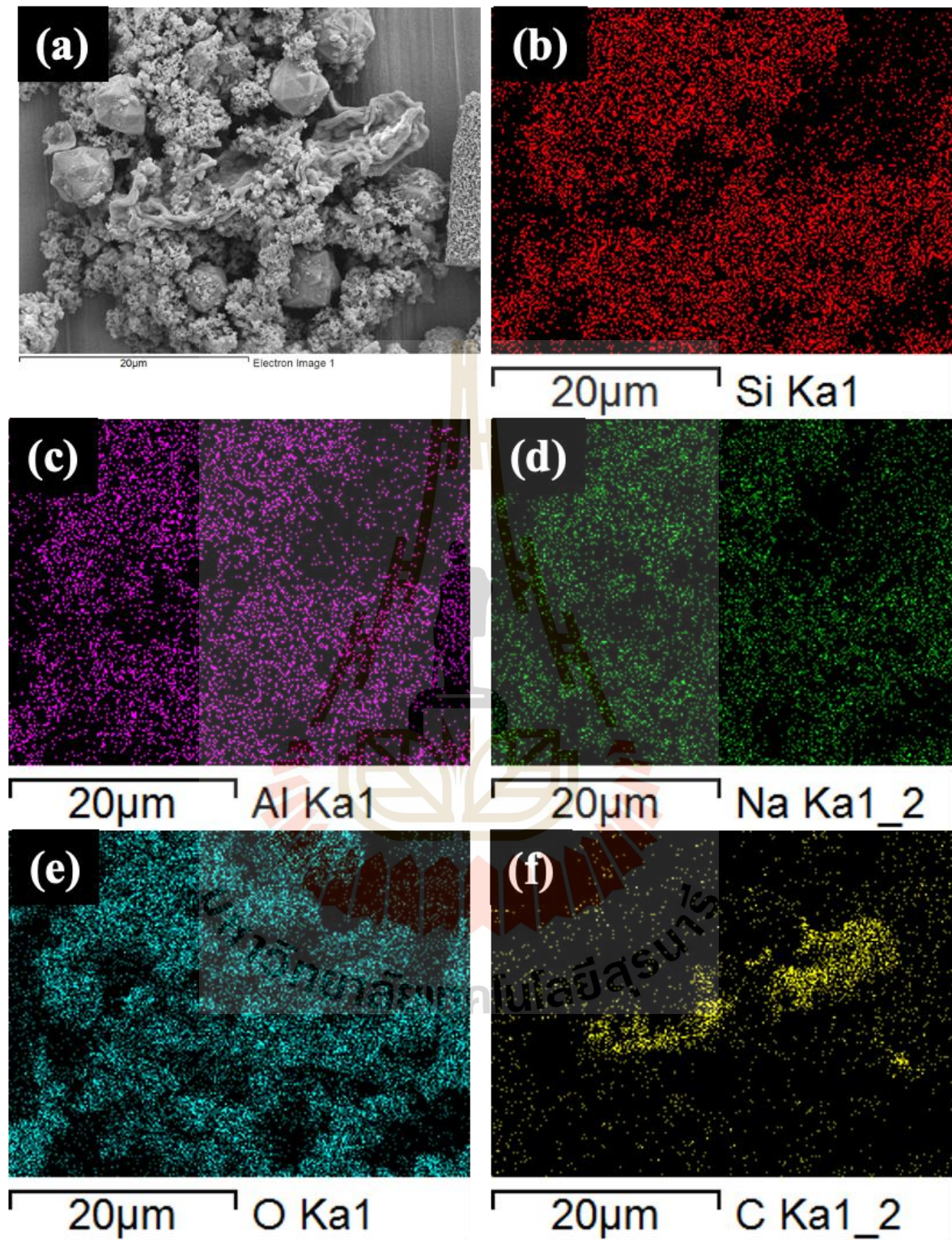
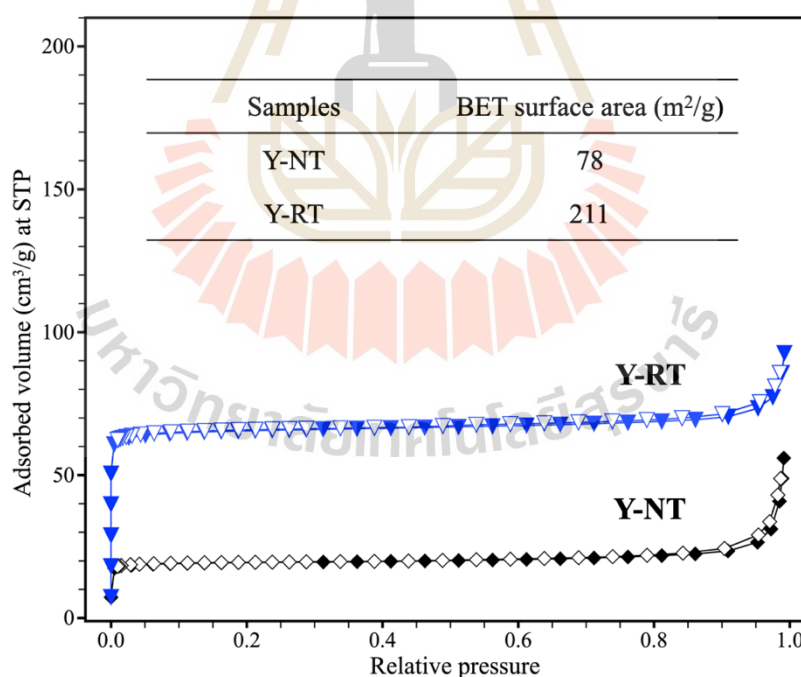


Figure 3.8 SEM images and EDS mapping of Y-RT.

**Figure 3.9** presents the nitrogen adsorption-desorption isotherm to estimate the textural properties for the NaY samples. All samples show a type I isotherm, as classified by IUPAC (Sing, 1985). The adsorbed volume increases quickly at low-pressure to generate a monolayer, which is a typical type for microporous materials. The surface area of Y-NT is estimated as 78 m<sup>2</sup>/g, while Y-RT has 211 m<sup>2</sup>/g. The evidence implies a higher degree of the crystallinity in Y-RT.

However, the presence of amorphous phase is still observed in Y-RT due to the rich potassium content in trunk grass. The incorporation of potassium in zeolite NaY synthesis has been reported by Ajayi et al. (2018). Potassium ion, with a larger size (1.33 Å) compared sodium ion (0.95 Å), are highly active in silica depolymerization, causing poor dissolution of aluminosilicate (Phair and Van Deventer, 2001). High levels of potassium disrupt the system and slow down the zeolite growth rate. Thereby, the addition of trunk grass, which contains potassium content up to 14 wt.% (Bunmai et al., 2018), hinders the formation of zeolite.



**Figure 3.9** Nitrogen adsorption-desorption isotherm of Y-NT and Y-RT; filled symbols = adsorption and hollow symbols = desorption.

### 3.4 Conclusion

The utilization of non-refluxed and acid-refluxed trunk grass (NT and RT) in the synthesis of zeolite NaY resulted in the production of Y-NT and Y-RT samples. Both samples exhibit characteristic of zeolite NaY, but they also display the presence of two distinct phases: crystal and amorphous. This phenomenon suggests an incomplete formation of zeolite, likely due to the presence of potassium. However, both Y-NT and Y-RT samples demonstrate uniform zeolite particles size (5  $\mu\text{m}$ ) and well dispersion. These observations indicate that trunk grass has the potential to facilitate zeolite formation and ensure uniform distribution, mitigating the occurrence of polycrystallinity in the synthesized materials. Further research into optimizing the synthesis process involving trunk grass may yield insights into growing zeolite and its properties for various applications.

### 3.5 References

- Ajayi, O. A., Adefila, S. S., and Ityokumbul, M. T. (2018). Monitoring zeolite NaY formation from potassium-rich Nigerian kaolinite clay. *Ain Shams Eng. J.*, 9(4), 1653-1661.
- Amin, F. R., Khalid, H., Zhang, H., Rahman, S. U., Zhang, R., Liu, G., and Chen, C. (2017). Pretreatment methods of lignocellulosic biomass for anaerobic digestion. *AMB Express*, 7(1), 72.
- Bunmai, K., Osakoo, N., Deekamwong, K., Rongchapo, W., Keawkumay, C., Chanlek, N., Prayoonpokarach, S., and Wittayakun, J. (2018). Extraction of silica from cogon grass and utilization for synthesis of zeolite NaY by conventional and microwave-assisted hydrothermal methods. *J. Taiwan Inst. Chem. Eng.*, 83, 152-158.
- Estrada, J. A., and Flory, S. L. (2015). Cogongrass (*Imperata cylindrica*) invasions in the US: Mechanisms, impacts, and threats to biodiversity. *Glob. Ecol. Conserv.*, 3, 1-10.
- Gomes, E. S., Aranda, D. A. G., Pereira, M. M., and Louis, B. (2018). ZSM-5 synthesis by the assistance of biomass and biomass-derivate compounds. *Microporous Mesoporous Mater.*, 263, 251-256.

- Holzmueller, E. J., and Jose, S. (2010). Invasion success of cogongrass, an alien  $C_4$  perennial grass, in the southeastern United States: exploration of the ecological basis. *Biol. Invasions*, 13(2), 435-442.
- Kandhola, G., Djioleu, A., Rajan, K., Labbé, N., Sakon, J., Carrier, D. J., and Kim, J.-W. (2020). Maximizing production of cellulose nanocrystals and nanofibers from pre-extracted loblolly pine kraft pulp: a response surface approach. *Bioresour. Bioprocess.*, 7(1), 1-16.
- Keawkumay, C., Rongchapo, W., Sosa, N., Suthirakun, S., Koleva, I. Z., Aleksandrov, H. A., Vayssilov, G. N., and Wittayakun, J. (2019). Paraquat adsorption on NaY zeolite at various Si/Al ratios: A combined experimental and computational study. *Mater. Chem. Phys.*, 238, 121824.
- Khalid, F. E., Ahmad, S. A., Zakaria, N. N., Shaharuddin, N. A., Sabri, S., Azmi, A. A., Khalil, K. A., Verasoundarapandian, G., Gomez-Fuentes, C., and Zulkharnain, A. (2021). Application of cogon Grass (*Imperata cylindrica*) as biosorbent in diesel-filter system for oil spill removal. *Agron*, 11(11), 2273.
- Kosawatthanakun, S., Pansakdanon, C., Sosa, N., Chanlek, N., Roessner, F., Prayoonpokarach, S., and Wittayakun, J. (2022). Comparative properties of K/NaX and K/NaY from ultrasound-assisted impregnation and performance in transesterification of palm oil. *ACS Omega*, 7(11), 9130-9141.
- Kulawong, S., Chanlek, N., and Osakoo, N. (2020). Facile synthesis of hierarchical structure of NaY zeolite using silica from cogon grass for acid blue 185 removal from water. *J. Environ. Chem. Eng.*, 8(5), 104114.
- Kundu, C., Samudrala, S. P., Kibria, M. A., and Bhattacharya, S. (2021). One-step peracetic acid pretreatment of hardwood and softwood biomass for platform chemicals production. *Sci Rep.*, 11(1), 11183.
- Lewis, D., Freeman, C., and Catlow, C. (1995). Predicting the templating ability of organic additives for the synthesis of microporous materials. *J. Phys. Chem.*, 99(28), 11194-11202.
- Louis, B., Gomes, E. S., Coelho, T., Lutzweiler, G., Losch, P., Silva, A. V., Faro, A. C., Romero, T., Osman, M. B., Balanqueux, A., Bernardon, C., and Pereira, M. M. (2016).

- Influence of biomass residues on the metastability of zeolite structures. *Nanosci. Nanotechnol. Lett.*, *8*(11), 917-923.
- Louis, B., Gomes, E. S., Losch, P., Lutzweiler, G., Coelho, T., Faro, A., Pinto, J. F., Cardoso, C. S., Silva, A. V., and Pereira, M. M. (2017). Biomass-assisted zeolite syntheses as a tool for designing new acid catalysts. *ChemCatChem*, *9*(12), 2065-2079.
- Ma, H., Jiao, K., Xu, X., and Song, J. (2020). Synthesis and characterization of a new aluminosilicate molecular sieve from aluminosilica perhydrate hydrogel. *Materials*, *13*(23), 5469.
- Mintova, S., and Valtchev, V. (1996). Deposition of zeolite A on vegetal fibers. *Zeolites*, *16*(1), 31-34.
- Nandanwar, R., Chaudhari, A., and Ekhe, J. (2016). Nitrobenzene oxidation for isolation of value added products from industrial waste lignin. *J. Chem. Biol. Phys. Sci.*, *6*, 501-513.
- Ocampo, F., Cunha, J. A., de Lima Santos, M. R., Tessonier, J. P., Pereira, M. M., and Louis, B. (2010). Synthesis of zeolite crystals with unusual morphology: Application in acid catalysis. *Appl. Catal. A-Gen.*, *390*(1-2), 102-109.
- Pereira, M. M., Gomes, E. S., Silva, A. V., Pinar, A. B., Willinger, M. G., Shanmugam, S., Chizallet, C., Laugel, G., Losch, P., and Louis, B. (2018). Biomass-mediated ZSM-5 zeolite synthesis: when self-assembly allows to cross the Si/Al lower limit. *Chem. Sci.*, *9*(31), 6532-6539.
- Phair, J., and Van Deventer, J. (2001). Effect of silicate activator pH on the leaching and material characteristics of waste-based inorganic polymers. *Miner. Eng.*, *14*(3), 289-304.
- Popova, M., Ristić, A., Mavrodinova, V., Maučec, D., Mindizova, L., and Novak Tušar, N. (2014). Design of cobalt functionalized silica with interparticle mesoporosity as a promising catalyst for VOCs decomposition. *Catal. Letters*, *144*(6), 1096-1100.
- Rakmae, S., Keawkumay, C., Osakoo, N., Montalbo, K. D., de Leon, R. L., Kidkhunthod, P., Chanlek, N., Roessner, F., Prayoonpokarach, S., and Wittayakun, J. (2016). Realization of active species in potassium catalysts on zeolite NaY prepared by ultrasound-assisted impregnation with acetate buffer and improved performance in transesterification of palm oil. *Fuel*, *184*, 512-517.

- Ribeiro, S. P. d. S., Martins, R. C., Barbosa, G. M., Rocha, M. A. d. F., Landesmann, A., Nascimento, M. A. C., and Nascimento, R. S. V. (2019). Influence of the zeolite acidity on its synergistic action with a flame-retarding polymeric intumescent formulation. *J. Mater. Sci.*, 55(2), 619-630.
- Rongchapo, W., Sোধiphun, O., Rintramee, K., Prayoonpokarach, S., and Wittayakun, J. (2013). Paraquat adsorption on porous materials synthesized from rice husk silica. *Water Sci. Technol.*, 68(4), 863-869.
- Sing, K. S. (1985). Reporting physisorption data for gas/solid systems with special reference to the determination of surface area and porosity (Recommendations 1984). *Pure Appl. Chem.*, 57(4), 603-619.
- Surtiningsih, T., Agustina, D., and Manuhara, Y. S. W. (2018). Hydrolysis of imperata cylindrica (L.) Beauv. By penicillium sp., aspergillus Niger and trichoderma viride as bioethanol basic ingredient production. *Biosci. Res.*, 15(3), 2318-2326.
- Valtchev, V., Mintova, S., Vulchev, I., and Lazarova, V. (1994). Influence of reactive radicals in cellulose fibres on the formation of zeolite coatings. *J. Chem. Soc., ChemComm.*, (18), 2087-2088.
- Yang, H., Yan, R., Chen, H., Lee, D. H., and Zheng, C. (2007). Characteristics of hemicellulose, cellulose and lignin pyrolysis. *Fuel*, 86(12-13), 1781-1788.
- Zarib, N., Abdullah, S., and Jusri, N. (2020). Effect of acid treatment on extraction of silica from cogon grass by using  $C_6H_8O_7$  and HCL Acid. *IOP Conf. Ser. Mater. Sci. Eng.*, 834, 012067.

# CHAPTER IV

## THE SYNTHESIS OF WELL-DISPERSED AND UNIFORM-SIZED ZEOLITE NaY BY ADDING NON-REFLUXED AND ACID-REFLUXED BLADE

### 4.1 Introduction

Zeolite NaY belongs to the faujasite framework (FAU), characterized by a typical silicon-to-aluminum ratio (Si/Al) in the range of 2–5, with sodium serving as the charge-balancing ion (Baerlocher, 2008). NaY has three-dimensional channels with a pore diameter of 7.4 Å. Its outstanding properties, including a large surface area and high sodium content, have made it versatile for various applications, such as an adsorbent of paraquat and dye (Rongchapo et al., 2013; Keawkumay et al., 2019; Kulawong et al., 2020). Despite its utility, challenges persist in the synthesis of zeolite NaY to achieve precise control over its properties for specific applications such as crystal size, structure, and chemical composition. The properties of NaY are influenced by various synthesis parameters (Li et al., 2023; Li et al., 2023).

Efforts have been directed towards optimizing the characteristics of zeolites through several synthesis methods. One approach involves the use of additives in one-pot synthesis, allowing for tailoring the properties of zeolites (Zhao et al., 2016; Zhu et al., 2020). Additives play a crucial role in promoting the aggregation of precursor molecules and facilitating zeolite particle nucleation (Lewis et al., 1995). For example, researchers have explored the utilization of biomass as an additive in zeolite synthesis. Sugarcane bagasse residue has been investigated to introduce a new morphology in MFI zeolite (Ocampo et al., 2010; Louis et al., 2016; Louis et al., 2017). Biomass-derived additives can influence the direction of crystal growth and zeolite formation. The hydrolysis of bagasse under base conditions yields molecules containing both hydrophilic sites (hydroxyl groups) and hydrophobic sites (organic species). The hydroxyl groups have demonstrated

potential as binding sites for zeolite precursors (Valtchev et al., 1994; Mintova and Valtchev, 1996).

In related studies, glucose was utilized in the synthesis of various hierarchical ZSM-5 materials (Nandan et al., 2014). The preference for the interaction between hydrocarbon molecules and aluminates over silicates results in a higher aluminum content in the final product (Gomes et al., 2018; Pereira et al., 2018). These findings underscore the impact of additives on the chemical composition and properties of zeolites, emphasizing the potential of biomass-derived additives in zeolite synthesis.

An interesting biomass explored in this work is cogon grass (*Imperata Cylindrica*) due to its widespread abundance with low economic value. Cogon grass is an invasive species commonly considered undesirable due to its aggressive growth, high flammability, and ability to outcompete native plant species. Its rapid spread leads to the formation of dense stands and negatively impacts biodiversity (Yandoc et al., 2004; Estrada and Flory, 2015). The grass presents a fire hazard and can diminish agricultural productivity by invading fields and interfering with crop growth. Additionally, it offers little nutritional value for livestock and can disrupt grazing areas (Dozier et al., 1998). Efforts to control cogon grass face challenges due to its resilience and quick recolonization. Owing to its abundance, researchers have been exploring ways to enhance its value. With a silica content of approximately 9% in the dry weight of blade grass, cogon grass was used as a silica source to synthesize zeolite NaY and NaX (Bunmai et al., 2018; Kulawong et al., 2020). The organic content in cogon grass could potentially act as a stabilizing agent in zeolite synthesis.

The compositions of cogon grass by weight consist of cellulose (35.1%), hemicellulose (27.6%), lignin (16.5%), and extractives (11.2%) (Kefli et al., 2017). Upon mixing sodium hydroxide with cogon grass, it interacts with the ester bonds in the cellulose and other organic compounds within the cogon grass, leading to their conversion into smaller carbohydrate molecules, alcohol, and sodium salt. These products could influence zeolite formation and crystallization. Regarding bio-silica from cogon grass, acid leaching decomposes organic components and removes inorganic components, thereby yielding higher-purity silica (Kow et al., 2014; Bunmai et al., 2018).

Therefore, the objective of this work is to utilize cogon grass for the synthesis of zeolite NaY. Non-refluxed blade and acid-refluxed blade grass are compared to elucidate the role of organic contents produced in situ within the synthesis gel. Characterization techniques, including X-ray diffraction (XRD), Fourier transform infrared spectroscopy (FTIR), and scanning electron microscopy with energy dispersive spectroscopy (SEM-EDS) are employed to distinguish the properties of the obtained zeolites. Moreover, the adsorption of the herbicide paraquat serves as the primary indicator to differentiate between the zeolite samples. Previous research has reported that zeolite with different properties exhibit different capacities for paraquat adsorption. It has been observed that adsorption on zeolite NaY and NaBEA obeys the Langmuir model, with NaY demonstrating superior adsorption capacities (Rongchapo et al., 2013). Further studies have revealed that NaY has a higher adsorption capacity than NaX due to a higher Si/Al ratio (Rongchapo et al., 2017), and the adsorption on NaY increased with the Si/Al ratio (Keawkumay et al., 2019).

## 4.2 Experiment

### 4.2.1 Material and chemicals

Cogon grass was collected from the Suranaree University of Technology (Nakhon Ratchasima, Thailand). Chemicals used include hydrochloric acid (37%, Merck, *Rahway, USA*), silicon dioxide RPE (99%, Sigma-Aldrich, *St. Louis, USA*), sodium aluminate (95%, Sigma-Aldrich, *St. Louis, USA*), and sodium hydroxide (97%, Carlo Erba, *Emmendingen, Germany*). Commercial-grade paraquat (N,N'-dimethyl-4,4'-bipyridinium dichloride, 27.6%, Shandong Kexin Biochemical, Jinan, *China*) was employed in the adsorption experiments. A 28.7 g of fumed silica was dissolved in 59.8 mL of 0.27 M NaOH solution for preparation of sodium silicate solution (Na<sub>2</sub>SiO<sub>3</sub>).

### 4.2.2 Preparation of cogon grass

Cogon grass was rinsed with water and dried in a hot air oven at 90 °C for 3 days. The blades were separated and cut into 0.5 cm in length. This non-refluxed blade was named NB. The 5.0 g of dried NB was refluxed by using 67.0 mL of 3.0 M HCl solution at 90 °C for 6 h. The solid portion was filtered, washed with deionized (DI) water until pH neutral, and dried at 90 °C for 24 h. The refluxed blade is named RB.

### 4.2.3 Synthesis of zeolite NaY by adding cogon grass

Zeolite NaY was synthesized using a method modified from that of the Synthesis Commission of the International Zeolite Association (Mintova, 2016). The molar composition of the overall gel used was  $1\text{Al}_2\text{O}_3:10\text{SiO}_2:5.1\text{Na}_2\text{O}:180\text{H}_2\text{O}$ . Typically, 1.0 g of dried NB or RB was hydrolyzed with 10.0 mL of 2.5 M NaOH at ambient temperature for 24 h. These samples were named SNB and SRB. Then 4.8 g of  $\text{Na}_2\text{SiO}_3$  solution and 0.4 g of  $\text{NaAlO}_2$  were added to mixture under continuous stirring. The final mixture, a seed gel, was aged at room temperature for 24 h.

A feed gel was prepared in the same way a seed gel, but without aging process. In brief, 2.8 g of  $\text{NaAlO}_2$  and 30.18 g of  $\text{Na}_2\text{SiO}_3$  solution were added to NaOH solution with 0.035 g of NaOH in 22.3 mL of DI water. After that, a feed gel was slowly dropped to the seed gel while stirring and constantly stirred for 10 min. The resultant gel was aged at ambient temperature and crystallized at 90 °C for 24 h. The obtained mixture was washed with DI water until the measured pH was neutral by centrifugation and dried at 90 °C for 24 h. The zeolite samples from non-refluxed and refluxed blade were designated as Y-NB and Y-RB, respectively. The same method was used to produce parent NaY zeolite without any grass. The sample was labeled as Y-WG. The sample Y-NB was also referred to Y-1.0NB to compare the grass amounts (Section 4.2.6). All samples were not calcined.

### 4.2.4 Adsorption of paraquat

The paraquat adsorption was performed following the procedure in the literature (Keawkumay et al., 2019), employing paraquat concentrations ranging from 100 to 1000 mg/L. The adsorption from each concentration was replicated three times. In each experiment, 0.05 g of dried NaY sample was introduced into 20 mL of the targeted paraquat solution with magnetic stirring at 450 rpm for 60 min at 30 °C using a temperature-controlled water bath. The adsorbent was filtered through a 0.45  $\mu\text{m}$  syringe filter and the remaining paraquat solution was analyzed by a UV-Vis spectrophotometer (Varian CARY 300, Palo Alto, USA) at  $\lambda_{\text{max}}$  of 257 nm. The calibration curve of paraquat solution was shown in Figure A1. The paraquat adsorption data were evaluated with Langmuir and Freundlich isotherm models.

The maximum adsorption capacity of paraquat ( $q_m$ ) on adsorbents was determined based on the Langmuir isotherm using Equation (4.1).

$$\frac{C_e}{q_e} = \frac{1}{K_L q_m} + \frac{C_e}{q_m} \quad (4.1)$$

where  $C_e$  and  $q_e$  are the concentration and amount adsorbed at equilibrium, and  $K_L$  is the Langmuir constant related to the affinity of the binding site (L/mg). Both  $K_L$  and  $q_m$  can be determined from the linear plot of  $C_e/q_e$  versus  $C_e$ .

The Freundlich adsorption equation is defined based on Equation (4.2).

$$\log q_e = \log K_F + \frac{1}{n} \log C \quad (4.2)$$

where  $K_F$  is the Freundlich constant, which indicates the relative adsorption capacity of adsorption (mg/g) to proceed in multilayer sorption, while  $\frac{1}{n}$  represents adsorption intensity.

#### 4.2.5 Characterization of materials

Samples phases were validated by X-ray diffraction (XRD, Bruker D8 ADVANCE, Billerica, USA) with Cu K $\alpha$  radiation operated at 40 kV and 40 mA. The XRD data was used to calculate relative crystallinity. The total area of nine prominent peaks of FAU zeolite was estimated by OriginLab, Origin 2022 (9.9). Y-NB was used as a reference since it has the highest total area. The functional groups of the samples were investigated by Fourier-transform infrared spectroscopy (FT-IR, Bruker Tensor 27, Billerica, USA) using attenuated total reflectance (ATR) mode. The morphology, particle size, and Si/Al ratio of the zeolite products were determined by field-emission scanning electron microscopy with energy-dispersive X-ray spectroscopy (FE-SEM/EDX, JEOL JSM 7800F, Akishima, Tokyo, Japan). To improve the sample conductivity, it was dispersed on carbon tape and subjected to a one-minute gold coating. Surface areas and micropore volume were examined using the Brunauer–Emmett–Teller (BET) method and  $t$ -plot method via N<sub>2</sub> adsorption/desorption (BelSorp mini II, Microtrac, Pennsylvania, USA). Thermal decomposition of the products was investigated by the thermogravimetric analysis (TGA, Mettler Toledo TGA/DSC1, Schwerzenbach, Switzerland) in the air-zero with a flow rate of 50.0 mL/min at a heating rate of 10.0 °C/min up to 700 °C.

#### 4.2.6 Synthesis and characterization of zeolite NaY with various amounts of non-refluxed cogon grass

Zeolite NaY was synthesized with the procedure described in **Section 4.2.3**, but with 0.5, 1.5, and 2.0 g of non-refluxed blade. The obtained products were named Y-0.5NB, Y-1.5NB, and Y-2.0NB, respectively. They were characterized by XRD, SEM, and TGA and compared with Y-1.0NB from **Section 4.2.3**.

#### 4.2.7 Effect of calcination on adsorption capacity

The Y-NB synthesis was repeated twice with 1.0 g of non-refluxed blade from the same location. One gram of each zeolite product was calcined at 500 °C for 3 h with a heating rate of 1 °C/min. Before testing for paraquat adsorption, all non-calcined and calcined samples were characterized by XRD (Bruker D2 PHASER) and tungsten scanning electron microscopy (W-SEM, JEOL, JSM-6010LV, Tokyo, Japan).

### 4.3 Results and discussion

#### 4.3.1 Paraquat adsorption on the zeolite samples

**Figure 4.1** illustrated the relationship between the amount of paraquat adsorbed and the initial concentration of NaY synthesized using refluxed blade (Y-RB), non-refluxed blade (Y-NB), and conventional synthesis method without grass (Y-WG) under standard conditions. **Table 4.1** provides the parameters and correlation coefficients ( $R^2$ ) obtained from fitting paraquat adsorption on the zeolite samples with the Langmuir, which could find the numerical data in **Table A1**, and Freundlich models (see details in **Figure A2**). All adsorbents exhibit the adsorption behavior resembling the Langmuir isotherm, which implies the adsorption sites show a monolayer and uniformity. Y-WG demonstrates the best fit, with an  $R^2$  higher than Y-NB and Y-RB. An excellent fit was also reported on zeolite NaY and NaBEA (Rongchapo et al., 2013; Rongchapo et al., 2017). At 1000 mg/L, the adsorption on Y-WG remained essentially constant, whereas that on Y-NB and Y-RB increased. This is likely attributed to multilayer adsorption. Consequently, Y-NB has a higher adsorption capacity than Y-WG as illustrated in **Table 4.1**, and further details are provided in **Table A2**. From the fit with the Freundlich models, Y-NB and Y-RB had greater  $R^2$  values compared to Y-WG. It

appears probable that other adsorption sites, apart from those associated with the zeolite phase, were responsible for multilayer adsorption. Thus, Y-NB and Y-RB were analyzed by several techniques in comparison with Y-WG to understand their adsorption behaviors.

Even though Y-NB had the highest adsorption capacity, the conclusion from a single point was not definitive. Consequently, the synthesis was repeated twice, as described in **Section 4.2.7 of Section 4.2**, detailing the synthesis of zeolite NaY through the addition of blade grass. The adsorption performance and zeolite characteristics results are provided in **Section 4.2.4 and 4.2.7**, respectively.

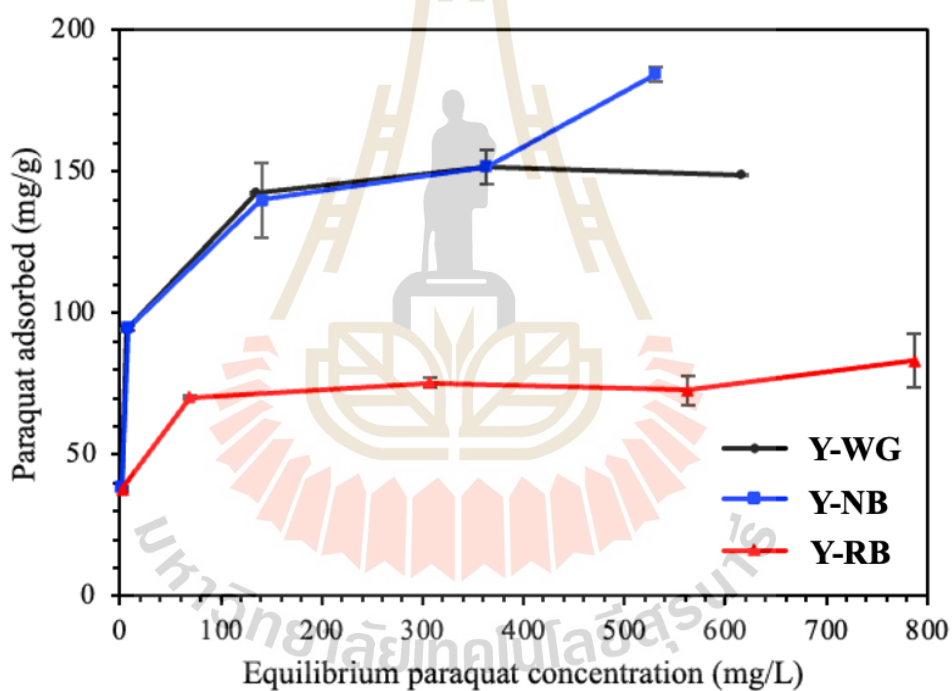


Figure 4.1 Adsorption of paraquat on Y-WG, Y-NB, and Y-RB.

**Table 4.1** The parameters of paraquat adsorption fit with the Langmuir and Freundlich models.

Sample	Langmuir Model			Freundlich Model		
	$q_m$ (mg/g)	$K_L$ (L/mg)	$R^2$	$K_F$ (mg/g)	$n$	$R^2$
Y-WG	$150.8 \pm 1.3$	0.3350	0.9997	46.5	4.890	0.8648
Y-NB	$178.0 \pm 1.8$	0.0522	0.9915	44.5	4.410	0.9071
Y-RB	$80.0 \pm 8.0$	0.1434	0.9814	5.02	15.39	0.9274

#### 4.3.2 Characterization of the zeolite samples

**Figure 4.2** exhibits the XRD patterns of Y-RB, Y-NB, and Y-WG. All samples show the characteristic peaks of FAU zeolite (Baerlocher, 2008, Montova, 2016). The dominant zeolite peaks are observed, providing essentially flat baselines that differ from those of non-refluxed and refluxed grass as depicted in **Figure 4.3a** (Amin et al., 2017). The relative crystallinity of each sample was assessed by comparing the total peak areas of the nine most significant peaks relative to the sample with the highest total area. Y-NB showed slightly higher crystallinity than Y-WG and significantly higher than Y-RB. These findings imply that the addition of non-refluxed cogon grass could enhance the crystallinity of NaY, while the addition of refluxed grass has the opposite effect. Upon adding cogon grass to the zeolite synthesis, lignin undergoes degradation under alkaline conditions, forming small organic molecules (Haque et al., 2016; Surtiningsih et al., 2018). The FTIR spectra of non-refluxed grass reveal a prominent peak corresponding to the hydroxyl groups of carbohydrate molecules refer to **Figure 4.3b** and **Table 4.2** (Xu et al., 2007; Kandhola et al., 2020). Those groups could influence the zeolite synthesis process.

Y-RB demonstrates the lowest crystallinity, suggesting that the acid-refluxed blade (RB) had a detrimental impact on the crystallization process. The reflux process leads to the degradation of the grass as illustrated in **Figure 4.3**. According to **Figure 4.3b**, the FTIR spectra confirmed the disappearance of the  $\beta$ -glycosidic linkage (Xu et al.,

2007; Kandhola et al., 2020; Zarib et al., 2020). Cogon grass contains partially complex carbohydrates, such as cellulose and hemicellulose, which undergo hydrolysis to form glucose and fructose under reflux conditions. These compounds were subsequently removed by washing with DI water. As a result, the remaining fibers possess fewer functional groups, impacting zeolite synthesis.

Regarding paraquat adsorption, the adsorption behaviors of Y-WG and Y-NB were similar at initial concentrations of 100 to 750 mg/L. The similarity might be due to similar crystallinity since paraquat adsorption occurs in the zeolite cavities (Rongchapo et al., 2013; Rongchapo et al., 2017).

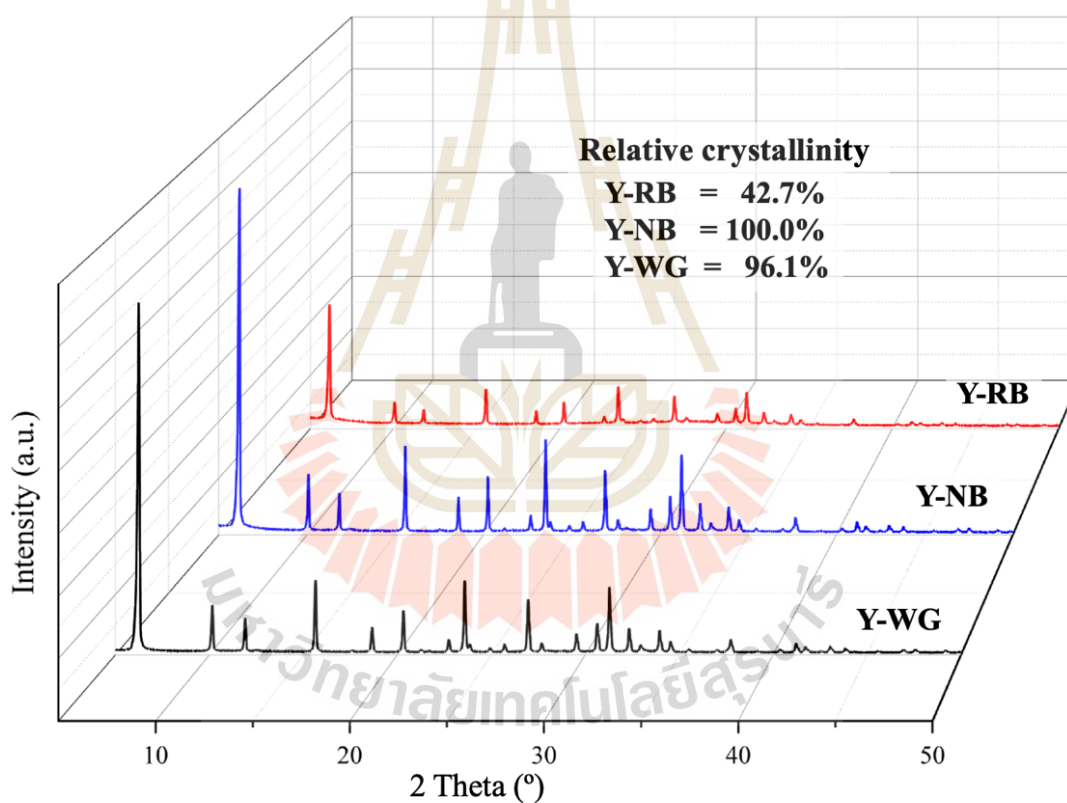


**Figure 4.2** XRD pattern of NaY with acid-refluxed blade (Y-RB) and non-refluxed grass (Y-NB) compared with the zeolite NaY without grass (Y-WG).

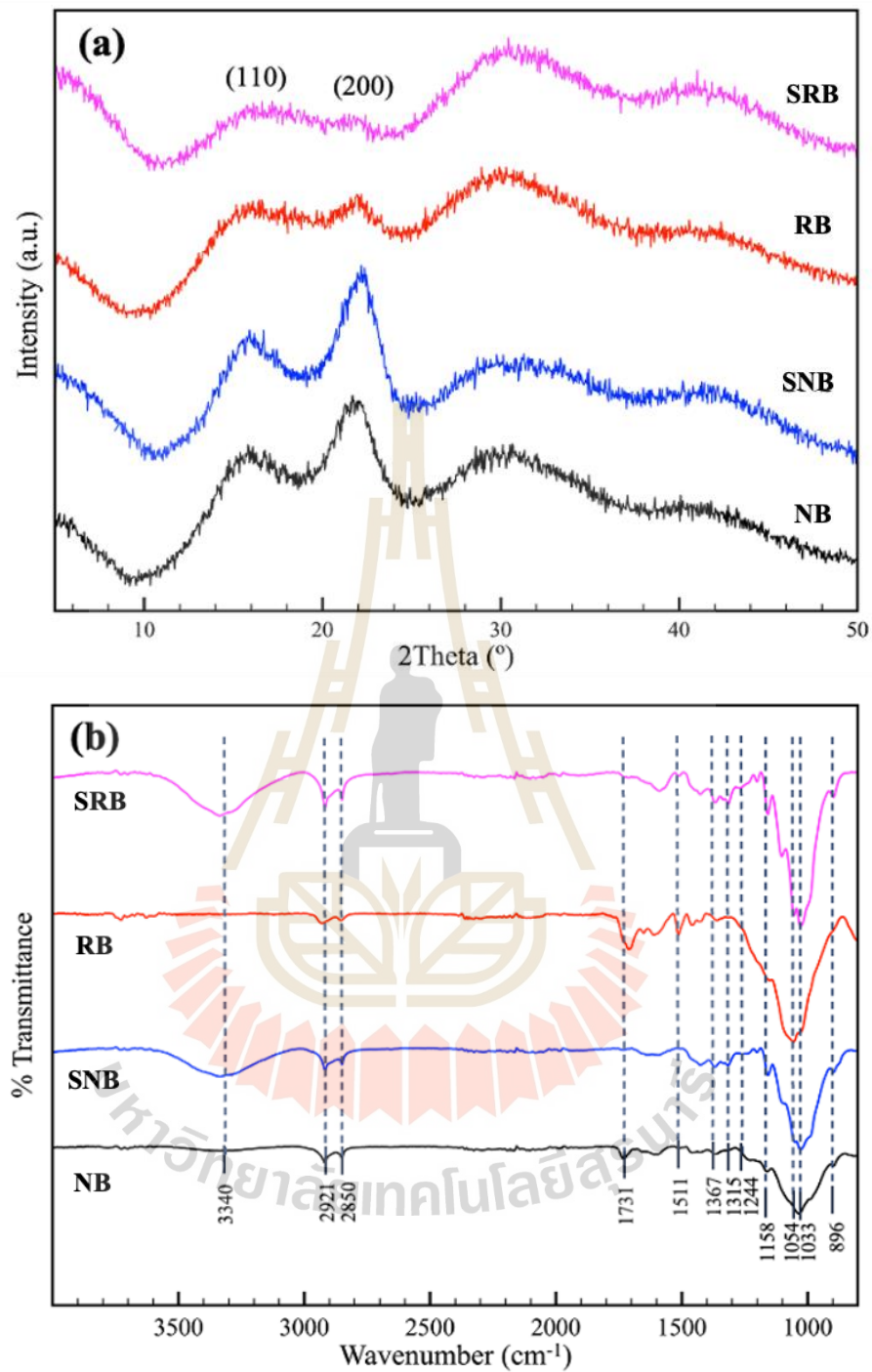


Figure 4.3 XRD pattern (a) and FTIR spectra (b) of non-refluxed (NB), acid-refluxed (RB), and NaOH-soaked blade samples (SNB and SRB).

**Table 4.2** Peak assignments of functional groups of samples.

Wavenumber (cm <sup>-1</sup> )	Assignment	Reference
3340	O-H group stretching of cellulose	Kandhola et al. (2020); Kundu et al. (2021)
2921	C-H stretching in lignocellulose	
2850	Methyl and methylene groups of lignin	Nandanwar et al. (2016);
1731	C=O acetyl group or carbonyl group of hemicellulose and lignin unit	Khalid et al. (2021)
1511	Aromatic stretching of lignin	
1367, 1315, 1244	C-O and C-H bending of hemicellulose	Xu et al. (2007); Yuan et al. (2017)
1158	C-O-C glycosidic bond of cellulose and hemicellulose	
1054	C-O in C-O-C ring skeletal vibration of cellulose and lignin	Lopes et al. (2018); Kundu et al. (2021)
1033	C-O-H stretching of alcohol of cellulose and lignin	
896	$\beta$ -glycosidic linkage between glucose units of cellulose	Haque et al. (2016)

Figure 4.4 shows the FTIR spectra of Y-WG, Y-NB, and Y-RB. The spectra of all samples exhibit peaks at similar positions. The peaks originating from internal tetrahedra were assigned as follows (Karge, 2001):  $1130\text{ cm}^{-1}$ , asymmetrical stretch ( $\nu_{\text{asym}}$ ) of Si-O-Si;  $695\text{ cm}^{-1}$ , symmetrical stretch ( $\nu_{\text{sym}}$ ) of O-T-O; and  $454\text{ cm}^{-1}$ , T-O bend. The peaks from the external linkages were assigned as follows:  $571\text{ cm}^{-1}$  double-ring vibration; and  $1130\text{ cm}^{-1}$  and  $772\text{ cm}^{-1}$ , asymmetrical and symmetrical stretches of O-T-O, respectively. It is worth noting that some peaks in the Y-RB spectrum exhibit lower intensity than others, such as the peak at  $571\text{ cm}^{-1}$  compared to the peak at  $695\text{ cm}^{-1}$ . This observation aligns with the XRD results, indicating that Y-RB possesses the lowest crystallinity (Karge, 2001).

The peaks originating from hydroxyl groups were identified as follows (Karge, 2001): the asymmetrical stretch at  $3500\text{ cm}^{-1}$  and the deformation band of adsorbed water at  $1640\text{ cm}^{-1}$ . Among the samples, Y-WG exhibited a stronger intensity in the first band than Y-NB and Y-RB, indicating that Y-WG possessed a higher degree of hydrophilicity.

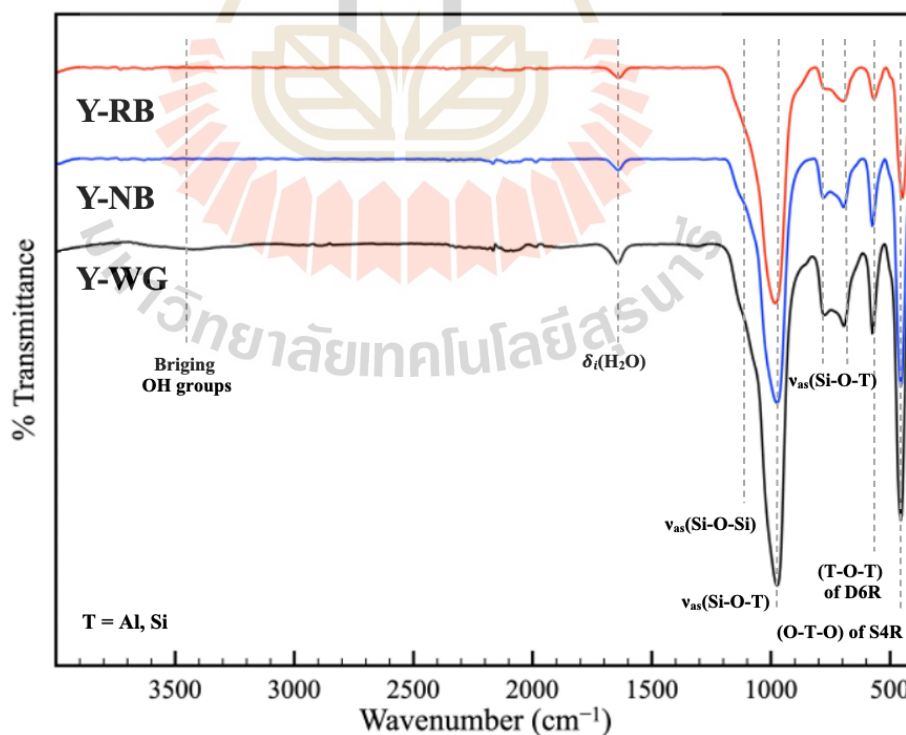


Figure 4.4 FTIR spectra of Y-WG, Y-NB, and Y-RB.

**Figure 4.5** presents the morphologies of NaY samples obtained from FE-SEM/EDX at different magnifications. In the case of Y-WG, the sample exhibits crystals with particle sizes of approximately 2  $\mu\text{m}$  (**Figure 4.5a**). These crystals tend to aggregate, forming particles of varying sizes. Upon closer inspection (**Figure 4.5b,c**), it becomes evident that the aggregate comprises polycrystals of different sizes, suggesting a rapid crystallization process. The Si/Al ratio of Y-WG, as determined by EDX, was 2.06 (**Figure 4.6**).

The SEM image of Y-NB (**Figure 4d**) shows particles of zeolite and some fiber, likely from blade grass. The images at higher magnification (**Figure 4.5e,f**) display the zeolite crystals with a uniform size of approximately 5  $\mu\text{m}$ . The images confirm that the addition of blade grass could prevent the aggregation of zeolite crystals. The Si/Al ratio of Y-NB was 2.05 (**Figure 4.6**). The blade of cogon grass contains a low percentage of silica, which did not have much effect on the Si/Al ratio of the zeolite. This sample also contains a small amount of carbon. The aggregation prevention to produce a uniform size distribution was reported in the synthesis of zeolite RHO using methylcellulose as the space-confinement additive (Liu et al., 2013).

The SEM images of Y-RB depicted in **Figure 4.5g-i** display a mixed phase, comprising fibers, sponge-like materials, and zeolites. The predominant zeolite phase consists of polycrystals with a diameter of approximately 5  $\mu\text{m}$  and some woolball-like particles. This sample exhibits a Si/Al ratio of 2.17 and contains a higher carbon content than Y-NB (**Figure 4.6**).

Regarding paraquat adsorption, both Y-NB and Y-RB seemed to have multilayer adsorption at the initial concentration of 1000 mg/L. It is possible that multilayer adsorption takes place on carbon compound residues or amorphous phases in Y-NB and Y-RB.

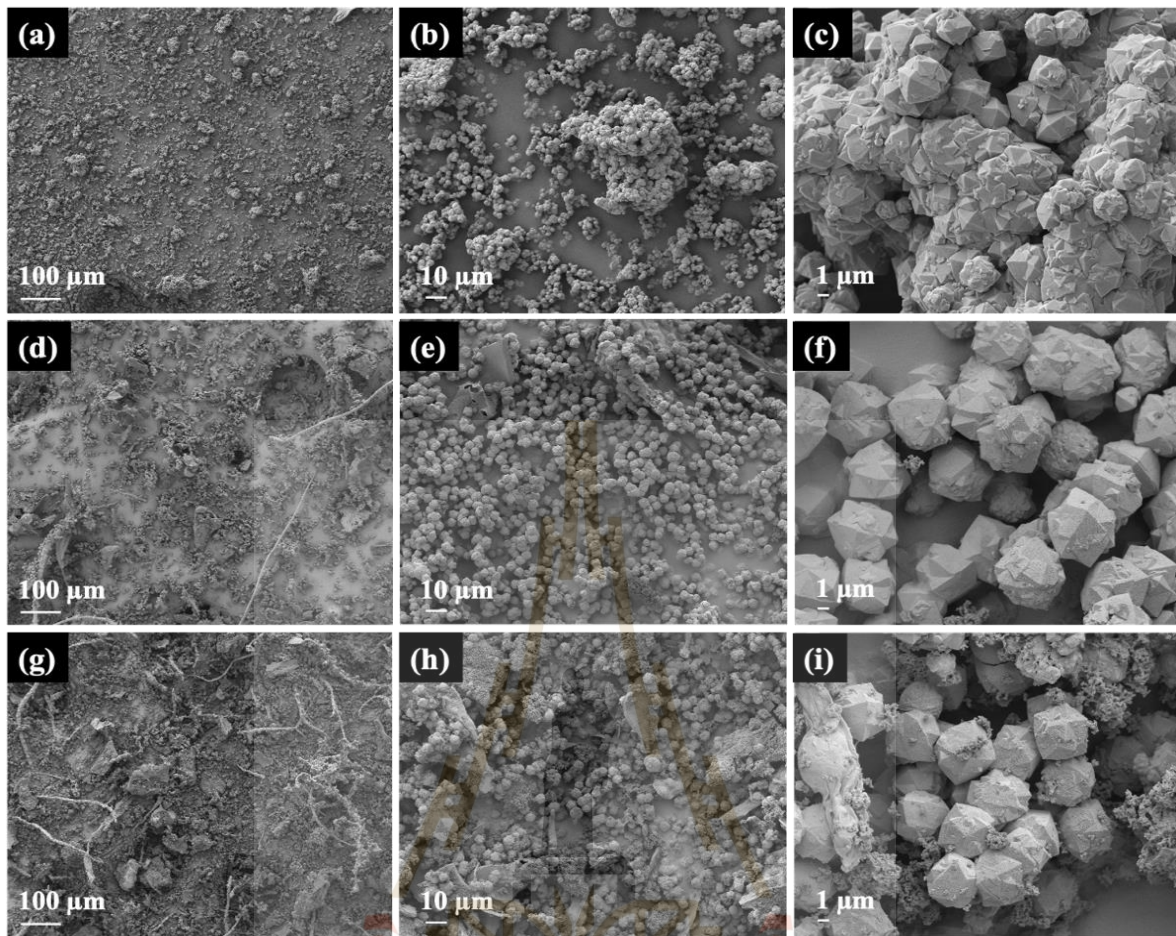


Figure 4.5 SEM images of Y-WG (a–c), Y-NB (d–f), and Y-RB (g–i).

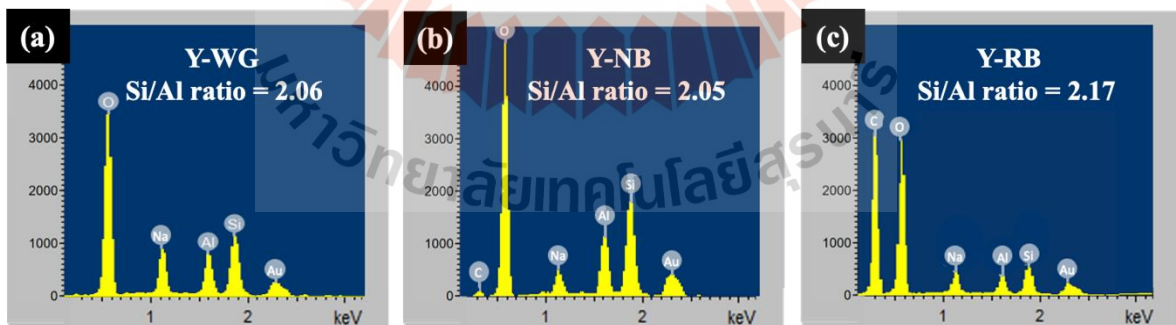


Figure 4.6 EDX spectrum of Y-WG (a), Y-NB (b), and Y-RB (c).

Figure 4.7 presents additional SEM images of Y-NB at different magnifications, showcasing the presence of crystals and sponge-like particles within the sample. It was not that some crystals exhibited an open structure (Figure 4.7b,c), revealing sponge-like materials both internal and external of the crystal. Through EDX point analysis, it was determined that the sponge-like particle is composed of an aluminosilicate material with a Si/Al ratio of 2.08 (Figure 4.8a). Additionally, carbon was detected in the analysis. The existence of these open crystals suggests incomplete crystallization and provides valuable insights into the mechanism of crystal growth.

To understand the composition of Y-NB, the sample was subjected to calcination at 500 °C for 3 h and investigated using SEM/EDX point analysis refer to Table 4.3. The results are presented in Figure 4.8b. The presence of open crystals was still observed. Furthermore, Figure 4.7e illustrates the aggregation of small crystals, leading to the formation of larger particles. The carbon content decreased significantly from 7.1% to 2.8% after calcination refers to Table 4.4 (Liu et al., 2013; Nandanwar et al., 2016; Yuan et al., 2017; Lopes et al., 2018; Kalid et al., 2021; Kundu et al., 2021). The point analysis further confirms that the sponge-like particles consist of aluminosilicate material.

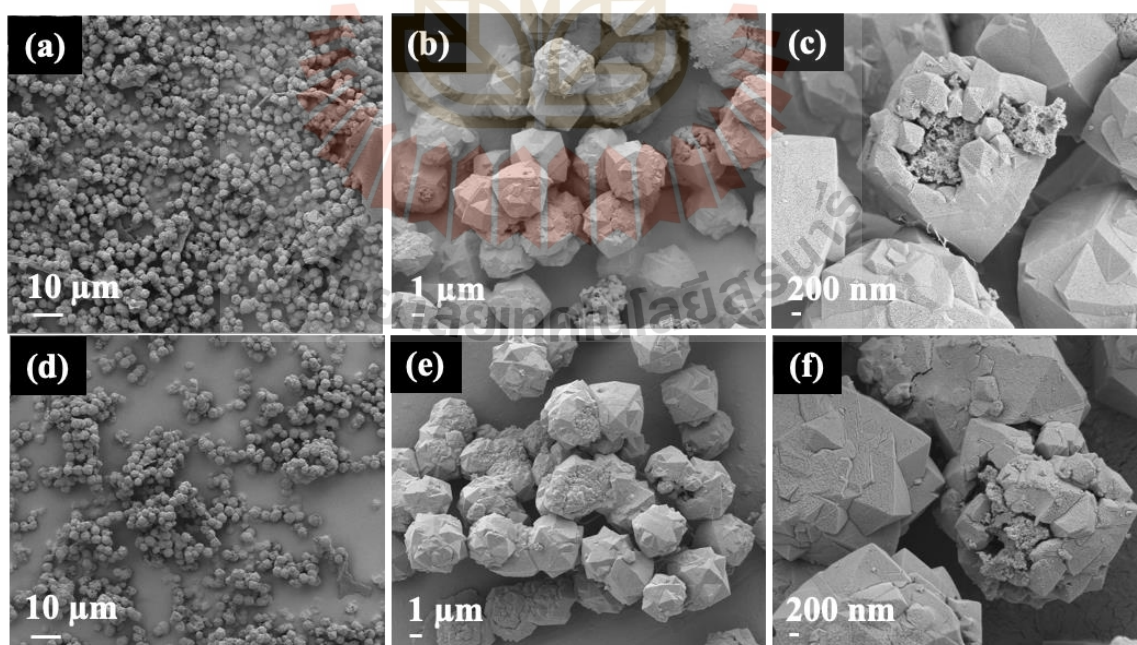
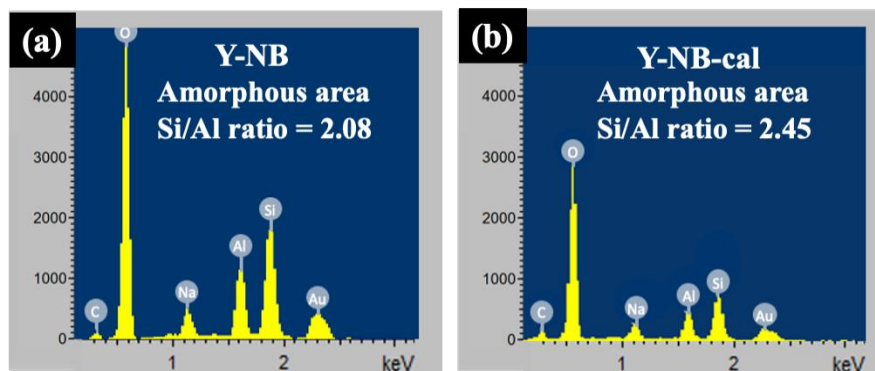


Figure 4.7 SEM images and EDX spectrum of Y-NB (a–c) and calcined Y-NB (d–f).



**Figure 4.8** EDX spectrum of the sponge-like amorphous core of Y-NB: before (a) and after calcination (b).

**Table 4.3** Chemical compositions of the internal zeolite NaY particles.

Sample name	Compositions (%)									
	C		O		Na		Al		Si	
Y-NB	7.1	3.8	56.6	2.8	2.5	0.6	10.9	0.7	22.8	0.6
Y-NB-cal	2.8	0.5	54.0	0.6	4.1	1.5	11.0	0.1	27.0	0.7

Figure 4.9 illustrates the nitrogen adsorption-desorption isotherm for the NaY samples. All samples exhibit a type I isotherm according to the IUPAC classification, indicating a characteristic behavior of microporous materials (Sing, 1985). At low relative pressure ( $P/P_0 = 0.0-0.1$ ), there is a rapid increase in the adsorbed volume attributed to adsorption in the micropores, eventually reaching a plateau as monolayer adsorption occurs. The surface area and pore volume of Y-NB are slightly smaller than those of Y-WG, potentially due to the presence of amorphous particles. Y-RB exhibits the lowest surface area and pore volume, primarily due to a significant amount of the amorphous phase. These findings from the nitrogen adsorption-desorption analysis are consistent with the results obtained from the XRD and SEM observations.

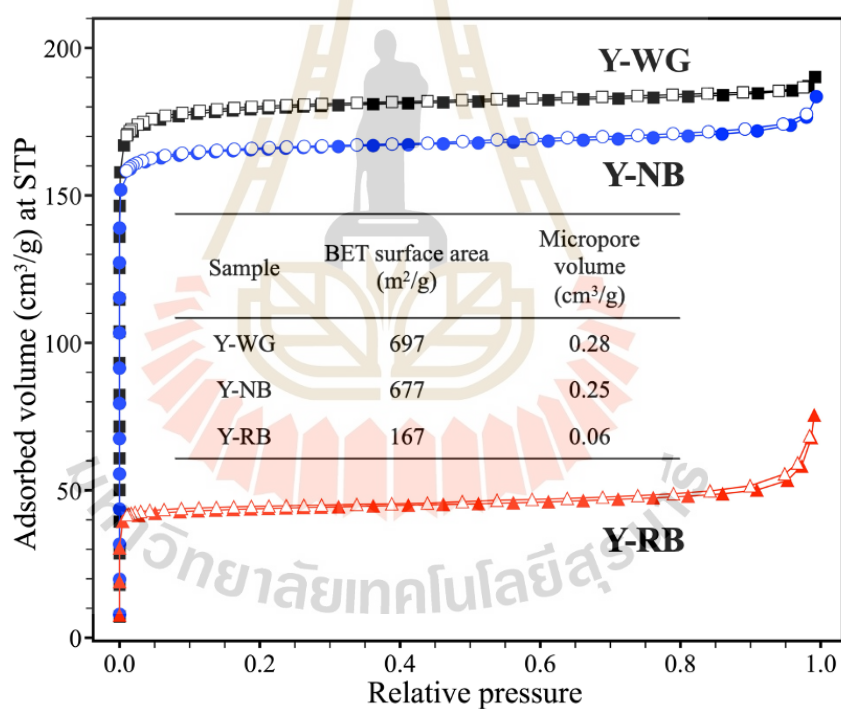


Figure 4.9 Nitrogen adsorption-desorption isotherm and textural properties of Y-WG, Y-NB, and Y-RB; filled symbols = adsorption, and hollow symbols = desorption. Micropore volume was calculated by the  $t$ -plot method.

From the presented results, the addition of cogon grass in the synthesis of NaY appeared to inhibit the aggregation of zeolite crystals. Specifically, non-refluxed grass resulted in NaY with a higher crystallinity and surface area than refluxed grass.

### 4.3.3 Characterization of Y-NB with various grass content

Figure 4.10 presents the XRD pattern of NaY synthesized with varying amounts of non-refluxed grass (NB). The characteristic peaks of zeolite NaY were detected in all samples. Y-1.0NB demonstrated the highest crystallinity, followed by Y-1.5NB, Y-0.5NB, and Y-2.0NB.

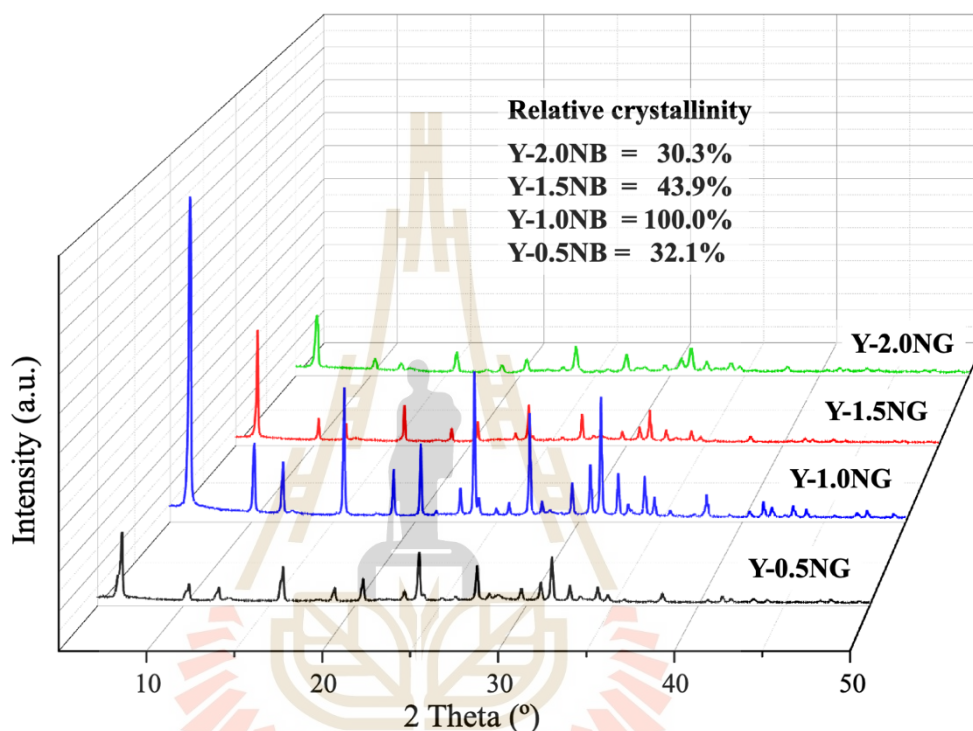


Figure 4.10 XRD pattern of Y-NB synthesized with various grass content.

Figure 4.11 presents the SEM images of Y-0.5NB, Y-1.5NB, and Y-2.0NB at various magnifications. The images of Y-0.5NB (Figure 4.11a–c) reveal the presence of crystals and round particles with an approximate diameter of 5  $\mu\text{m}$  and amorphous particles. These round-shaped and amorphous particles could contribute to the lower intensity in the XRD pattern. The Si/Al ratio of Y-0.5NB from SEM-EDS was 2.08 (Figure 4.12). The images of Y-1.5NB (Figure 4.11d–f) also show crystals, round particles, and sponge-like phases. However, the Si/Al ratios of the crystal and round particles were similar (namely, 2.24 and 2.21).

Lastly, the images of Y-2.0NB (Figure 4.11g–i) show particles of polycrystals and ball wool-like, and cactus-like round particles. The Si/Al ratios of these particles were as follows: 2.11 (crystals), 2.41 (wool ball-like shape), and 2.39 (cactus-like shape). Their

EDX spectra are shown in **Figure 4.12**. The results above clearly indicate that the amount of grass has a significant impact on the synthesis of zeolite NaY. During the base hydrolysis process, lignocellulose undergoes decomposition, yielding sugar, alcohol, and other molecules (Gomes et al., 2017; Pereira et al., 2018). The increased sugar content can reduce the aluminum (Al) content within the zeolite structure. Sugar molecules tend to preferentially bind with silicate precursors rather than aluminate precursors, leading to a higher silicon-to-aluminum (Si/Al) ratio (Nandan et al., 2014; Turner et al., 2019). Concurrently, the presence of aluminum slows down the growth of crystal edges. The optimal amount of grass in the synthesis of zeolite NaY is 1.0 g.

**Figure 4.13** shows the thermogravimetric analysis (TGA) and derivative thermogravimetry (DTG) plots of Y-NB obtained from varying amounts of grass. The TGA plots reveal weight losses in three distinct regions. The weight loss observed in the temperature range up to 250 °C corresponds to the desorption of water (Ribeiro et al., 2019). At higher temperatures, the weight loss is attributed to the decomposition of residual grass fibers. The pyrolysis process, involving the breakdown of cellulose, hemicellulose, and lignin, occurs in the temperature range of 315–400 °C (Yang et al., 2007). Finally, the combustion of the complex structure and the formation of char take place above 400 °C on the Y-1.5NB and Y-2.0NB samples (Kok and Ozgur, 2017).

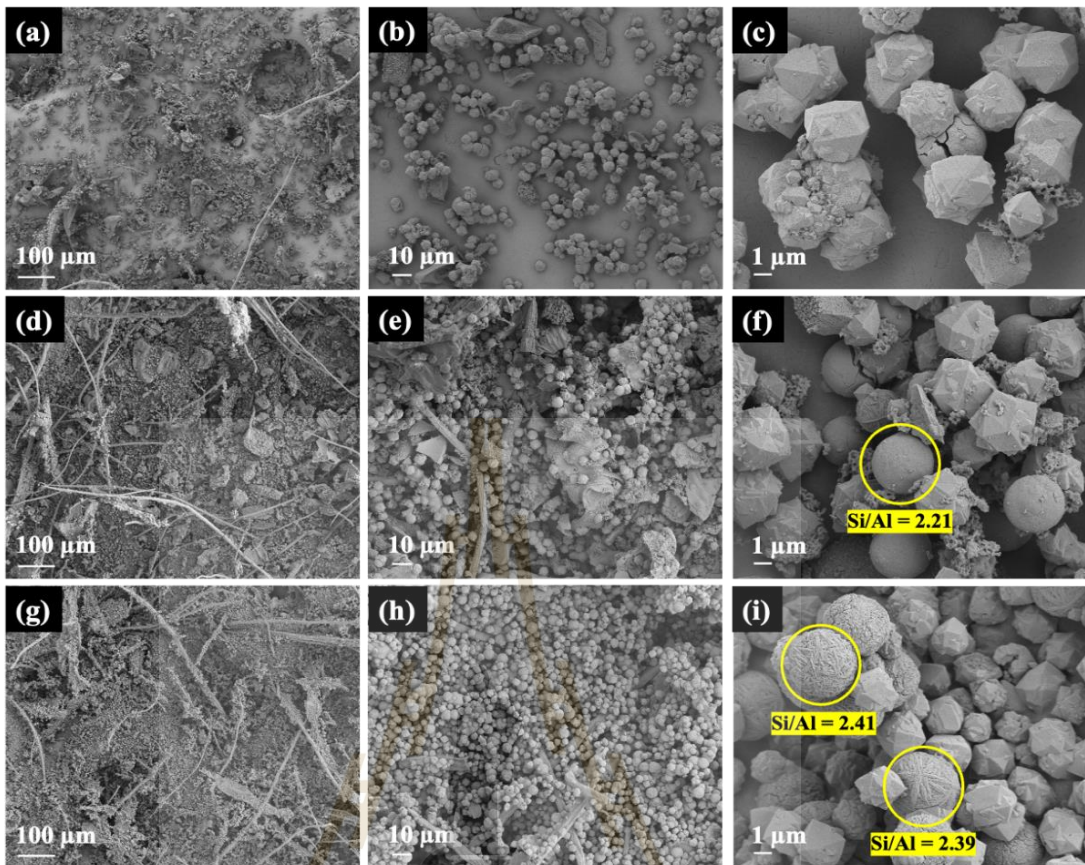


Figure 4.11 SEM images of Y-0.5NB (a-c), Y-1.5NB (d-f), and Y-2.0NB (g-i).

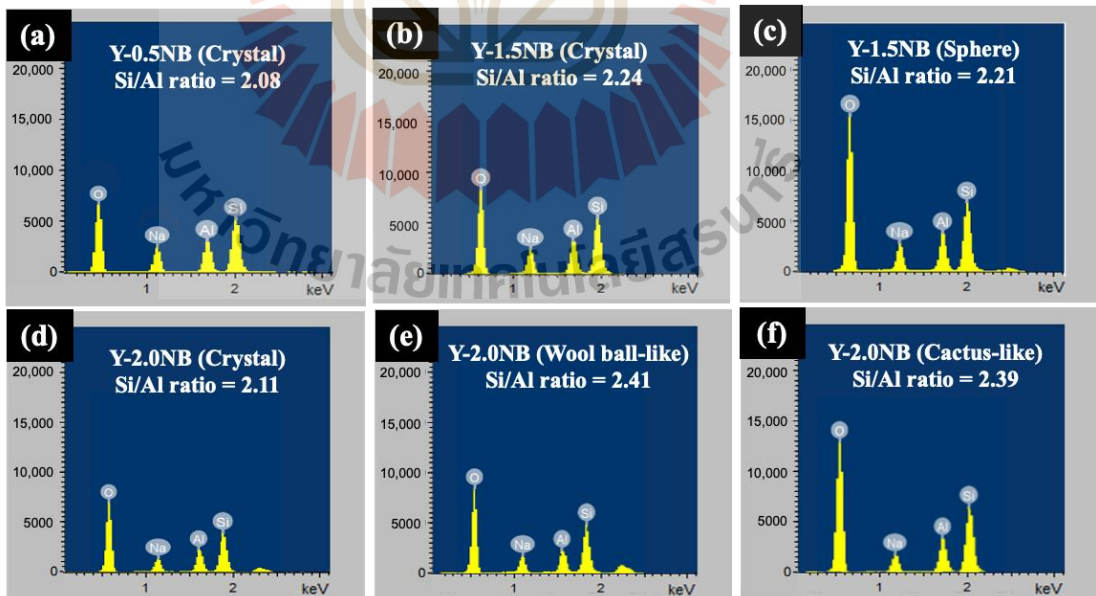


Figure 4.12 EDX spectra of Y-0.5NB (a), Y-1.5NB (b,c), and Y-2.0NB (d-f).

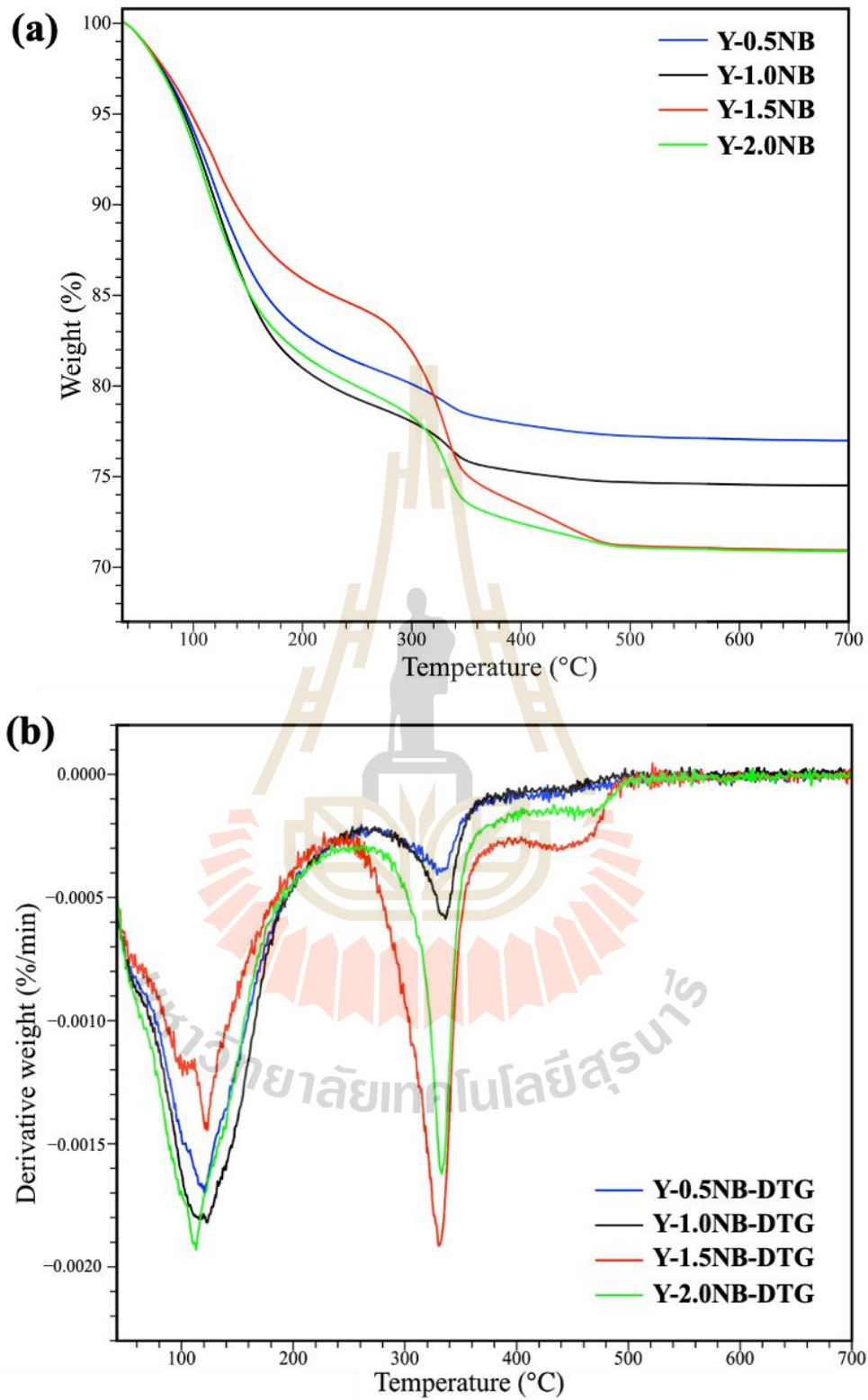


Figure 4.13 TGA (a) and DTG (b) curves of Y-NB with various grass content.

#### 4.3.4 Characterization and paraquat adsorption of non-calcined and calcined Y-NB

Figure 4.14a illustrates the XRD patterns of non-calcined and calcined Y-NB synthesized with 1.0 g of non-refluxed blade. All samples reveal the characteristic peaks of zeolite NaY. Notably, it was observed before from the same NaY sample that the intensity of the first peak from the Bruker D2 diffractometer is lower than that of the Bruker D8. The weights of calcined samples 1 and 2 were 10.7% and 8.9%, respectively, which are lower than the non-calcined samples due to the loss of water and organic content. SEM images of non-calcined and calcined samples display good dispersion and a Si/Al ratio of 1.9. The paraquat adsorption of Y-NB samples reached a plateau at higher initial concentrations, as depicted in Figure 4.14b, indicating the formation of a monolayer. The adsorption behavior aligns with the report by Keawkumay et al. (2019). From these results, it can be conclude that the remaining organic content in the zeolite samples and calcination did not affect the adsorption behavior of zeolite NaY.

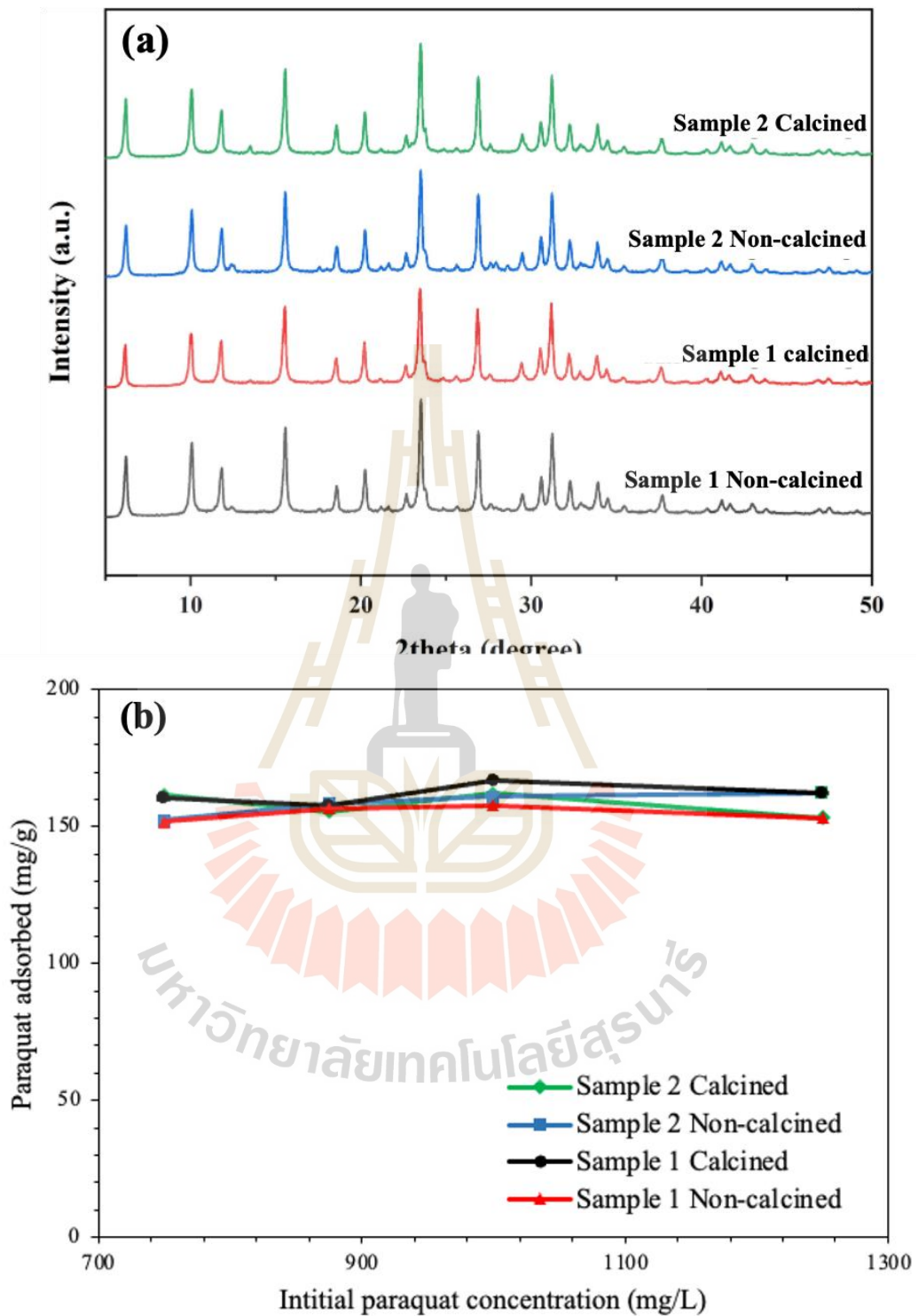


Figure 4.14 XRD patterns of non-calcined and calcined Y-NB (a) and paraquat adsorption of Y-NB and Y-WG from various initial concentrations (b).

#### 4.4 Conclusions

The addition of non-refluxed and refluxed blade (NB and RB) was incorporated into the synthesis of zeolite NaY, resulting in the production of Y-NB and Y-RB, respectively. For comparison, NaY was also synthesized without the addition of grass (Y-WG). All samples exhibited paraquat adsorption behavior consistent with the Langmuir model, occurring on the zeolite. Y-NB demonstrated comparable crystallinity and surface area to Y-WG, along with better particle dispersion. In contrast, Y-RB displayed the lowest crystallinity, surface area, and paraquat adsorption capacity. This study highlights the potential of cogon grass to produce zeolite with uniform crystal size and good dispersion.

Future research directions aim to achieve a deeper understanding of the role of compounds derived from cogon grass during zeolite synthesis, as well as to explore distinctive applications of the uniform-sized zeolite. This work exemplifies the potential of cogon grass as an abundant and natural resource for the development of sustainable and environmentally friendly materials in adsorption and catalysis applications.

#### 4.5 References

- Amin, F. R., Khalid, H., Zhang, H., Rahman, S. U., Zhang, R., Liu, G., and Chen, C. (2017). Pretreatment methods of lignocellulosic biomass for anaerobic digestion. *AMB Express*, 7(1), 72.
- Baerlocher, C. (2008). Database of zeolite structures. <http://www.iza-structure.org/databases/> (accessed on 26 June 2023).
- Bunmai, K., Osakoo, N., Deekamwong, K., Rongchapo, W., Keawkumay, C., Chanlek, N., Prayoonpokarach, S., and Wittayakun, J. (2018). Extraction of silica from cogon grass and utilization for synthesis of zeolite NaY by conventional and microwave-assisted hydrothermal methods. *J. Taiwan Inst. Chem. Eng.*, 83, 152-158.
- Dozier, H., Gaffney, J. F., McDonald, S. K., Johnson, E. R., and Shilling, D. G. (1998). Cogongrass in the United States: history, ecology, impacts, and management. *Weed Technol.*, 12(4), 737-743.

- Estrada, J. A., and Flory, S. L. (2015). Cogongrass (*Imperata cylindrica*) invasions in the US: Mechanisms, impacts, and threats to biodiversity. *Glob. Ecol. Conserv.*, 3, 1-10.
- Gomes, E. S., Lutzweiler, G., Losch, P., Silva, A. V., Bernardon, C., Parkhomenko, K., Pereira, M. M., and Louis, B. (2017). Strategy to design zeolite catalysts in the presence of biomass. *Micropor. Mesopor. Mat.*, 254, 28-36.
- Haque, M. A., Barman, D. N., Kim, M. K., Yun, H. D., and Cho, K. M. (2016). Cogon grass (*Imperata cylindrica*), a potential biomass candidate for bioethanol: cell wall structural changes enhancing hydrolysis in a mild alkali pretreatment regime. *J. Sci. Food Agric.*, 96(5), 1790-1797.
- Kandhola, G., Djioleu, A., Rajan, K., Labbé, N., Sakon, J., Carrier, D. J., and Kim, J.-W. (2020). Maximizing production of cellulose nanocrystals and nanofibers from pre-extracted loblolly pine kraft pulp: a response surface approach. *Bioresour. Bioprocess.*, 7(1).
- Karge, H. G. (2001). Characterization by IR spectroscopy. In *Verified syntheses of zeolitic materials*. Elsevier Sci., 69-71.
- Keawkumay, C., Rongchapo, W., Sosa, N., Suthirakun, S., Koleva, I. Z., Aleksandrov, H. A., Vayssilov, G. N., and Wittayakun, J. (2019). Paraquat adsorption on NaY zeolite at various Si/Al ratios: A combined experimental and computational study. *Mater. Chem. Phys.*, 238, 121824.
- Kefli, A. A., Khasri, A., Rohaizad, N. M., and Ahmad, M. A. (2017). Microwave assisted pyrolysis of *Imperata Cylindrica* with ionic liquids pre-treatment. *Int. J. Petrochem. Res.*, 1(1), 73-75.
- Khalid, F. E., Ahmad, S. A., Zakaria, N. N., Shaharuddin, N. A., Sabri, S., Azmi, A. A., Khalil, K. A., Verasoundarapandian, G., Gomez-Fuentes, C., and Zulkharnain, A. (2021). Application of cogon grass (*Imperata cylindrica*) as biosorbent in diesel-filter system for oil spill removal. *Agronomy*, 11(11), 2273.
- Kok, M. V., and Ozgur, E. (2017). Characterization of lignocellulose biomass and model compounds by thermogravimetry. *Energy Sources A Recovery Util. Environ. Eff.*, 39(2), 134-139.

- Kow, K.-W., Yusoff, R., Aziz, A. R. A., and Abdullah, E. C. (2014). Characterisation of bio-silica synthesised from cogon grass (*Imperata cylindrica*). *Powder Technol.*, *254*, 206-213.
- Kulawong, S., Chanlek, N., and Osakoo, N. (2020). Facile synthesis of hierarchical structure of NaY zeolite using silica from cogon grass for acid blue 185 removal from water. *J. Environ. Chem. Eng.*, *8*(5), 104114.
- Kundu, C., Samudrala, S. P., Kibria, M. A., and Bhattacharya, S. (2021). One-step peracetic acid pretreatment of hardwood and softwood biomass for platform chemicals production. *Sci. Rep.*, *11*(1), 11183.
- Lewis, D., Freeman, C., and Catlow, C. (1995). Predicting the templating ability of organic additives for the synthesis of microporous materials. *J. Phys. Chem.*, *99*(28), 11194-11202.
- Li, J., Gao, M., Yan, W., and Yu, J. (2023). Regulation of the Si/Al ratios and Al distributions of zeolites and their impact on properties. *Chem. Sci.*, *14*(8), 1935-1959.
- Li, X., Han, H., Evangelou, N., Wichrowski, N. J., Lu, P., Xu, W., Hwang, S.-J., Zhao, W., Song, C., and Guo, X. (2023). Machine learning-assisted crystal engineering of a zeolite. *Nat. Commun.*, *14*(1), 3152.
- Liu, X., Zhang, X., Chen, Z., and Tan, X. (2013). Hydrothermal synthesis of zeolite Rho using methylcellulose as the space-confinement additive. *Ceram. Int.*, *39*(5), 5453-5458.
- Lopes, J. d. O., Garcia, R. A., and Souza, N. D. d. (2018). Infrared spectroscopy of the surface of thermally-modified teak juvenile wood. *Maderas. Cienc. Tecnol.*, *20*(4), 737-746.
- Louis, B., Gomes, E. S., Coelho, T., Lutzweiler, G., Losch, P., Silva, A. V., Faro, A. C., Romero, T., Osman, M. B., Balanqueux, A., Bernardon, C., and Pereira, M. M. (2016). Influence of Biomass Residues on the Metastability of Zeolite Structures. *Nanosci. Nanotech. Lett.*, *8*(11), 917-923.
- Louis, B., Gomes, E. S., Losch, P., Lutzweiler, G., Coelho, T., Faro, A., Pinto, J. F., Cardoso, C. S., Silva, A. V., and Pereira, M. M. (2017). Biomass-assisted Zeolite Syntheses as a Tool for Designing New Acid Catalysts. *ChemCatChem*, *9*(12), 2065-2079.

- Mintova, S. (2016). Verified syntheses of zeolitic materials. *The Synthesis Commission of the International Zeolite Association*, 215-223.
- Mintova, S., and Valtchev, V. (1996). Deposition of zeolite A on vegetal fibers. *Zeolites*, 16(1), 31-34.
- Nandan, D., Saxena, S. K., and Viswanadham, N. (2014). Synthesis of hierarchical ZSM-5 using glucose as a templating precursor. *J. Mater. Chem. A*, 2(4), 1054-1059.
- Nandanwar, R., Chaudhari, A., and Ekhe, J. (2016). Nitrobenzene oxidation for isolation of value added products from industrial waste lignin. *J. Chem. Biol. Phys. Sci.*, 6, 501-513.
- Ocampo, F., Cunha, J. A., de Lima Santos, M. R., Tessonier, J. P., Pereira, M. M., and Louis, B. (2010). Synthesis of zeolite crystals with unusual morphology: Application in acid catalysis. *Appl. Catal. A Gen.*, 390(1-2), 102-109.
- Pereira, M. M., Gomes, E. S., Silva, A. V., Pinar, A. B., Willinger, M. G., Shanmugam, S., Chizallet, C., Laugel, G., Losch, P., and Louis, B. (2018). Biomass-mediated ZSM-5 zeolite synthesis: when self-assembly allows to cross the Si/Al lower limit. *Chem. Sci.*, 9(31), 6532-6539.
- Ribeiro, S. P. d. S., Martins, R. C., Barbosa, G. M., Rocha, M. A. d. F., Landesmann, A., Nascimento, M. A. C., and Nascimento, R. S. V. (2019). Influence of the zeolite acidity on its synergistic action with a flame-retarding polymeric intumescent formulation. *J. Mater. Sci.*, 55(2), 619-630.
- Rongchapo, W., Keawkumay, C., Osakoo, N., Deekamwong, K., Chanlek, N., Prayoonpokarach, S., and Wittayakun, J. (2017). Comprehension of paraquat adsorption on faujasite zeolite X and Y in sodium form. *Adsorpt. Sci. Technol.*, 36(1-2), 684-693.
- Rongchapo, W., Sোধiphun, O., Rintramee, K., Prayoonpokarach, S., and Wittayakun, J. (2013). Paraquat adsorption on porous materials synthesized from rice husk silica. *Water Sci. Technol.*, 68(4), 863-869.
- Sing, K. S. (1985). Reporting physisorption data for gas/solid systems with special reference to the determination of surface area and porosity (Recommendations 1984). *Pure Appl. Chem.*, 57(4), 603-619.

- Surtiningsih, T., Agustina, D., and Manuhara, Y. S. W. (2018). Hydrolysis of imperata cylindrica (L.) Beauv. By penicillium sp., aspergillus niger and trichoderma viride as bioethanol basic ingredient production. *Biosci. Res.*, 15(3), 2318-2326.
- Turner, S. J., Chen, J., Slawin, A. M. Z., and Zhou, W. (2019). New mechanism for the nucleation and growth of large zeolite X crystals in the presence of triethanolamine. *Chem. Comm.*, 55(6), 862-865.
- Valtchev, V., Mintova, S., Vulchev, I., and Lazarova, V. (1994). Influence of reactive radicals in cellulose fibres on the formation of zeolite coatings. *J. Chem. Soc. Chem. Commun.*, (18), 2087-2088.
- Xu, F., Sun, J. X., Geng, Z. C., Liu, C. F., Ren, J. L., Sun, R. C., Fowler, P., and Baird, M. S. (2007). Comparative study of water-soluble and alkali-soluble hemicelluloses from perennial ryegrass leaves (*Lolium persee*). *Carbohydr. Polym.*, 67(1), 56-65.
- Yandoc, C. B., Charudattan, R., and Shilling, D. G. (2004). Suppression of cogongrass (*Imperata cylindrica*) by a bioherbicidal fungus and plant competition. *Weed Sci.*, 52(4), 649-653.
- Yang, H., Yan, R., Chen, H., Lee, D. H., and Zheng, C. (2007). Characteristics of hemicellulose, cellulose and lignin pyrolysis. *Fuel*, 86(12-13), 1781-1788.
- Yuan, Z., Kapu, N. S., and Martinez, D. M. (2017). An eco-friendly scheme to eliminate silica problems during bamboo biomass fractionation. *Nord. Pulp Pap. Res. J.*, 32(1), 4-13.
- Zarib, N., Abdullah, S., and Jusri, N. (2020). Effect of acid treatment on extraction of silica from cogon grass by using  $C_6H_8O_7$  and HCL Acid. *IOP Conf. Ser. Mater. Sci. Eng.*, 834, 012067.
- Zhao, J., Yin, Y., Li, Y., Chen, W., and Liu, B. (2016). Synthesis and characterization of mesoporous zeolite Y by using block copolymers as templates. *Chem. Eng. J.*, 284, 405-411.
- Zhu, D., Wang, L., Fan, D., Yan, N., Huang, S., Xu, S., Guo, P., Yang, M., Zhang, J., Tian, P., and Liu, Z. (2020). A Bottom-Up Strategy for the Synthesis of Highly Siliceous Faujasite-Type Zeolite. *Adv. Mater.*, 32(26), 2000272.

## CHAPTER V

### POTASSIUM SUPPORTED ON VARIOUS CRYSTAL SIZES OF ZEOLITE NaY FOR TRANSESTERIFICATION OF PALM OIL

#### 5.1 INTRODUCTION

Renewable and alternative energy sources are in demand for environmental and economic sustainability due to the concern of fossil fuel extinction and contribution to climate change. Biodiesel is biodegradable and environment-friendly nature. It has excellent properties such as high combustion, high flash point, lower CO<sub>2</sub> emission (Changmai et al., 2020). The utilization of edible vegetable oil can minimize the cost of biodiesel production. In Thailand, palm oil is one popular feedstock.

Biodiesel is usually produced by the transesterification of triglyceride and methanol in the presence of a basic catalyst. Typically, the catalysts for the reaction could be either homogeneous or heterogeneous. Potassium carbonate exhibited excellent biodiesel yield that reached 98.7% (Zhang et al., 2020). Unfortunately, the homogeneous catalysts provided complicated post-process. The heterogeneous catalysts are considered as a green technology because there is less amount of wastewater and easy reusability.

The active species are also important factor to enhance activity of transesterification. The K ions and/or carbonate species on zeolite NaY framework may promote the catalytic performance. Besides, the catalyst preparation by ultrasound-assisted impregnation with potassium acetate buffer gave a better dispersion of active site than that by the conventional impregnation method (Rakmae et al., 2016).

Among several solids, zeolites are interesting because they contain high surface area and microporosity, improving the dispersion of active site. Zeolite NaY was previously used as a support in transesterification. Potassium carbonate supported on NaY showed the yield of biodiesel up to 70-90% (Supamathanon et al., 2011; Montalbo et al., 2013; Rakmae et al. 2016; Maneechot et al., 2021; Kosawatthanakun et al., 2022).

Nevertheless, the interaction between the catalyst and reactants poses a challenge for micro-sized zeolites, resulting in less effectiveness for biodiesel production (Pang et al., 2020; Supamathanon et al., 2023). Thus, the utilization of different crystal sizes or mixed phase of amorphous in the zeolite may enhance the accessibility of reactant to the active site.

Zeolite with different crystal sizes and phases could be synthesized by variation of water content in the synthesis gel (Huang et al., 2010; Shirazian et al., 2014; Mintova et al., 2016; Keawkumay et al., 2019). A zeolite gel with low water content promotes the formation of smaller zeolite nanocrystal. This is due to the increment of the basicity that facilitates the dissolution of sodium silicate, thereby enabling the crystallization of zeolite crystals. Conversely, lower basicity or high water content reduces the dissolution of silicate anions, leading to the production of the amorphous aluminosilicate (Isa et al., 2018).

Therefore, the goal of this work was to prepare potassium catalyst from potassium acetate buffer by impregnation method with ultrasound. Then the effect of crystal sizes, phases, and the active species of these samples are studied. Consequently, all catalysts are tested in transesterification of palm oil.

## 5.2 Experiment

### 5.2.1 Chemicals

Chemicals for zeolite synthesis were silicon dioxide RPE (99%, Sigma-Aldrich, *St. Louis, USA*), sodium aluminate (95%, Sigma-Aldrich, *St. Louis, USA*), and sodium hydroxide (97%, Carlo Erba, *Cornaredo, Italy*). Potassium acetate (99%, Carlo Erba, *Cornaredo, Italy*) and glacial acetic acid (99.7%, RCI Labscan, *Bangkok, Thailand*) were used for catalyst preparation. Refined palm olein from pericarp (food grade, Morakot Industries Public Co. Ltd., *Bangkok, Thailand*) and methanol (99%, Carlo Erba, *Cornaredo, Italy*) were applied in the transesterification reaction. Methyl nonadecanoate ( $C_{19}(CH_3(CH_2)_{17}COOCH_3$ , 98%, Sigma-Aldrich, *St. Louis, USA*) was utilized as a standard for biodiesel detection.

### 5.2.2 Zeolite NaY synthesis

Zeolite NaY were synthesized using a modified procedure based on Keawkumay et al. (2019), adjusting the water content in seed and feed gel as displayed. The Si/Al ratio ranged 2.0 to 2.2.  $\text{Na}_2\text{SiO}_3$  solution was prepared by dissolving of 57.4 g fumed silica in NaOH solution prepared from dissolving of 23.0 g of NaOH in 119.6 g deionized (DI) water. A seed gel was prepared in a polypropylene (PP) bottle with a molar ratio of  $10.67\text{Na}_2\text{O}:1.0\text{Al}_2\text{O}_3:10.0\text{SiO}_2:x\text{H}_2\text{O}$  ( $x = 180, 300, \text{ and } 400$ ). Then the mixture is stirred, capped, and aged at room temperature for 24 h. A feedstock gel with molar ratio  $4.67\text{Na}_2\text{O}:1.0\text{Al}_2\text{O}_3:10.0\text{SiO}_2:x\text{H}_2\text{O}$  ( $x = 180, 300, \text{ and } 400$ ) was prepared following a similar procedure to the seed gel, excepting without aging. Subsequently, the feedstock gel was gently added to a seed gel, stirred for 10 min, and aged in a closed PP bottle at ambient temperature for 24 h. The resulting overall gel with molar ratio  $5.5\text{Na}_2\text{O}:1.0\text{Al}_2\text{O}_3:10.0\text{SiO}_2:x\text{H}_2\text{O}$  ( $x = 180, 300, \text{ and } 400$ ) was further crystallized under the hydrothermal condition at 90 °C for 24 h. The synthesized samples were labeled as NaY0.25, NaY1.0, and NaY2.0, respectively.

### 5.2.3 Preparation of catalysts through an ultrasound-assisted impregnation

Catalysts consisting of potassium carbonate supported on zeolite NaY were prepared using ultrasound-assisted impregnation method detailed in the literature (Rakmae et al., 2016). A 12 wt.% of potassium acetate buffer (pH 5) was created by dissolving 5.7 g of potassium acetate in 1.0 M acetic acid and adjusting the solution to 25.0 mL. The zeolite was dried at 90 °C for 24 h. Subsequently, the buffer was added dropwise to 2.0 g of dried NaY0.25 (1.2 mL), NaY1.0 (1.0 mL), NaY2.0 (2.8 mL). The mixture was sonicated at 37 Hz with a power of 80 W (Elmasonic E30H model, Elma, Switzerland) for 10 min, followed by stirring with magnetic bar for 10 min. Both samples were left at ambient temperature for 24 h and dried at 80 °C for 24 h. The K/NaY0.25\_IM, K/NaY1.0\_IM, and K/NaY2.0\_IM were obtained. These samples were further calcined at 500 °C for 3 h under atmospheric conditions with a heating rate 1 °C/min. The final samples were denoted as K/NaY0.25, K/NaY1.0, and K/NaY2.0, respectively.

### 5.2.4 Catalyst characterization

The zeolite structure and potassium species were measured using X-ray diffraction (XRD, Bruker D8 ADVANCE, *Billerica, USA*) with Cu K $\alpha$  radiation operated with a voltage of 40 kV and a current of 40 mA. All patterns were collected by a  $2\theta$  scan range from 5 to 50° with a step size of 0.02° at a scan speed of 0.2 s/step.

The functional groups of the zeolite and catalysts were investigated by Fourier-transform infrared spectroscopy (FT-IR, Bruker Tensor 27, *Ettlingen, Germany*) using Attenuated Total Reflectance (ATR) mode. The spectrum was recorded from 4000 to 400 cm<sup>-1</sup> with a resolution of 4 cm<sup>-1</sup> and 64 scans.

The thermogravimetric analysis (TGA), differential thermogravimetric (DTG), and differential scanning calorimetry (DSC) were conducted (Mettler Toledo TGA/DSC1, *Schwerzenbach, Switzerland*). The samples were heated from ambient to 600 °C at a scan rate 10.0 °C/min, using a sample mass of 20 mg under air-zero.

The morphology, particle size, distribution, and their composition were determined by field-emission scanning electron microscopy with energy-dispersive spectroscopy (FE-SEM/EDS, JEOL JSM 7800F, *Akishima, Tokyo, Japan*) and high-resolution transmission electron microscopy (HRTEM, Talos F200X, *Thermo Fisher Scientific, Waltham, USA*).

The isotherms of all samples were measured by N<sub>2</sub> adsorption–desorption (micromeritics model 3flex, 2020, *Georgia, USA*). The dried samples (0.1-0.2 g) were degassed at 300 °C for 10 h until reaching a final pressure of 5×10<sup>-6</sup> mmHg. The specific surface areas were calculated by the Brunauer–Emmett–Teller (BET) method. The micropore volume, total volume, and external surface area were derived from *t*-plot method.

### 5.2.5 Transesterification of palm oil

A catalyst (0.2 g) was added in 50 mL one-necked round bottom flask, following methanol (3.7 mL) and palm oil (5.0 g), respectively. The reaction was performed within a reflux setup at 60 °C for 3 h in silicone oil bath. The product was separated by centrifugation (4000 rpm, 5 min). The liquid phase was evaporated to remove methanol by a rotary evaporator at 50 °C. Then the mixture was transferred to a

separatory funnel and left to stand overnight. The produced biodiesel in the upper layer was collected.

The quantitative content of biodiesel from the reaction were determined based on the biodiesel test method EN14103 by gas chromatography (Shimadzu, Model GC-14A Gas Chromatograph, *Kyoto, Japan*) equipped with a flame ionization detector (FID) and 30 m dimethylpolysiloxane column (SGE, BP1) with 0.53 mm id and 3  $\mu\text{m}$  film thickness. The initial column temperature was held at 80  $^{\circ}\text{C}$  for 1 min and before ramping up to 260  $^{\circ}\text{C}$  with a heating rate 10  $^{\circ}\text{C}/\text{min}$ . Methyl nonadecanoate ( $\text{C}_{19}$ ) was used as an internal standard. The yield of biodiesel was obtained from Eq (5.1).

$$\text{Biodiesel Yield (\%)} = \frac{(\sum A) - AEI}{AEI} \times \frac{CEI \times VEI}{m} \times 100 \quad (5.1)$$

where  $\sum A$  is total peak areas, which was acquired by GC,  $AEI$  is a peak area of Methyl nonadecanoate ( $\text{C}_{19}$ ),  $CEI$  is a concentration of the  $\text{C}_{19}$  solution (5.0 mg/mL), and  $VEI$  is volume of the  $\text{C}_{19}$  solution (1.0 mL), while  $m$  is a sample mass (50.0 mg).

### 5.2.6 Catalyst stability

The transesterification reaction was performed from **Section 5.2.5**. Solid catalyst was separated from the solution by centrifugation (4000 rpm, 5 min). It was washed with 10 mL of methanol and 10 mL of hexane before dried in a conventional oven at 90  $^{\circ}\text{C}$  overnight. The spent catalyst was performed with a similar process described in **Section 5.2.5**. The samples were labeled SP in front of their name.

### 5.2.7 Deactivation of catalysts

The transesterification reaction was performed from **Section 5.2.5**. After that, the catalyst was removed by centrifugation (4000 rpm, 5 min) and the methanol was evaporated out of the product by rotary evaporator at 50  $^{\circ}\text{C}$ . Then a half of final solution (2.5 g) was added to the mixture, consisting of palm oil (2.5 g) and methanol (2.9 g). Then the reaction continuously stirred at 60  $^{\circ}\text{C}$  for 3 h in a silicone oil bath. Finally, the mixture was cool down at room temperature, removed the methanol, and kept it overnight.

## 5.3 Result and discussion

### 5.3.1 Characterization of catalysts

Figure 5.1a-c show TGA/DTG thermograms of potassium acetate impregnated on NaY with varying crystal sizes and phases. The weight loss observed in NaY primarily occurred mainly between 380 to 480 °C, attributed to the decomposition of potassium acetate. Remarkably, our findings are consistent with a similar TGA results reported by Rakmae et al. (2016) and Manadee et al. (2017), which indicate acetate decomposition to carbonate at 480 °C. Moreover, Figure 5.1d-f exhibit an endothermic peak around 420 °C in the DSC profiles, corresponding to an 11-13% weight loss observed in TGA curves. This weight loss percentage suggest the decomposition process. Therefore, the as-prepared samples were calcined at 500 °C.

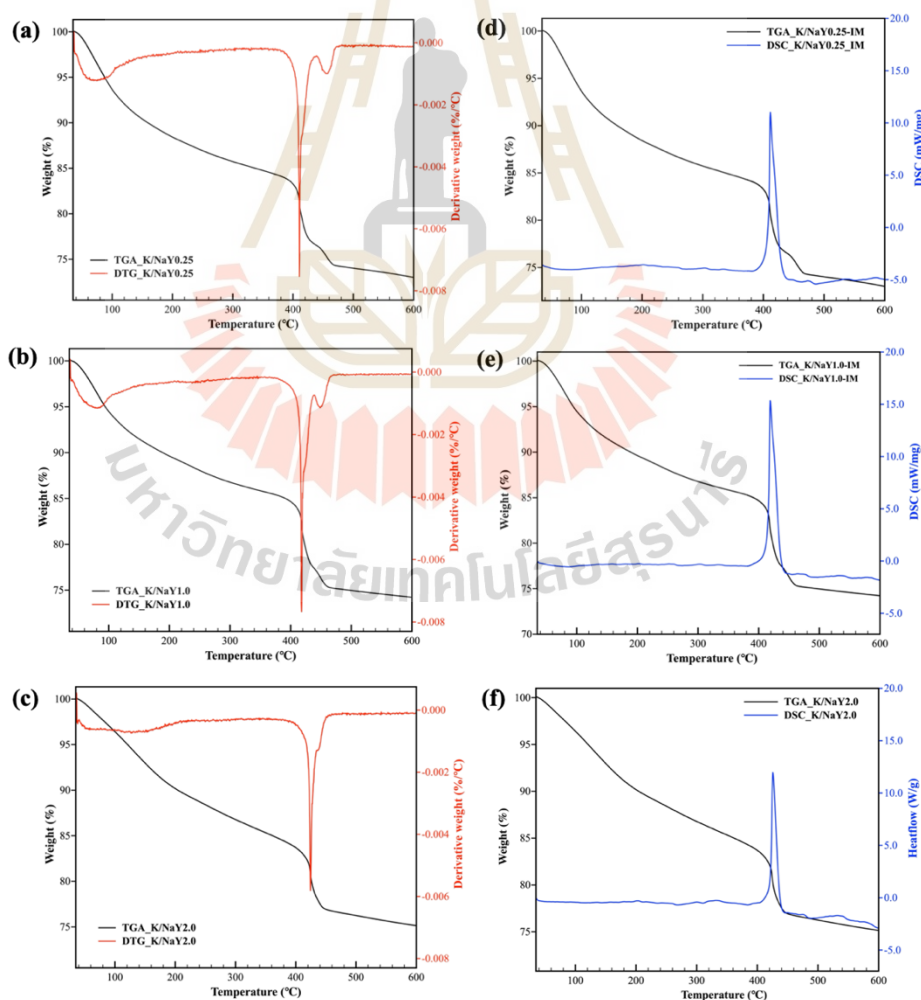


Figure 5.1 TGA/DTG (a-c) and TGA/DSC (e-f) curves of impregnated NaY in various crystal sizes.

**Figure 5.2** displays the XRD pattern of impregnated and calcined K/NaY samples compared with bare zeolites. Zeolite NaY exhibited peak positions consistent with the database of the international zeolite association (IZA) (Baerlocher, 2008; Mintova, 2016). The characteristic peaks of zeolite NaY remained noticeable in all impregnated samples, but with a significant decrease in peak intensities. Additionally, the characteristic peaks of potassium acetate were observed. Following calcination, these peaks were disappeared from all samples, suggesting complete decomposition of acetate into carbonate (Afzal et al., 1991). This deduction was corroborated by TGA analysis as depicted in **Figure 5.1**. Therefore, the calcination process effectively transforms the phase of the potassium acetate into potassium carbonate. Nevertheless, the XRD peak intensities of all calcined samples were lower than those bare samples. These results indicated that the zeolite crystal planes could be covered by potassium species, or the structure could collapse. This situation was similar to the observation by Rakmae et al. (2016) and Kosawatthanakun et al. (2019).

**Figure 5.3** demonstrates the functional groups in the samples, while **Table 5.1** illustrates the band assignment details corresponding to zeolite structure and potassium species. The functional groups of zeolites were observed within the range 450-1650  $\text{cm}^{-1}$ . The peaks at 1412 and 1574  $\text{cm}^{-1}$  were identified as potassium acetate (Zhong et al., 2018; Kosawatthanakun et al., 2019). These peaks disappeared during calcination, indicating complete decomposition and agreeing with XRD and TGA results. Moreover, these peaks of carbonate species were appeared. The asymmetric stretching of  $\text{CO}_3^{2-}$  or monodentate carbonate was exclusively present at 1398  $\text{cm}^{-1}$  (Du et al., 2010; Kosawatthanakun et al., 2019) in micron-sized samples. Interestingly, the peak at 1450  $\text{cm}^{-1}$  was associated with the symmetric stretching of  $\text{COO}^-$  or free carbonate (Weilach et al., 2011; Föttinger et al., 2017), which evident in K/NaY0.25. Considering these assignments, it is a reasonable to conclude that upon acetate on our catalysts mainly monodentate carbonate and/or free carbonate were produced. These carbonates are likely the dominant species contributing to the transesterification reaction.

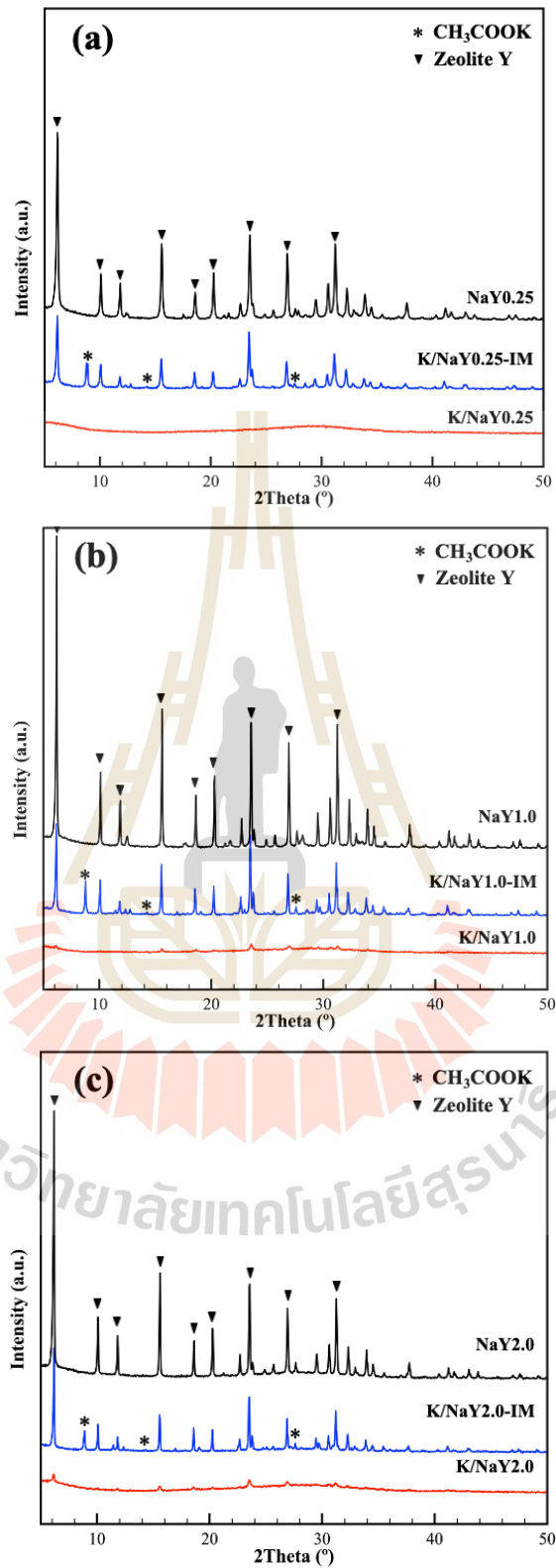


Figure 5.2 XRD patterns of impregnated (blue line) and calcined K/NaY (red line) compared with bare NaY (black line) on K/NaY0.25 (a), K/NaY1.0 (b), and K/NaY2.0 (c).

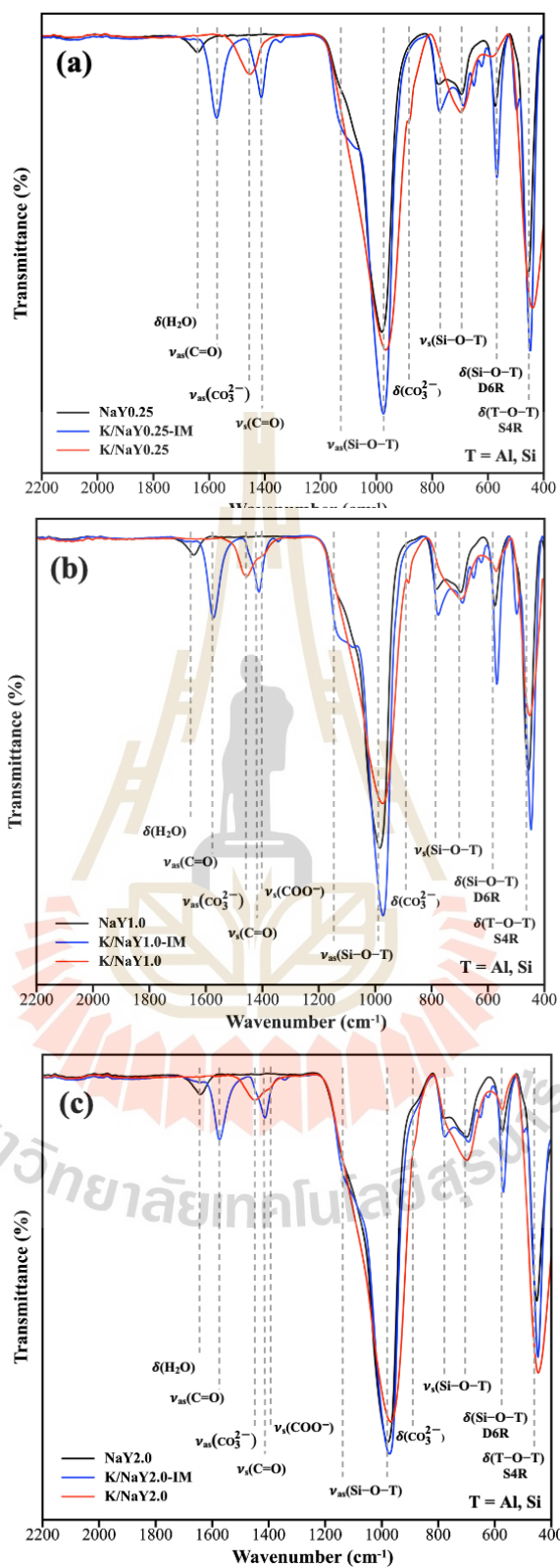
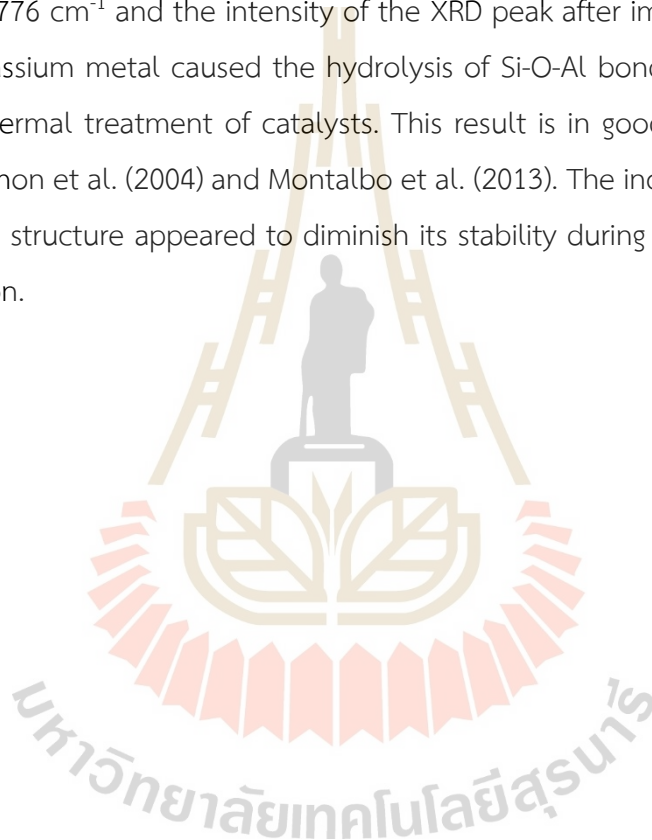


Figure 5.3 FTIR spectra of impregnated (blue line) and calcined K/NaY (red line) compared with bare NaY (black line) on K/NaY0.25 (a), K/NaY1.0 (b), and K/NaY2.0 (c).

The thermal stability of zeolite was monitored by investigation the samples heated for 3 h at 500 °C under the atmosphere as the same condition for catalyst preparation. The XRD pattern of parent and calcined NaY were displayed in **Figure 5.4**. The intensity of NaY peaks in the XRD pattern slightly decreased, suggesting that the calcination has no significant impact on the zeolite structure.

On the other hand, the potassium loading on zeolite NaY mainly affects the structure of zeolite. According to the above XRD and FTIR results, the decrease of the FTIR peak at 776  $\text{cm}^{-1}$  and the intensity of the XRD peak after impregnation suggested that the potassium metal caused the hydrolysis of Si-O-Al bonds of FAU frameworks during the thermal treatment of catalysts. This result is in good agreement with the studies by Simon et al. (2004) and Montalbo et al. (2013). The incorporation of alkaline ions into FAU structure appeared to diminish its stability during the impregnation and the calcination.



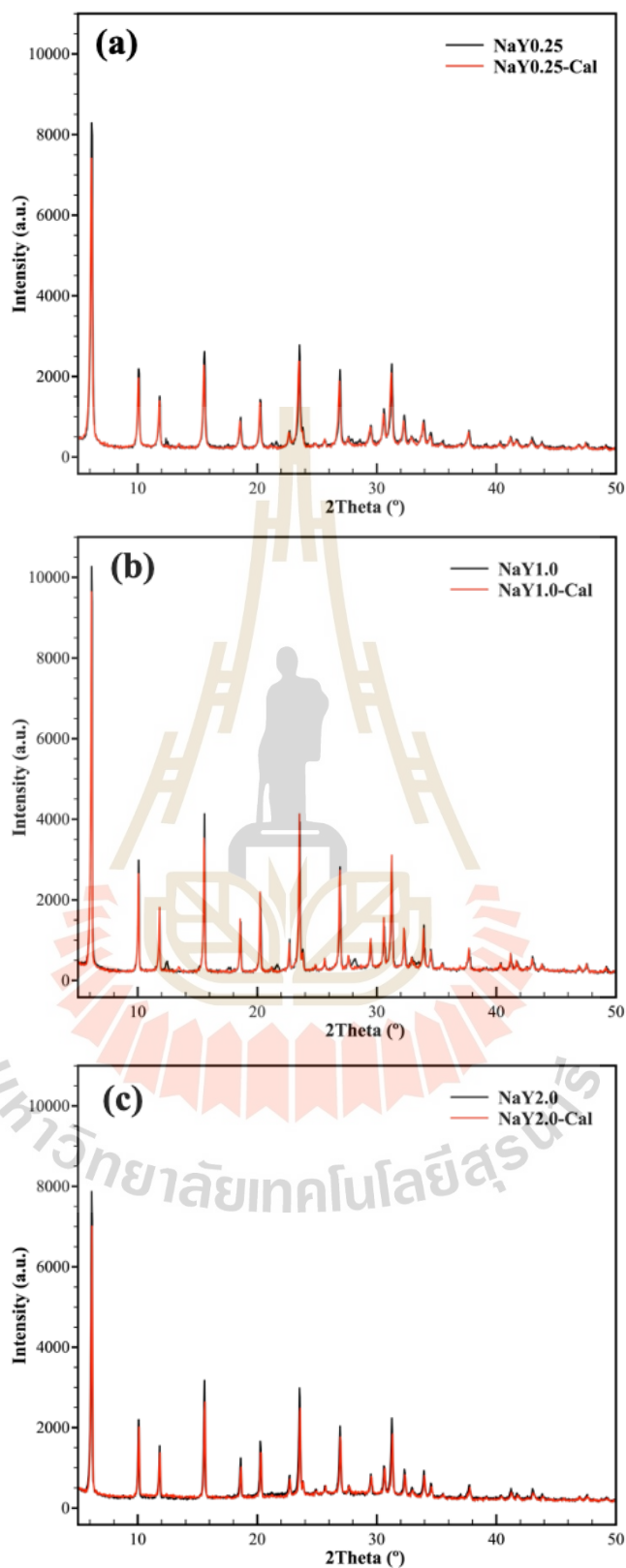


Figure 5.4 XRD patterns of bare zeolite (black line) compared with calcined zeolite NaY (red line) on K/NaY0.25 (a), K/NaY1.0 (b), and K/NaY2.0 (c).

**Table 5.1** FTIR peak assignments of functional group of zeolite and potassium species.

Wavenumber (cm <sup>-1</sup> )	Assignment	Reference
Functional groups for Zeolites		
452	T–O–T bending vibration of the four-membered ring (S4R)	Karge; Kosawatthanakun et al. (2019);
573	Si–O–T bending vibration of the double rings (D6R)	Mekki et al. (2019), Ma et al. (2021)
694, 776	Symmetric stretching of Si–O–T	
980	Asymmetric stretching of Si–O–T	
1120	Asymmetric stretching of Si–O–T (Shoulder)	
1640	O–H bending vibration (water adsorbed)	
Functional groups of acetate (CH <sub>3</sub> COOK)		
1412	Symmetric stretching of C=O	Zhong et al. (2018), Kosawatthanakun
1574	Asymmetric stretching of C=O	et al. (2019)
Functional groups of carbonate (K <sub>2</sub> CO <sub>3</sub> )		
885	In-plane bending of CO <sub>3</sub> <sup>2-</sup>	Du et al. (2010), Weilach et al. (2011),
1398	Symmetric stretching of COO <sup>-</sup> , Monodentate carbonate	Föttinger et al. (2017),
1450	Asymmetric stretching of CO <sub>3</sub> <sup>2-</sup> , Free carbonate	Kosawatthanakun et al. (2019)

Figure 5.5-5.7 displays the morphologies of all parent and calcined samples with different magnitudes. Bare zeolite NaY has polycrystalline formations with various morphologies. NaY0.25 consists of small particles approximately 150 to 250 nm in size as monitored in Figure 5.5a,b. Each particle constitutes a cluster of small crystals interconnected. Furthermore, NaY1.0 and NaY2.0 display a hexagonal structure with a uniform distribution of crystal sizes. There is crystal size approximately 1  $\mu\text{m}$  for NaY1.0 and 2  $\mu\text{m}$  for NaY2.0, respectively, as illustrated in Figure 5.6-5.7a,b. However, NaY2.0 exhibits a mixed phase of zeolite particles and amorphous material.

For the catalyst samples in Figure 5.5-5.7c,d, a distinct pattern covers the zeolite surface across all samples. These results suggest that the impregnation and calcination led to a greater degree of structural alteration. Notably, the presence of surface roughness and aggregation were observed, suggesting a significant impact on the surface characteristics according to XRD patterns. Moreover, K/NaY0.25 demonstrates the aggregation of zeolite crystals, as shown in Figure 5.5c,d.

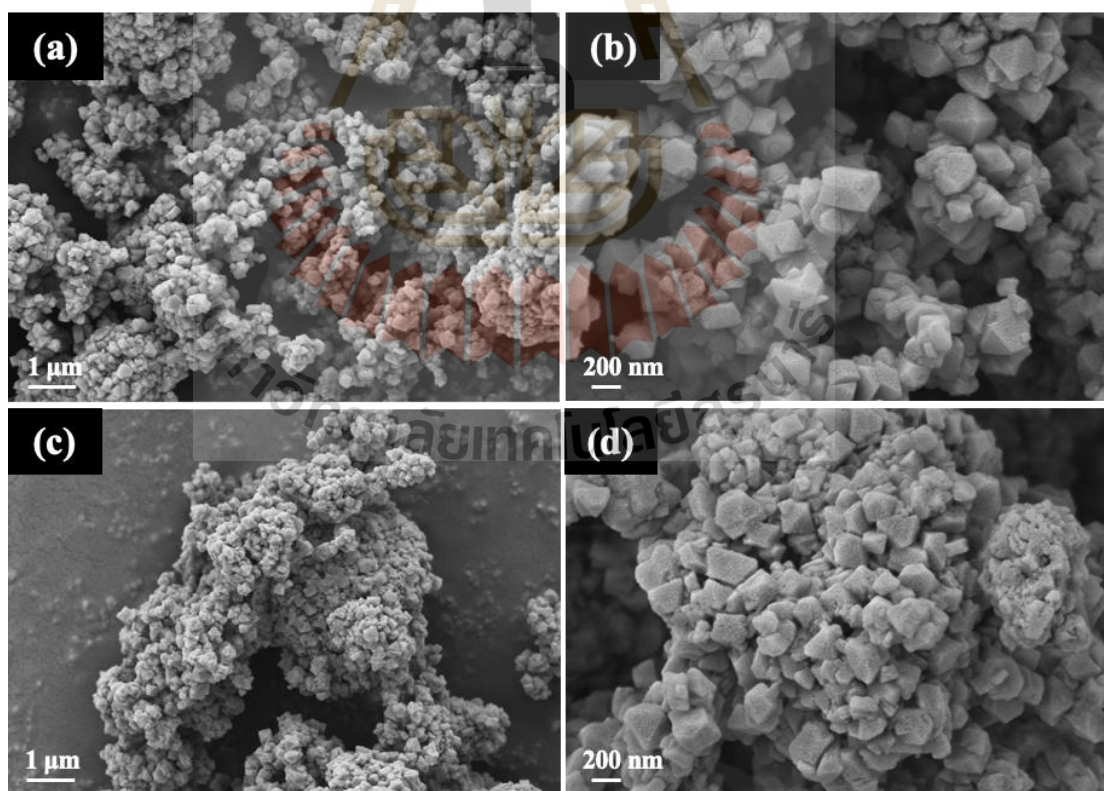


Figure 5.5 SEM images of NaY0.25 (a,b) and K/NaY0.25 (c,d) with different magnitudes including x10k and x30k.

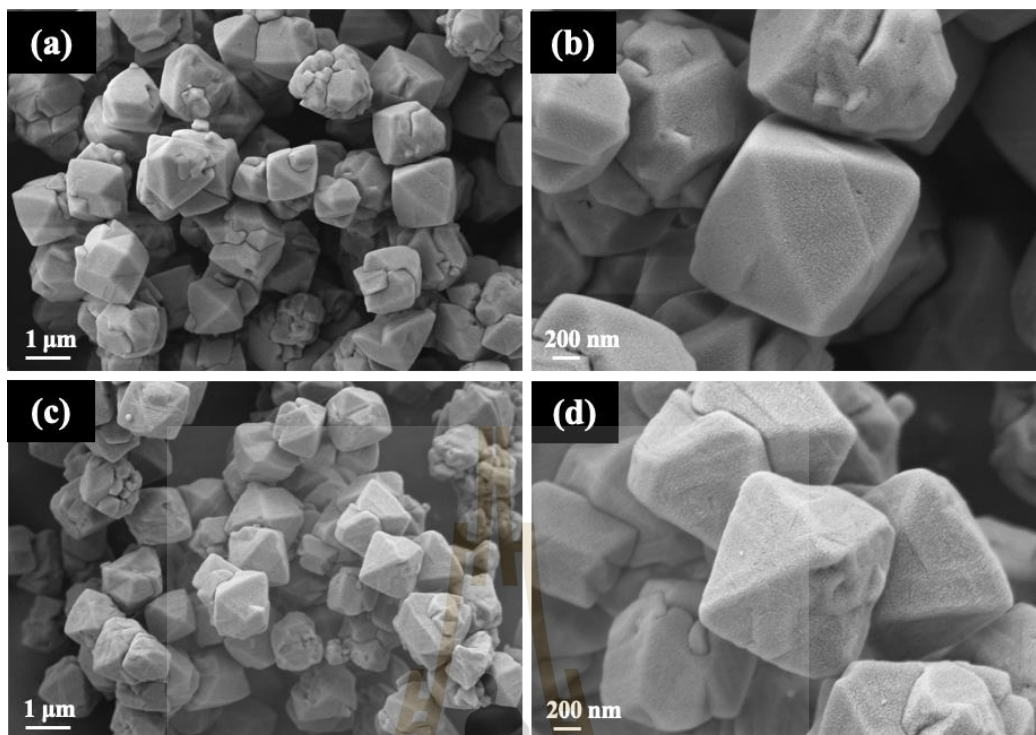


Figure 5.6 SEM images of NaY1.0 (a,b) and K/NaY1.0 (c,d) with different magnitudes including x10k and x30k.

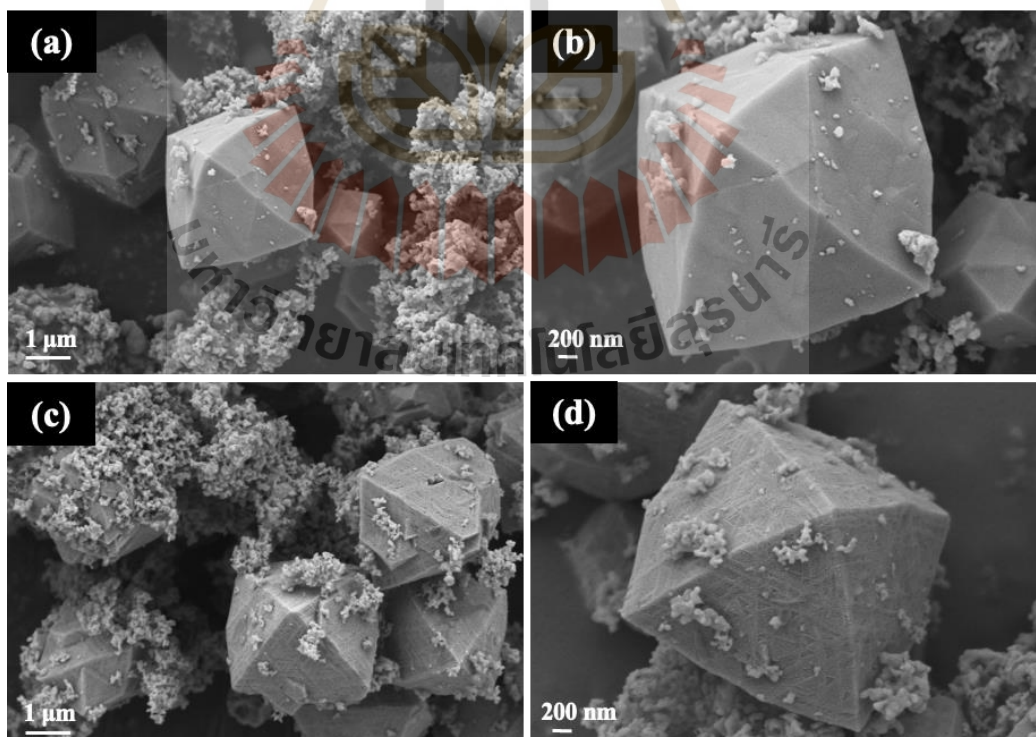


Figure 5.7 SEM images of NaY2.0 (a,b) and K/NaY2.0 (c,d) with different magnitudes including x10k and x30k.

**Figure 5.8** illustrates the nitrogen adsorption-desorption of all NaY samples, and **Table 5.2** shows their textural properties. All parent samples possessed a type I isotherm, implying a characteristic of microporous materials according to the IUPAC classification (Sing, 1985, Thommes et al., 2015). NaY0.25 with the smallest nanocrystal has a high surface area of 732 m<sup>2</sup>/g. Following, NaY1.0 and NaY2.0 are 696.2 and 374.6 m<sup>2</sup>/g, respectively. NaY2.0 has a lowest surface area because of the presence of amorphous phase. K/NaY0.25 exhibits a type IV isotherm with a hysteresis loop, indicating capillary condensation in the mesopores at high relative pressure. The aggregation of zeolite crystals leads to the formation of these mesopores. However, K/NaY1.0 and K/NaY2.0 indicated the type II isotherm that are nonporous solid. This decline in surface area is attributed to the aggregation of zeolite structure.

**Table 5.2** Textural properties of zeolite NaY and the catalyst samples.

Sample	Si/Al ratio	BET surface area (m <sup>2</sup> /g)	External surface area (m <sup>2</sup> /g)	Pore volume (cm <sup>3</sup> /g)
NaY0.25	2.0	732.0	8.1	0.36
K/NaY0.25		14.4	12.9	0.06
NaY1.0	2.2	696.2	22.6	0.33
K/NaY1.0		2.8	2.1	0.02
NaY2.0	2.2	374.6	15.0	0.19
K/NaY2.0		21.4	9.1	0.03

**Figure 5.9** shows HRTEM micrograph for the catalysts compared with the commercial zeolite NaY. The structure of zeolite NaY shows a pattern of dense-shallow distribution with the internal arrangement along the lattice planes. Conversely, the zeolite structure in both samples collapsed after catalyst preparation. This observation aligns with the findings from previous XRD patterns mentioned previously. Notably, the nano-sized sample reveals the presence of mesopore within the structure, consistent with the nitrogen isotherm analysis.

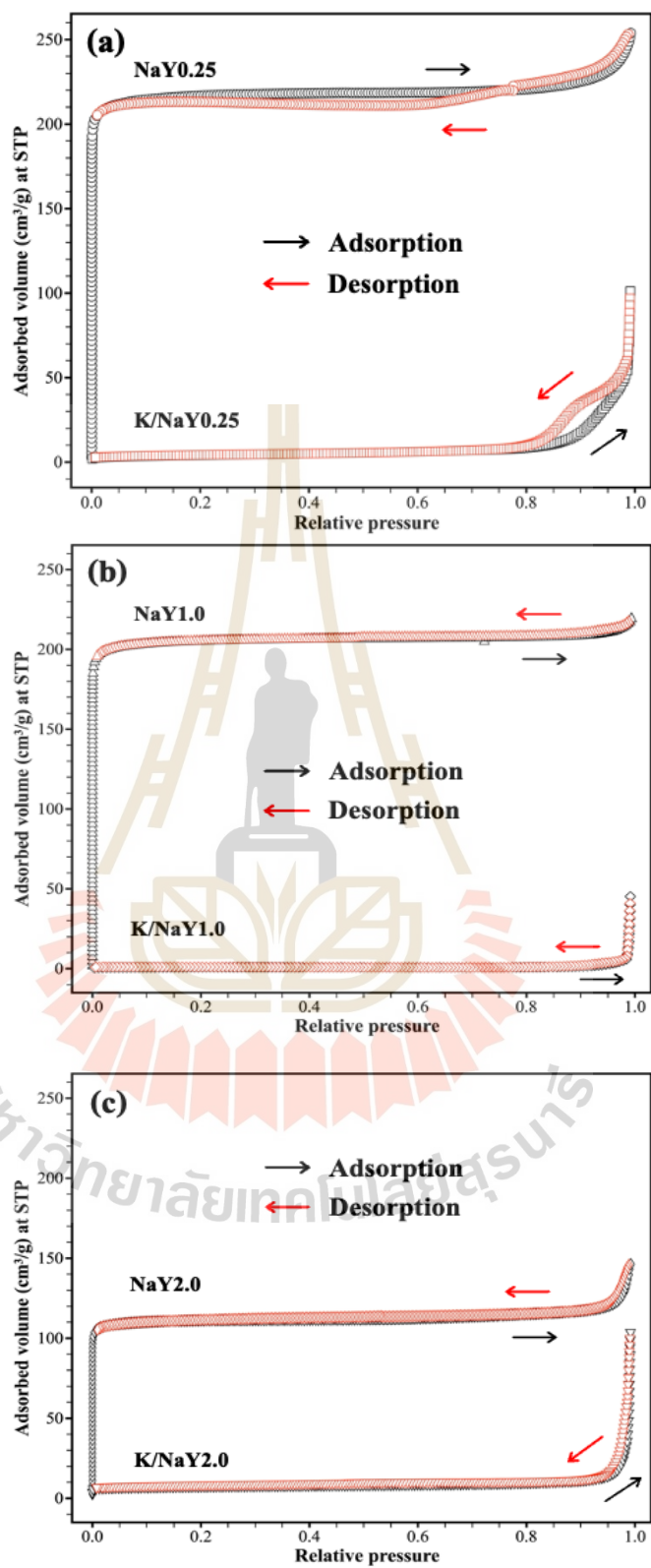


Figure 5.8 Nitrogen adsorption-desorption isotherm of zeolite NaY in various sizes and the catalyst samples.

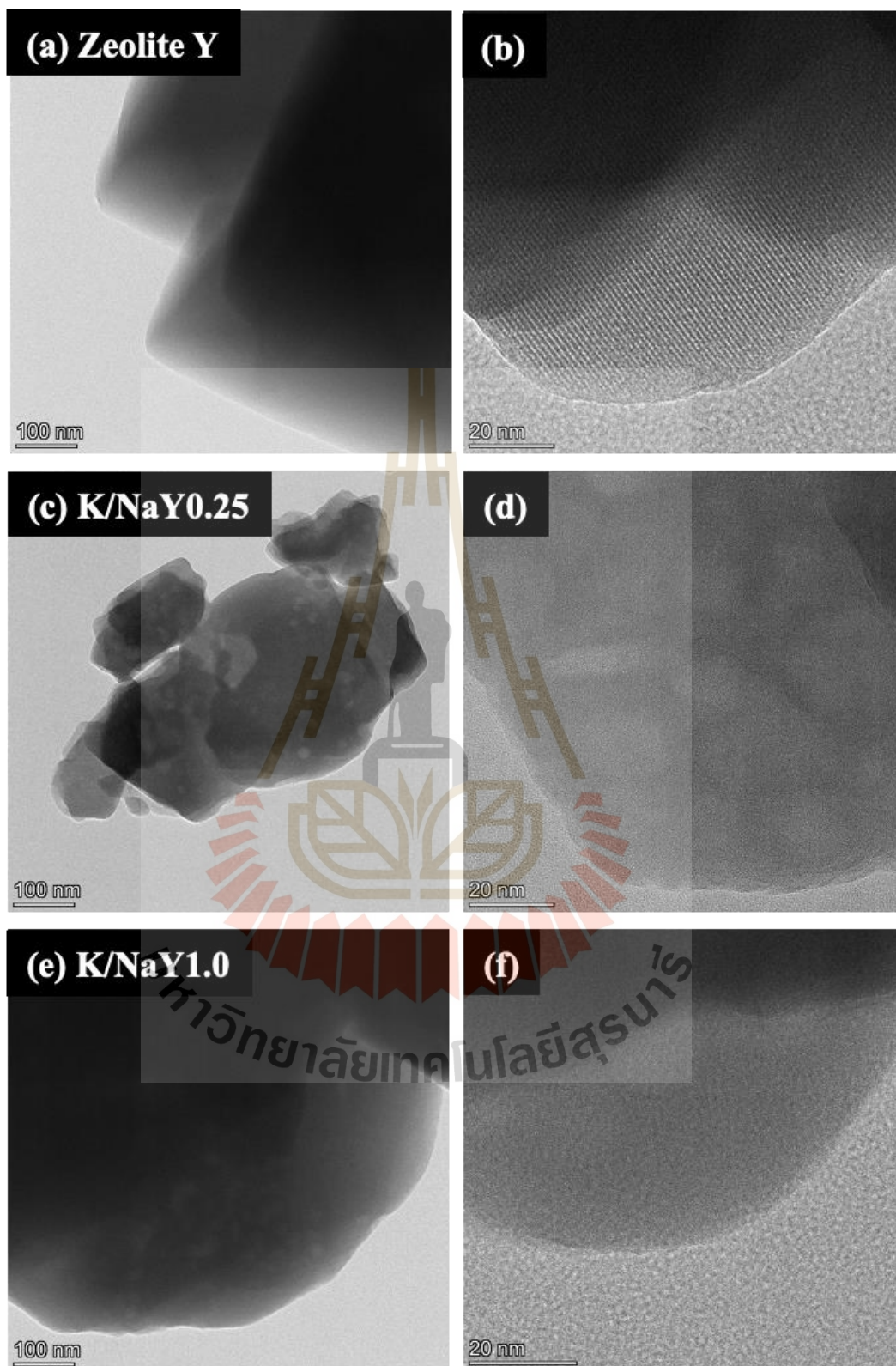


Figure 5.9 HRTEM images of commercial zeolite NaY (a,b), K/NaY0.25 (c,d) and K/NaY1.0 (e,f) in different magnification.

### 5.3.2 Catalytic performance on transesterification

**Figure 5.10** illustrates the biodiesel yield from the first run on K/NaY0.25, K/NaY1.0, and K/NaY2.0 catalysts. Meanwhile, **Figure 5.11** displays the chromatogram of samples in first and second runs. The yields were 98.6, 25.9, and 71.3%, respectively. On the other hands, the yield dropped significantly in the second run from all catalysts. Specifically, SP\_K/NaY1.0 and SP\_K/NaY2.0 did not produce any yield products, whereas SP\_K/NaY0.25 gave an 8.5% biodiesel. According to the aforementioned potassium species determination by FTIR results, monodentate carbonate provided nearly complete conversion of palm oil, along with a good yield towards biodiesel as a desired product. In addition, the presence of free carbonate promotes the biodiesel production.

**Table 5.3** compares the yield from this work with those from the literatures. The behavior of K/NaY0.25 from this study mirrors that in Kosawatthanakun et al. (2019). K/NaY has small particles and exhibits optimal performance in initial runs, but the yield drops in second run due to the leaching of active species. Therefore, the carbonate species play a significant role in this reaction.

Besides, the particle size of zeolite becomes the second factor for the reaction because of the relationship of surface area. In our case, higher external surface area showed the better performance as performed in K/NaY0.25 catalyst, following K/NaY2.0 and K/NaY1.0, respectively. Nevertheless, K/NaY2.0 has a mixed phase of zeolite and amorphous phase, resulting in better performance than K/NaY1.0. The zeolites generally suffer from limited base density and severe mass-transfer restriction for bulky FAME (Pang et al., 2020; Supamathanon et al., 2023). Additionally, Supamathanon and co-workers in 2021 reported that geopolymer (Geo) materials serve as effective supports for the transesterification of soybean oil. Geo is amorphous to semicrystalline, offering a distribution across multiple scales. This feature promotes the efficient diffusion of reactants through the active site. Similarly, the presence of an amorphous phase induces the distribution of reactant, resulting in high biodiesel yield. Thereby, the biodiesel production depends on two crucial factors: carbonate species and crystallinity.

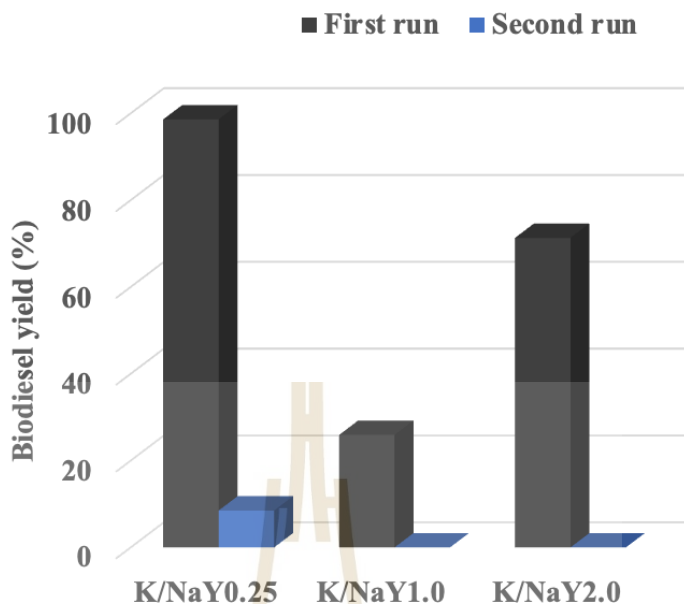


Figure 5.10 Biodiesel yield from first and second runs on K/NaY0.25, K/NaY1.0, and K/NaY2.0 at 60 °C for 3 h.

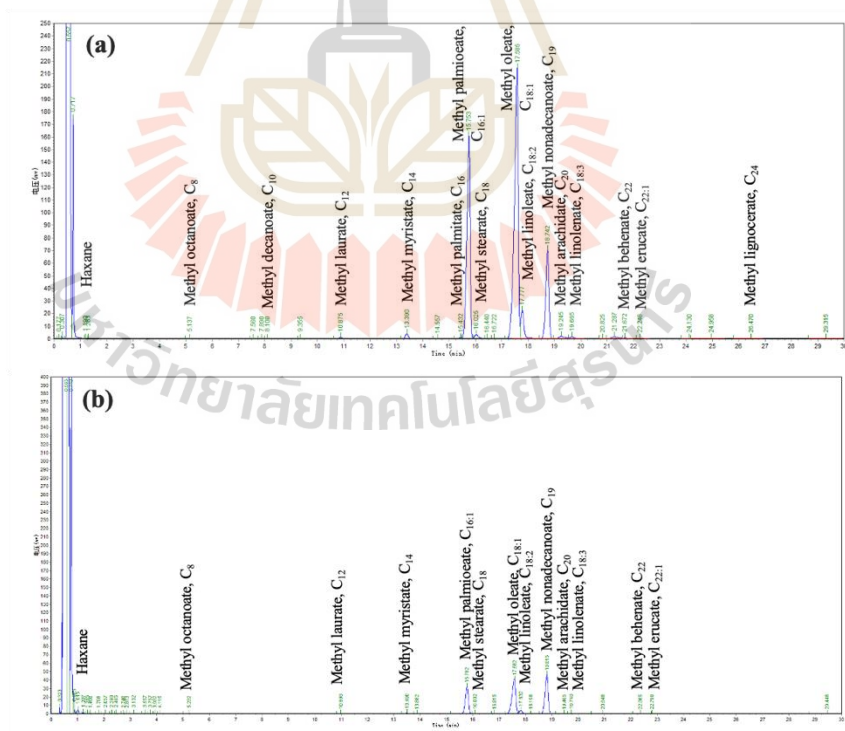


Figure 5.11 GC chromatograms of biodiesel products from transesterification of palm oil obtained from (a,b) K/NaY0.25 (1<sup>st</sup> and 2<sup>nd</sup> runs), (c,d) K/NaY1.0 (1<sup>st</sup> and 2<sup>nd</sup> runs), and (e,f) K/NaY2.0 (1<sup>st</sup> and 2<sup>nd</sup> runs).

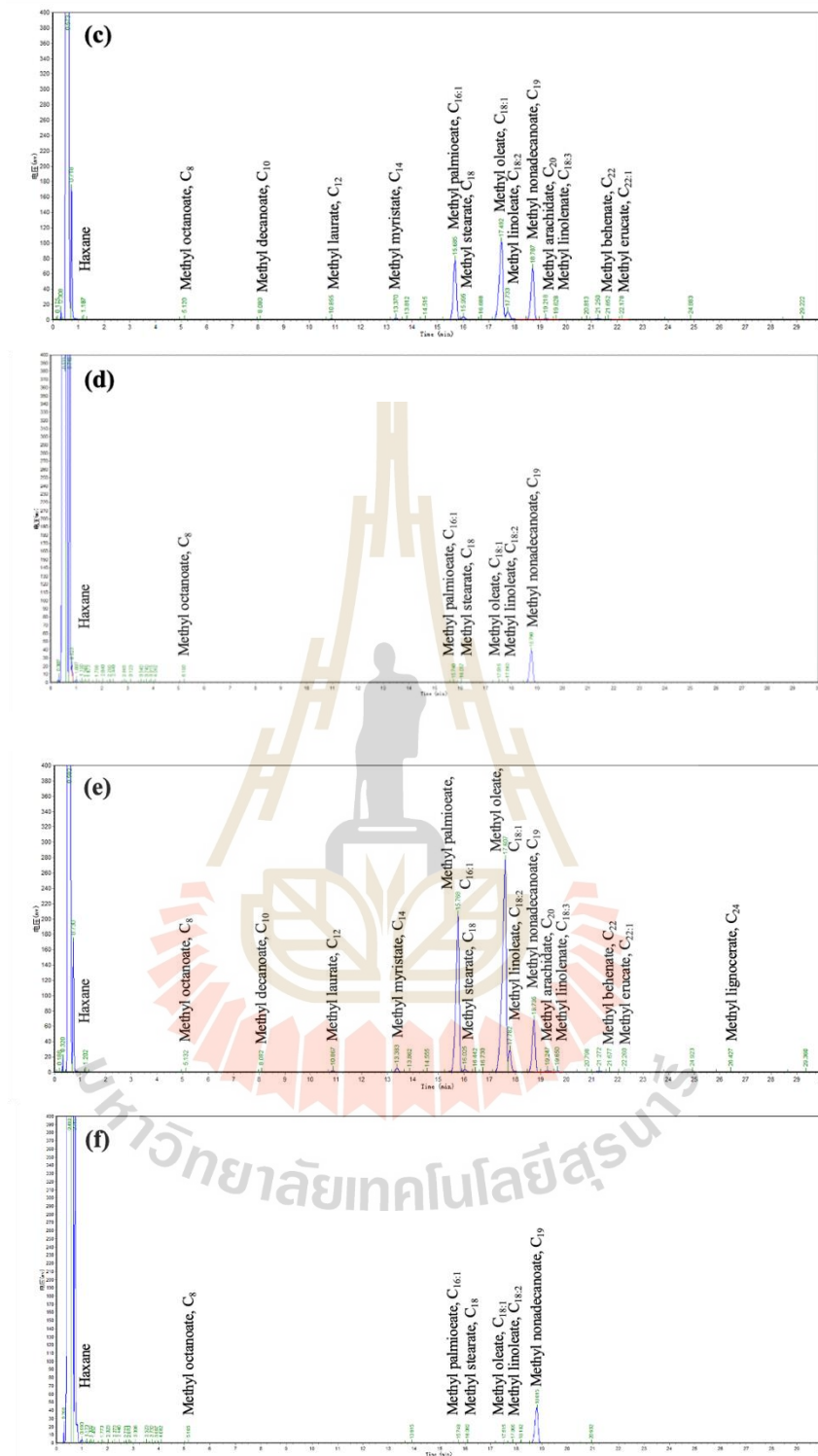


Figure 5.11 GC chromatograms of biodiesel products from transesterification of palm oil obtained from (a,b) K/NaY0.25 (1<sup>st</sup> and 2<sup>nd</sup> runs), (c,d) K/NaY1.0 (1<sup>st</sup> and 2<sup>nd</sup> runs), and (e,f) K/NaY2.0 (1<sup>st</sup> and 2<sup>nd</sup> runs) (Cont.).

**Table 5.3** Comparison of transesterification of vegetable oil for biodiesel production on zeolite catalysts from literature and this work.

Sample	Preparation method	Carbonate species	Crystal sizes	Reaction condition <sup>a</sup>	Biodiesel yield (%)		Reference
					1 <sup>st</sup> run	2 <sup>nd</sup> run	
12K/NaY	IM	N/A	0.6-0.8 μm	Jatropha seed oil at 65 °C for 3 h	73	N/A	Supamathanon et al. (2011)
12K/NaY	IM	Free carbonate and monodentate	< 1 μm	Palm oil at 60 °C for 3 h	72	N/A	Rakmae et al. (2016)
12K/NaY	IM	Free carbonate and monodentate	500 nm	Palm oil at 60 °C for 3 h	94	3	Kosawatthanakun et al. (2019)
12K/NaY <sup>b</sup>	IM-MA	Monodentate	< 1 μm	Jatropha seed oil at 60 °C for 3 h	97	96	Maneechot et al. (2021)
12K/NaY <sup>b</sup>	IM	Monodentate	< 1 μm	at 60 °C for 3 h	91	85	
12K/NaY	IM	Free carbonate and monodentate	150-250 nm	Palm oil at 60 °C for 3 h	99	9	This work
	IM	Monodentate	1 μm		26	0	
	IM	Monodentate	2 μm		71	0	

Note: N/A abbreviation is not available.; CH<sub>3</sub>COOH/CH<sub>3</sub>COOK buffer is a precursor.; IM = ultrasonic-assisted impregnation; MA = microwave-assisted impregnation.

<sup>a</sup> = 0.2 g catalyst, 5.0 g oil, 2.9 g MeOH

<sup>b</sup> = hierarchical NaY

### 5.3.3 Stability of catalysts

**Figure 5.12** exhibits the FTIR spectra of fresh and spent catalysts after transesterification. SP2 means obtained catalysts after second cycle. The FTIR spectra of both micron-sized samples are not different from their fresh samples. The monodentate carbonate peaks were still observed and were not changed. This situation likely resulted from the physicochemical deposition of some coke on surface-active site, leading to deactivation. Meanwhile, the free carbonate species peak of nano-sized sample has a lower intensity. The decrease in those peaks indicate this carbonate leaching after reaction, which mean free carbonate act as a homogeneous catalyst. It agrees with the transesterification performance as shown in **Figure 5.10** above. Nevertheless, the morphology of spent samples remains unchanged after testing as illustrated in **Figure 5.13**.

**Table 5.4** shows the EDS element analysis of fresh and spent catalysts. This data indicates that potassium is well-dispersed in all samples. Furthermore, the amount of potassium before and after the catalysis did not exhibit a significant change. Namely, all samples deactivate after testing the transesterification. The cause are the deactivated active site and carbonate leaching.

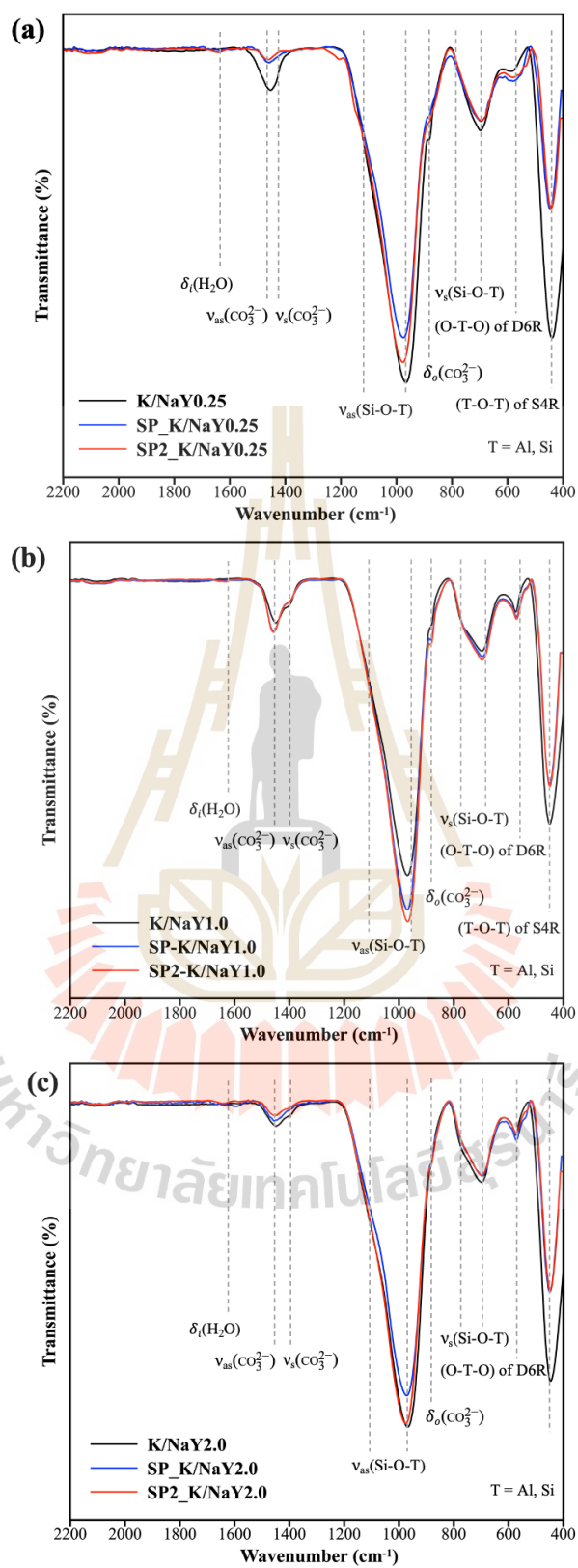


Figure 5.12 Comparison of fresh and spent catalysts by FTIR spectra of K/NaY0.25 (a), K/NaY1.0 (b), and K/NaY2.0 (c).

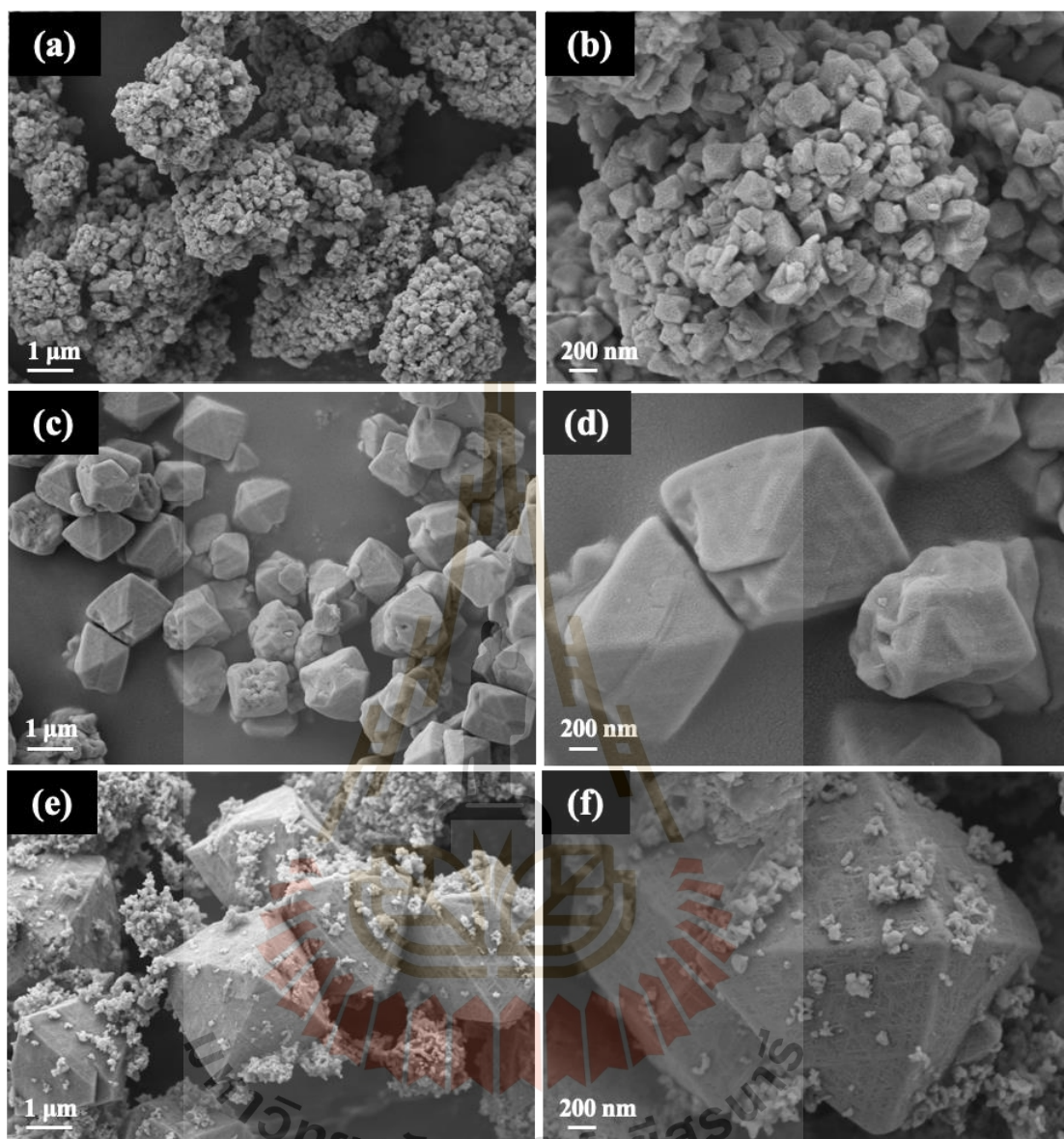


Figure 5.13 SEM images of spent  $K/NaY_{0.25}$  (a,b),  $K/NaY_{1.0}$  (c,d), and  $K/NaY_{2.0}$  (e,f).

Table 5.4 EDS element composition of fresh and spent catalysts.

Sample	Element composition (wt.%)				
	Si	Al	O	Na	K
K/NaY0.25	14.2 ± 0.4	7.0 ± 0.1	66.9 ± 0.8	6.0 ± 0.8	11.7 ± 1.0
SP_K/NaY0.25	14.9 ± 0.1	7.4 ± 0.0	67.3 ± 0.3	4.7 ± 0.0	11.1 ± 0.3
K/NaY1.0	16.1 ± 0.9	7.4 ± 0.3	62.6 ± 2.0	7.0 ± 0.3	13.1 ± 1.2
SP_K/NaY1.0	14.3 ± 0.4	6.7 ± 0.1	66.6 ± 1.1	6.5 ± 0.2	11.5 ± 0.6
K/NaY2.0	15.2 ± 0.7	6.8 ± 0.3	66.9 ± 1.2	6.3 ± 0.2	9.2 ± 0.2
SP_K/NaY2.0	15.8 ± 0.5	6.9 ± 0.1	67.0 ± 0.6	5.9 ± 0.4	8.7 ± 1.4

### 5.3.4 Catalytic behavior (Active site leaching)

Figure 5.14 illustrated the catalytic performance of K/NaY0.25, K/NaY1.0, and K/NaY2.0 in the leaching test. The products obtained from the initial run include palm oil, biodiesel, and glycerol. Malins (2018) have demonstrated that the potassium carbonate exhibited slightly solubility in methanol, while significantly dissolves in glycerol. Hence, the combination of glycerol and carbonate has the potential to form a homogeneous catalyst in this context. However, the presence of glycerol resulted in a delay in the transesterification process. This delay is attributed to glycerol being a side product that reduces the reaction rate, in accordance with (Nyepetsi et al., 2021), as outlined by Le Chatelier's principle. Consequently, biodiesel production is hindered.

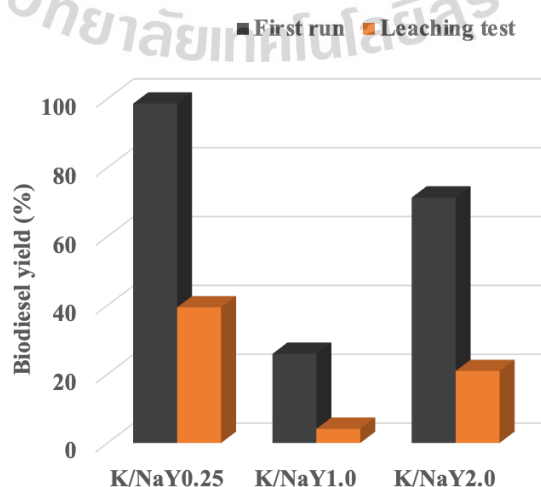


Figure 5.14 Biodiesel yield of transesterification in first run and leaching test.

## 5.4 Conclusions

The 12 wt.% of potassium acetate buffer was loaded onto zeolite NaY with various crystal sizes and phases using ultrasonic-assisted impregnation method. Subsequently, potassium acetate underwent decomposition and conversion to potassium carbonate through calcination at 500 °C for 3 h. Remarkably, the zeolite structure collapsed after potassium loading and calcination. Moreover, it was observed that the different carbonate species supported various NaY crystal sizes. Specifically, K/NaY0.25 displayed both free carbonate and monodentate carbonate, whereas only monodentate carbonate was present on micron-sized catalysts.

In the transesterification of palm oil and methanol during the first run, nano-sized zeolite exhibited high biodiesel yield, while both micron-sized zeolite provided medium to low biodiesel yield. The yield decreased by 10 times for K/NaY0.25 in the second run, whereas K/NaY1.0 and K/NaY2.0 were deactivated. The poor performance of the catalysts was attributed to the leaching of free carbonate, the high microporous structure, and the coke formation on the active site. Therefore, the carbonate species and crystallinity of the zeolite significantly impact to the transesterification of palm oil to biodiesel.

## 5.5 References

- Afzal, M., Ahmad, H., and Mahmood, F. (1991). Decomposition kinetics of metal acetates. *J. Chem. Soc. Pak.*, 13, 219-222.
- Baerlocher, C. (2008). Database of zeolite structures. <http://www.iza-structure.org/databases/> (accessed on 26 June 2023).
- Changmai, B., Vanlalveni, C., Ingle, A. P., Bhagat, R., and Rokhum, S. L. (2020). Widely used catalysts in biodiesel production: a review. *RSC Adv.*, 10(68), 41625-41679.
- Du, H., Williams, C. T., Ebner, A. D., and Ritter, J. A. (2010). In situ FTIR spectroscopic analysis of carbonate transformations during adsorption and desorption of CO<sub>2</sub> in K-promoted HTlc. *Chem. Mater.*, 22(11), 3519-3526.

- Föttinger, K., Emhofer, W., Lennon, D., and Rupprechter, G. (2017). Adsorption and reaction of CO on (Pd-)Al<sub>2</sub>O<sub>3</sub> and (Pd-)ZrO<sub>2</sub>: vibrational spectroscopy of carbonate Formation. *Top. Catal.*, 60(19), 1722-1734.
- Huang, Y., Wang, K., Dong, D., Li, D., Hill, M. R., Hill, A. J., and Wang, H. (2010). Synthesis of hierarchical porous zeolite NaY particles with controllable particle sizes. *Microporous Mesoporous Mater.*, 127(3), 167-175.
- Isa, M. A., Chew, T. L., and Yeong, Y. F. (2018). *Zeolite NaY synthesis by using sodium silicate and colloidal silica as silica source*. IOP Conf. Ser. Mater. Sci. Eng.
- Karge, H. G. (2001). Characterization by IR spectroscopy. In *Verified syntheses of zeolitic materials*. Elsevier Sci., 69-71.
- Keawkumay, C., Rongchapo, W., Sosa, N., Suthirakun, S., Koleva, I. Z., Aleksandrov, H. A., Vayssilov, G. N., and Wittayakun, J. (2019). Paraquat adsorption on NaY zeolite at various Si/Al ratios: A combined experimental and computational study. *Mater. Chem. Phys.*, 238, 121284.
- Kosawatthanakun, S., Pansakdanon, C., Sosa, N., Chanlek, N., Roessner, F., Prayoonpokarach, S., and Wittayakun, J. (2022). Comparative properties of K/NaX and K/NaY from ultrasound-assisted impregnation and performance in transesterification of palm oil. *ACS Omega*, 7(11), 9130-9141.
- Ma, Y.-K., Rigolet, S., Michelin, L., Paillaud, J.-L., Mintova, S., Khoerunnisa, F., Daou, T. J., and Ng, E.-P. (2021). Facile and fast determination of Si/Al ratio of zeolites using FTIR spectroscopy technique. *Micropor. Mesopor. Mat.*, 311, 110683.
- Malins, K. (2018). The potential of K<sub>3</sub>PO<sub>4</sub>, K<sub>2</sub>CO<sub>3</sub>, Na<sub>3</sub>PO<sub>4</sub> and Na<sub>2</sub>CO<sub>3</sub> as reusable alkaline catalysts for practical application in biodiesel production. *Fuel Process. Technol.*, 179, 302-312.
- Manadee, S., Sophiphun, O., Osakoo, N., Supamathanon, N., Kidkhunthod, P., Chanlek, N., Wittayakun, J., and Prayoonpokarach, S. (2017). Identification of potassium phase in catalysts supported on zeolite NaX and performance in transesterification of Jatropha seed oil. *Fuel Process. Technol.*, 156, 62-67.
- Maneechot, P., Sriprapakhan, P., Manadee, S., and Artkla, R. (2021). Improvement of potassium species dispersed on hierarchical zeolite NaY by using combined methods between ultrasound and microwave-assisted impregnation as

- catalysts for transesterification of refined *Jatropha* seed oil. *Biomass Bioenergy*, *153*, 106202.
- Mekki, A., Benmaati, A., Mokhtar, A., Hachemaoui, M., Zaoui, F., Habib Zahmani, H., Sassi, M., Hacini, S., and Boukoussa, B. (2019). Michael Addition of 1,3-Dicarbonyl Derivatives in the Presence of Zeolite Y as an Heterogeneous Catalyst. *J. Inorg Organomet Polym Mater.*, *30*(7), 2323-2334.
- Mintova, S. (2016). Verified synthesis of zeolitic materials. *The Synthesis Commission of the International Zeolite Association*, 215-223.
- Mintova, S., Grand, J., and Valtchev, V. (2016). Nanosized zeolites: quo vadis? *Comptes Rendus. Chimie*, *19*(1-2), 183-191.
- Montalbo, K. D., Leon, R. L. d., Sophiphun, O., Manadee, S., Prayoonpokarach, S., and Wittayakun, J. (2013). Characterization and catalytic performance of potassium loaded on rice husk silica and zeolite nay for transesterification of *jatropha* seed oil. *Química Nova*, *36*, 1116-1120.
- Nyepetsi, M., Mbaiwa, F., Oyetunji, O. A., Dzade, N. Y., and de Leeuw, N. H. (2021). The carbonate-catalyzed transesterification of sunflower oil for biodiesel production: in situ monitoring and density functional theory calculations. *S. Afr. J. Chem.*, *74*, 42-49.
- Pang, H., Yang, G., Li, L., and Yu, J. (2020). Efficient transesterification over two-dimensional zeolites for sustainable biodiesel production. *Green Energy Environ.*, *5*(4), 405-413.
- Rakmae, S., Keawkumay, C., Osakoo, N., Montalbo, K. D., de Leon, R. L., Kidkhunthod, P., Chanlek, N., Roessner, F., Prayoonpokarach, S., and Wittayakun, J. (2016). Realization of active species in potassium catalysts on zeolite NaY prepared by ultrasound-assisted impregnation with acetate buffer and improved performance in transesterification of palm oil. *Fuel*, *184*, 512-517.
- Shirazian, S., Ghafarnejad Parto, S., and Ashrafizadeh, S. N. (2014). Effect of water content of synthetic hydrogel on dehydration performance of nanoporous LTA zeolite membranes. *Int. J. Appl. Ceram.*, *11*(5), 793-803.

- Simon, A., Köhler, J., Keller, P., Weitkamp, J., Buchholz, A., and Hunger, M. (2004). Phase transformation of zeolites Cs, Na-Y and Cs, Na-X impregnated with cesium hydroxide. *Micropor. Mesopor. Mater.*, 68(1-3), 143-150.
- Sing, K. S. (1985). Reporting physisorption data for gas/solid systems with special reference to the determination of surface area and porosity (Recommendations 1984). *Pure appl. Chem.*, 57(4), 603-619.
- Supamathanon, N., Boonserm, K., Osakoo, N., Wittayakun, J., Prayoonpokarach, S., Chanlek, N., and Dungkaew, W. (2023). Potassium supported on zeolite-geopolymer hybrid materials as a new solid base catalyst for transesterification of soybean oil. *Renew. Energ.*, 202, 1460-1469.
- Supamathanon, N., Wittayakun, J., and Prayoonpokarach, S. (2011). Properties of Jatropha seed oil from Northeastern Thailand and its transesterification catalyzed by potassium supported on NaY zeolite. *J. Ind. Eng. Chem.*, 17(2), 182-185.
- Thommes, M., Kaneko, K., Neimark, A. V., Olivier, J. P., Rodriguez-Reinoso, F., Rouquerol, J., and Sing, K. S. W. (2015). Physisorption of gases, with special reference to the evaluation of surface area and pore size distribution (IUPAC Technical Report). *Pure Appl. Chem.*, 87(9-10), 1051-1069.
- Weilach, C., Spiel, C., Föttinger, K., and Rupprechter, G. (2011). Carbonate formation on Al<sub>2</sub>O<sub>3</sub> thin film model catalyst supports. *Surf. Sci.*, 605(15-16), 1503-1509.
- Zhang, T., Li, B., Li, H., Liu, Y., Li, J., Zhao, B., Zhang, X., and Wang, J. (2022). The efficient and green synthesis of biodiesel from crude oil without degumming catalyzed by sodium carbonate supported MoS<sub>2</sub>. *RSC Adv.*, 12(38), 24456-24464.
- Zhong, X.-H., Liu, Y., Xu, T., and Liu, W.-Y. (2018). Influencing factors of intercalation of potassium acetate into dickite using immersion method. *J. Alloys Compd.*, 742, 996-1001.

## CHAPTER VI

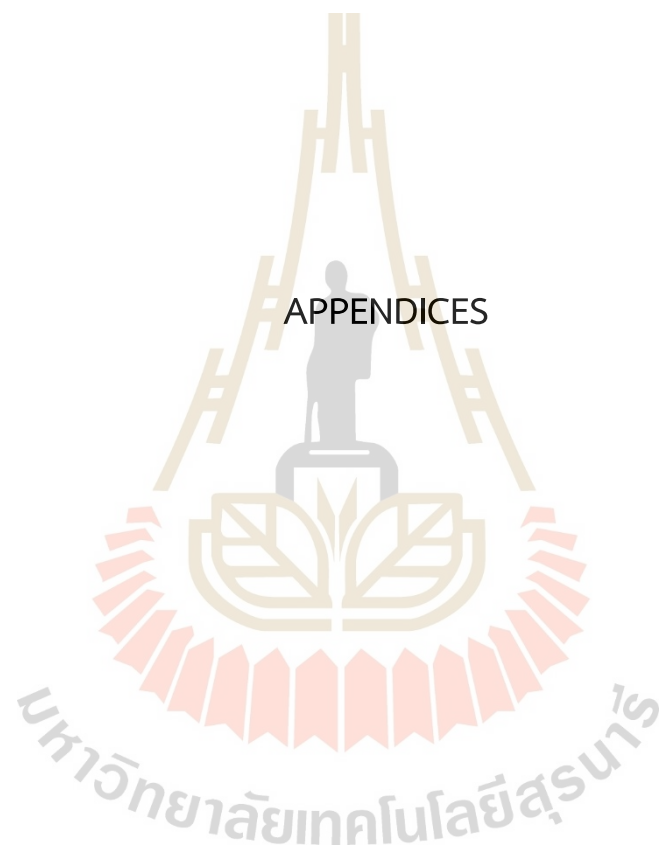
### CONCLUSIONS

Zeolite NaY crystal with an amorphous phase was obtained through a process mediated by trunk grass from Y-NT and Y-RT. This phenomenon suggests the unsuccessful intergrowth of zeolite. A high potassium content was observed in trunk grass, which inhibited the formation of zeolite particle. As a result, the blade grass is expected to be promoted instead of trunk grass for more successful zeolite NaY production.

Y-RB gave mixed phases of crystal and amorphous structure. The self-assembly of these NaY crystals was notably observed, especially in hemicellulose and cellulose. However, both components were eliminated upon acid treatment, leading to high proportion of lignin. The complex structure of lignin hindered the zeolite crystallization process. In contrast, Y-NB demonstrated successful synthesis. It has low Si/Al ratio and good dispersion compared with Y-WG. This result presents a higher paraquat adsorption capacity. Regarding the effect of grass content, it was found that 1.0 g of blade grass was optimal amount for the zeolite NaY synthesis.

For the transesterification of palm oil, the effect of water contents during zeolite synthesis were investigated. Three variants, namely NaY0.25, NaY1.0 and NaY2.0, were obtained using hydrothermal method with a crystallization time of 24 h. Subsequently, potassium catalysts supported on all NaY support were prepared using ultrasound-assisted impregnation. Potassium acetate was converted to carbonate by calcination, which caused the zeolite structure collapsed. Notably, nano-sized and micro-sized exhibited differences in carbonate species. In particular, the presence of free carbonate on K/NaY0.25 exhibited the best performance in biodiesel production compared to K/NaY1.0 and K/NaY2.0. Nevertheless, the second run, the biodiesel yield dropped, suggesting the leaching of active site.

APPENDICES



APPENDIX A  
PARAQUAT ADSORPTION

A.1 Calibration curve of paraquat solution for UV-Vis determination

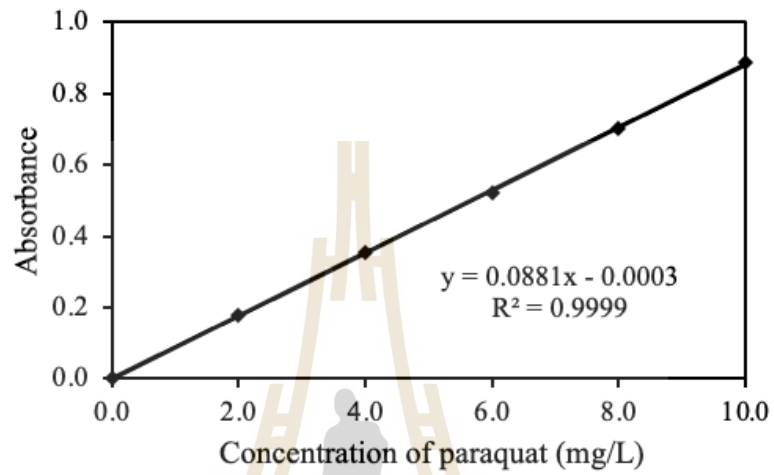


Figure A1 Calibration curve of paraquat solution for UV-Vis determination.

**Table A1** The equilibrium concentration ( $C_e$ ), equilibrium capacity of paraquat adsorption ( $q_e$ ), and  $C_e/q_e$  value of zeolite NaY samples at concentration 100 to 1000 mg/L.

Concentrations of paraquat solution		Sample name/Experiment								
		Y-WG			Y-NB			Y-RB		
		1st	2nd	3rd	1st	2nd	3rd	1st	2nd	3rd
100 ppm	$C_e$	1.33	1.29	1.24	1.33	1.38	1.35	1.89	2.06	1.92
	$q_e$	38.76	38.04	38.50	38.02	38.75	38.84	36.88	37.96	38.01
	$C_e/q_e$	0.035	0.034	0.032	0.035	0.036	0.035	0.051	0.054	0.051
250 ppm	$C_e$	7.74	7.71	6.57	8.89	6.55	7.81	69.87	69.24	68.14
	$q_e$	94.08	95.77	93.09	94.92	95.85	93.87	96.74	96.37	96.76
	$C_e/q_e$	0.082	0.081	0.071	0.094	0.068	0.083	0.014	0.014	0.014
500 ppm	$C_e$	131.58	142.27	131.18	158.79	103.74	157.92	304.21	307.91	307.85
	$q_e$	143.63	139.23	144.35	132.25	155.09	132.59	77.39	74.60	74.05
	$C_e/q_e$	0.916	1.021	0.909	1.201	0.669	1.191	3.931	4.128	4.158
750 ppm	$C_e$	369.84	365.59	355.51	352.77	352.95	383.28	549.14	567.59	571.72
	$q_e$	150.26	152.24	152.61	156.70	153.30	144.95	146.46	149.73	150.31
	$C_e/q_e$	2.461	2.401	2.329	2.251	2.302	2.644	6.971	8.106	8.209
1000 ppm	$C_e$	624.34	609.21	617.46	530.57	531.94	529.65	758.13	805.94	798.14
	$q_e$	146.46	149.73	150.31	181.60	185.00	186.65	93.75	75.81	79.63
	$C_e/q_e$	4.263	4.069	4.108	2.921	2.875	2.838	8.087	10.632	10.023

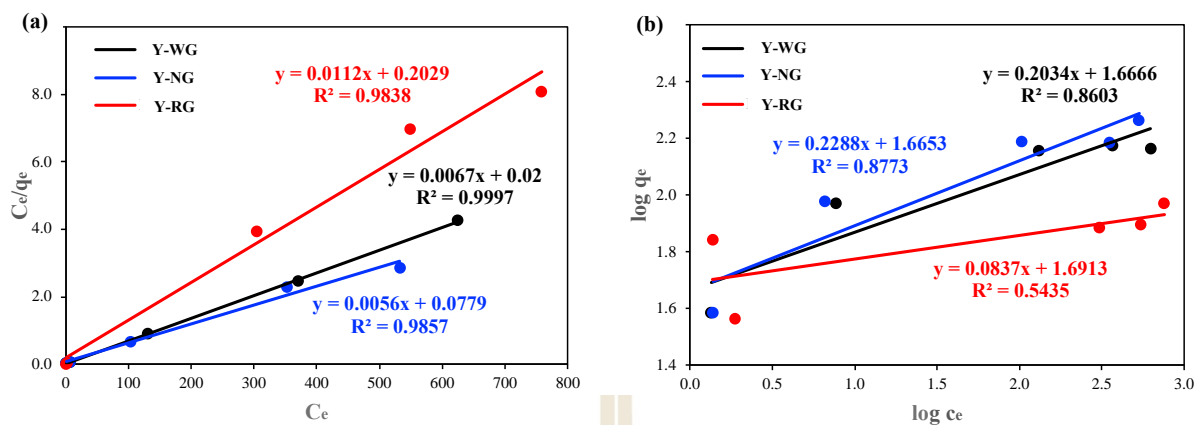


Figure A2 Plot of Langmuir (a) and Freundlich adsorption isotherm (b).

Table A2 Paraquat adsorption of zeolite NaY samples.

Sample	Maximum adsorption capacity of paraquat, $q_m$ (mg/g)			
	1st trial	2nd trial	3rd trial	Means
Y-WG	149.25	151.52	151.52	$150.76 \pm 1.30$
Y-NB	178.57	178.57	175.44	$177.53 \pm 1.81$
Y-RB	89.29	74.07	76.92	$80.09 \pm 8.09$

## APPENDIX B

## TRANSESTERIFICATION OF PALM OIL

## B.1 GC Chromatograms of biodiesel products from the conversion of palm oil

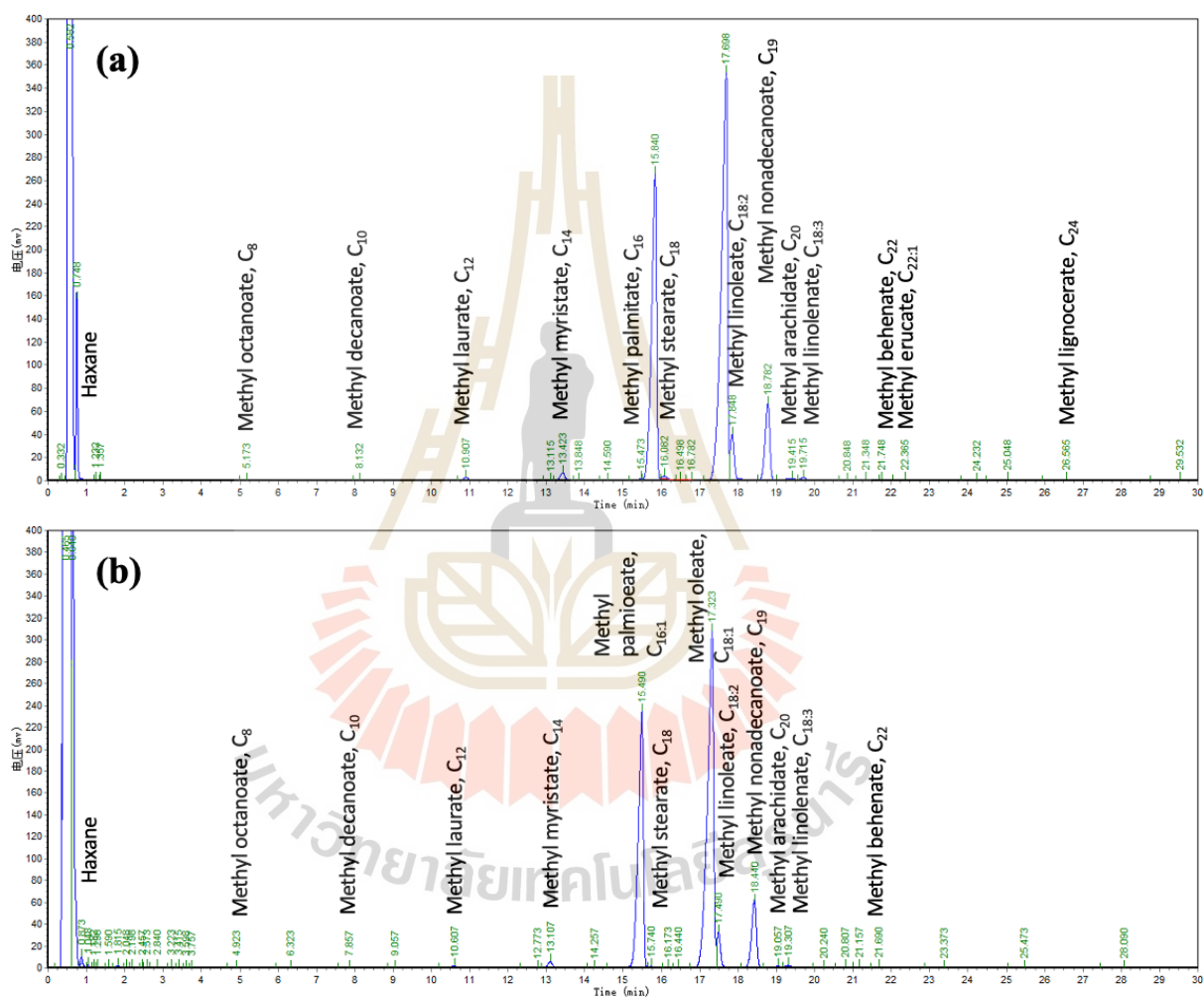


Figure B1 GC chromatogram of biodiesel products from transesterification of palm oil from K/NaY0.25 (a) duplicate of 1<sup>st</sup> run and (b) triplicate of 1<sup>st</sup> run.

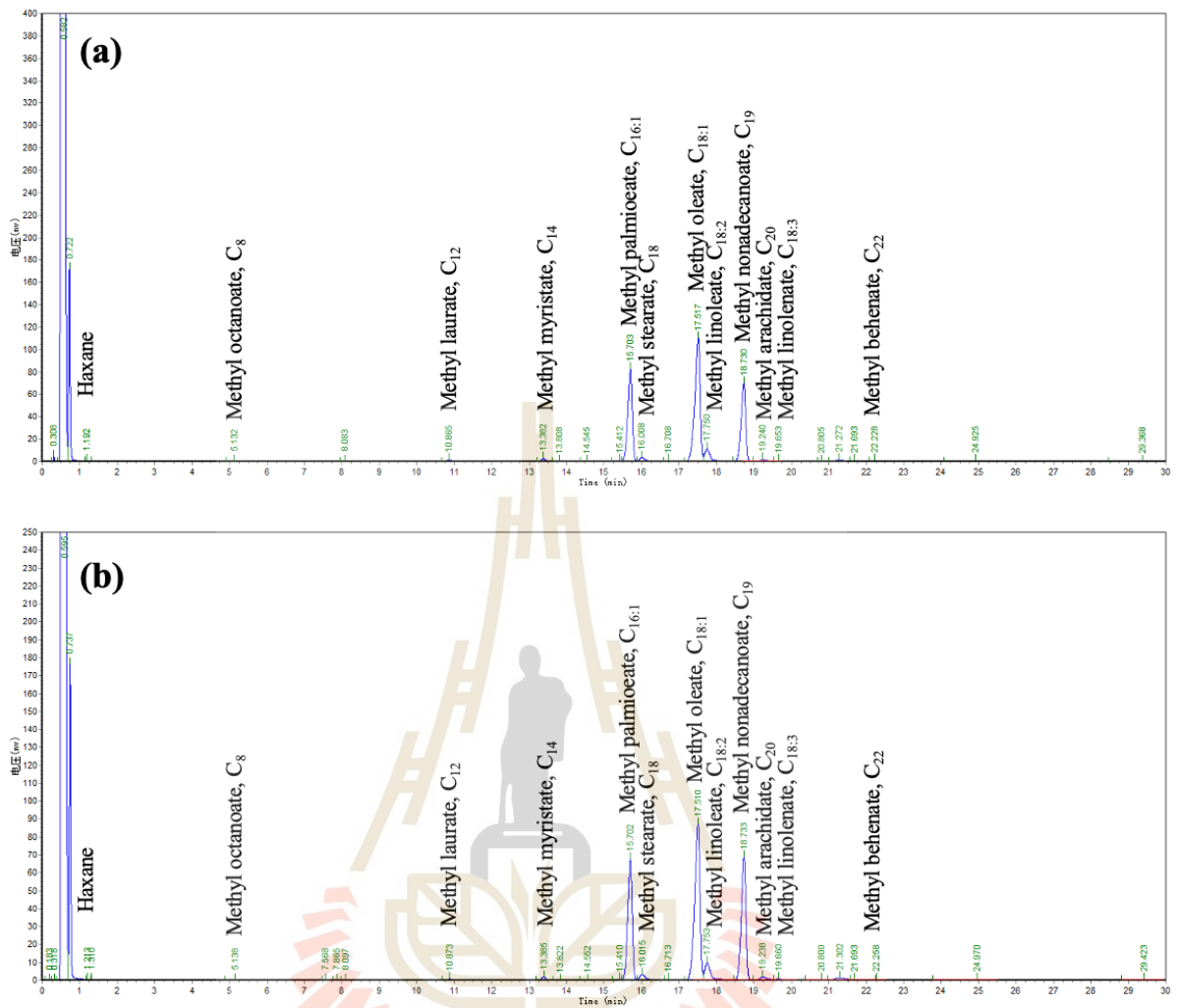


Figure B2 GC chromatogram of biodiesel products from transesterification of palm oil from K/NaY1.0 (a) duplicate of 1<sup>st</sup> run and (b) triplicate of 1<sup>st</sup> run.



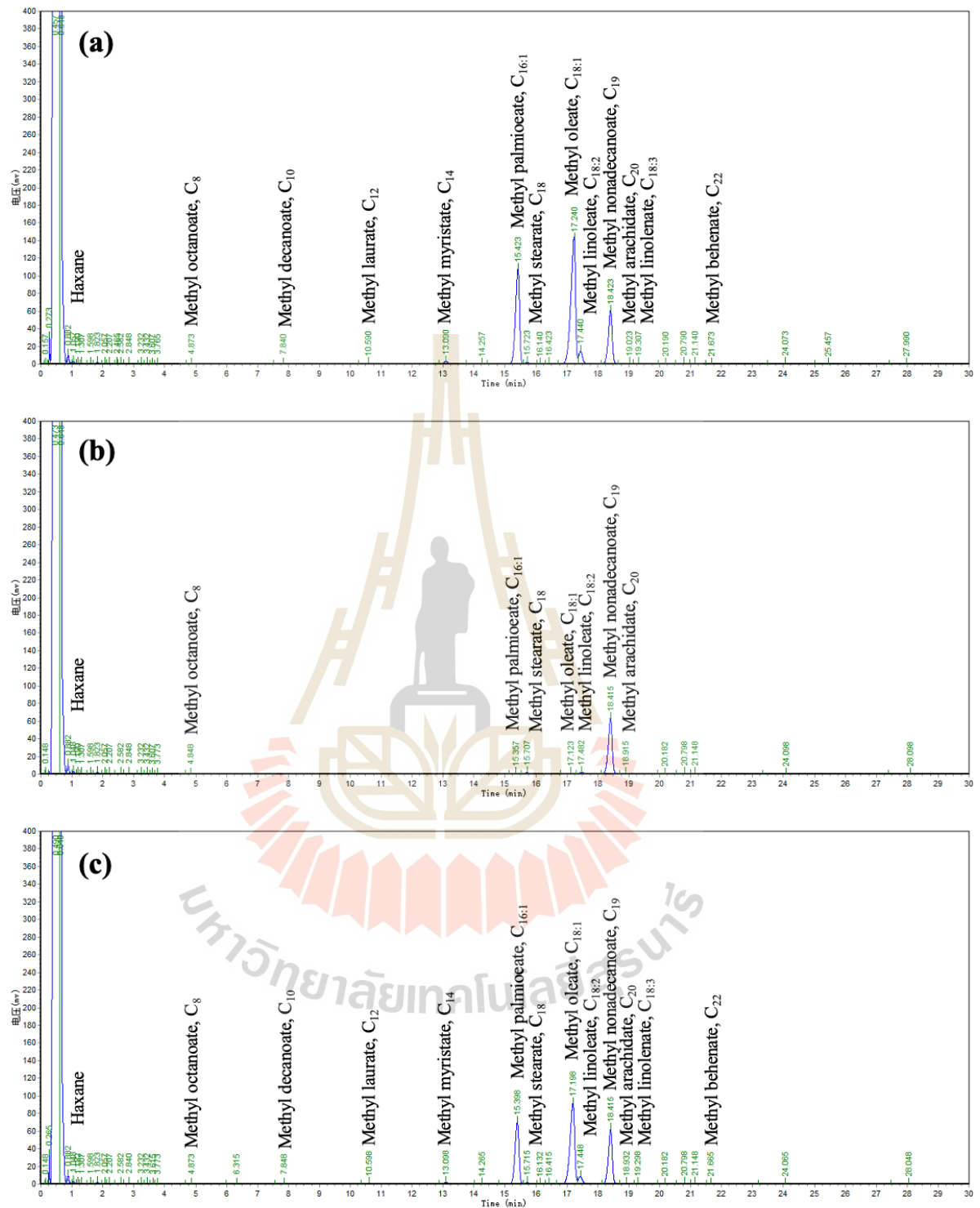
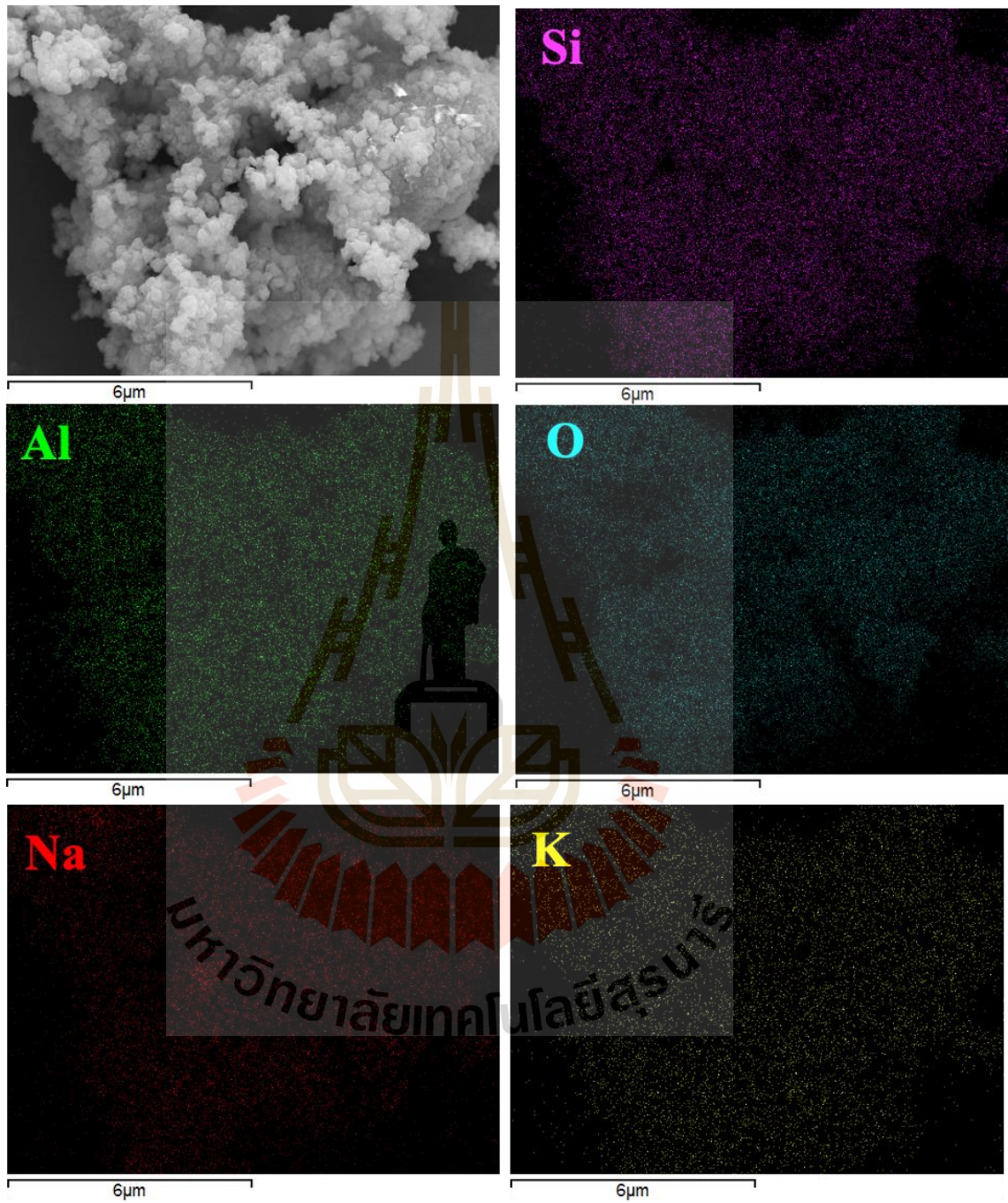


Figure B4 GC chromatogram of biodiesel products from leaching test from (a) K/NaY0.25, (b) K/NaY1.0, (c) K/NaY2.0.

## B.2 SEM images with EDX mapping and EDX spectra element analysis

Figure B5 SEM-EDS mapping of fresh  $K/NaY_{0.25}$ .

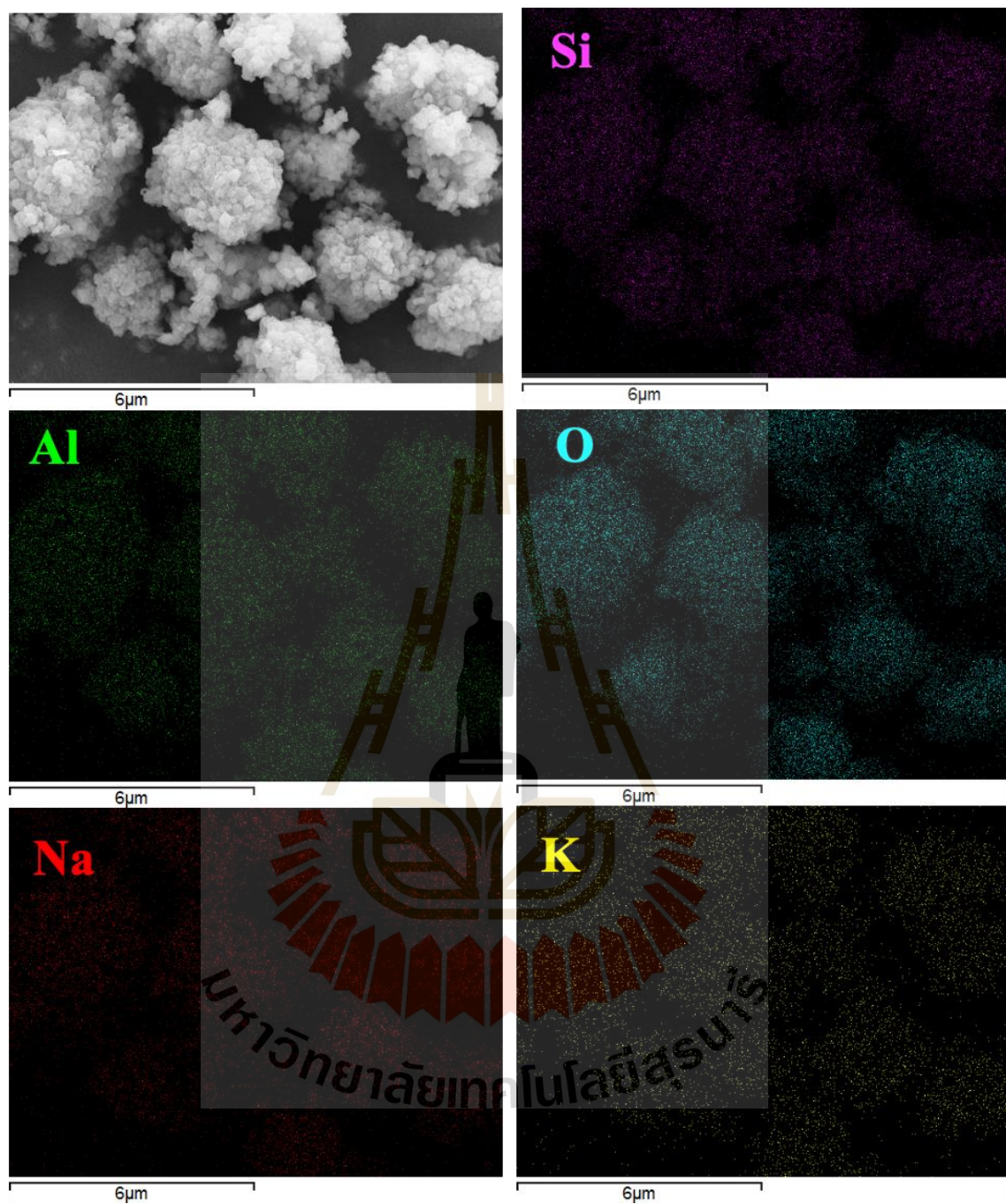


Figure B6 SEM-EDS mapping of spent K/NaY<sub>0.25</sub>.

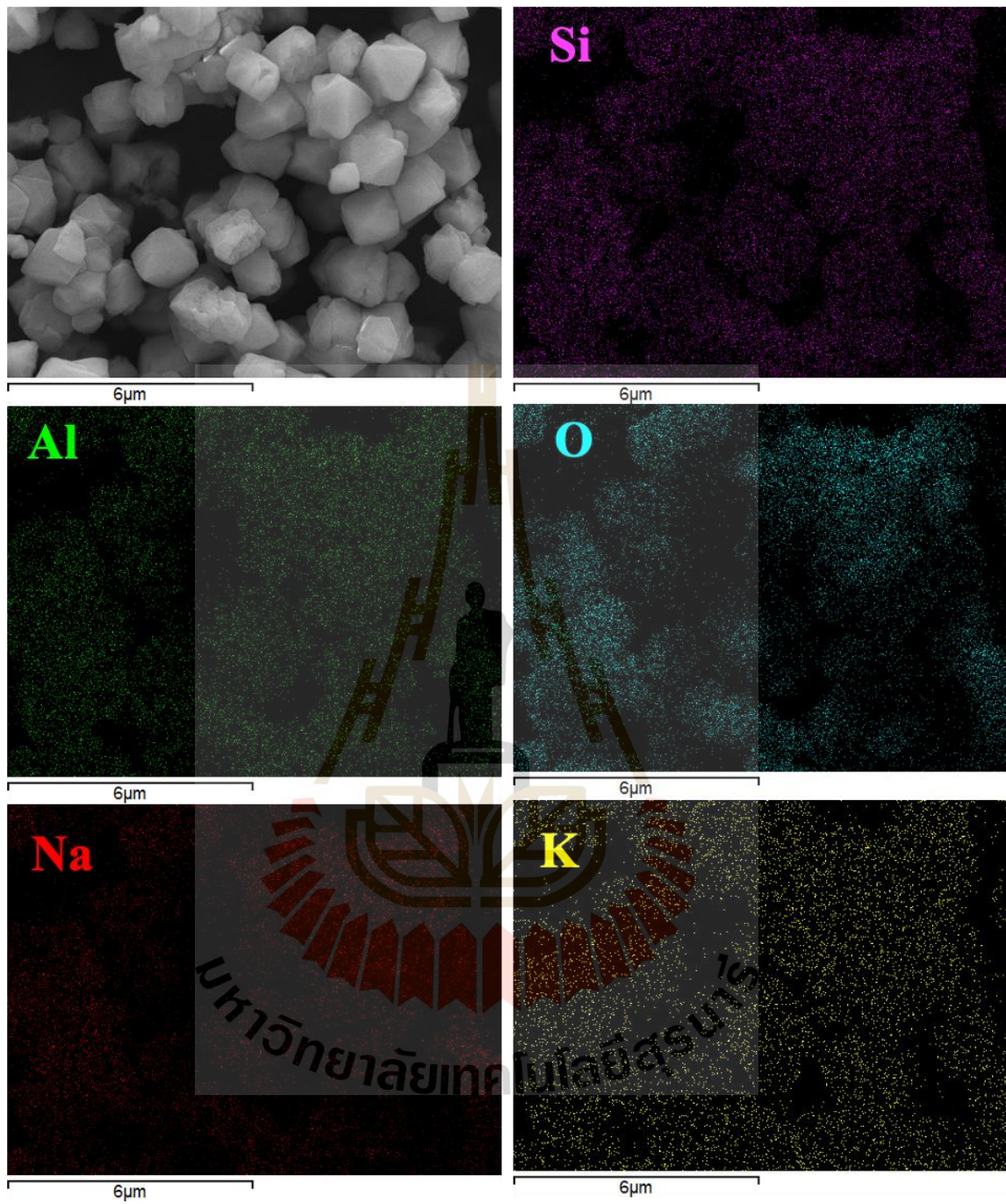
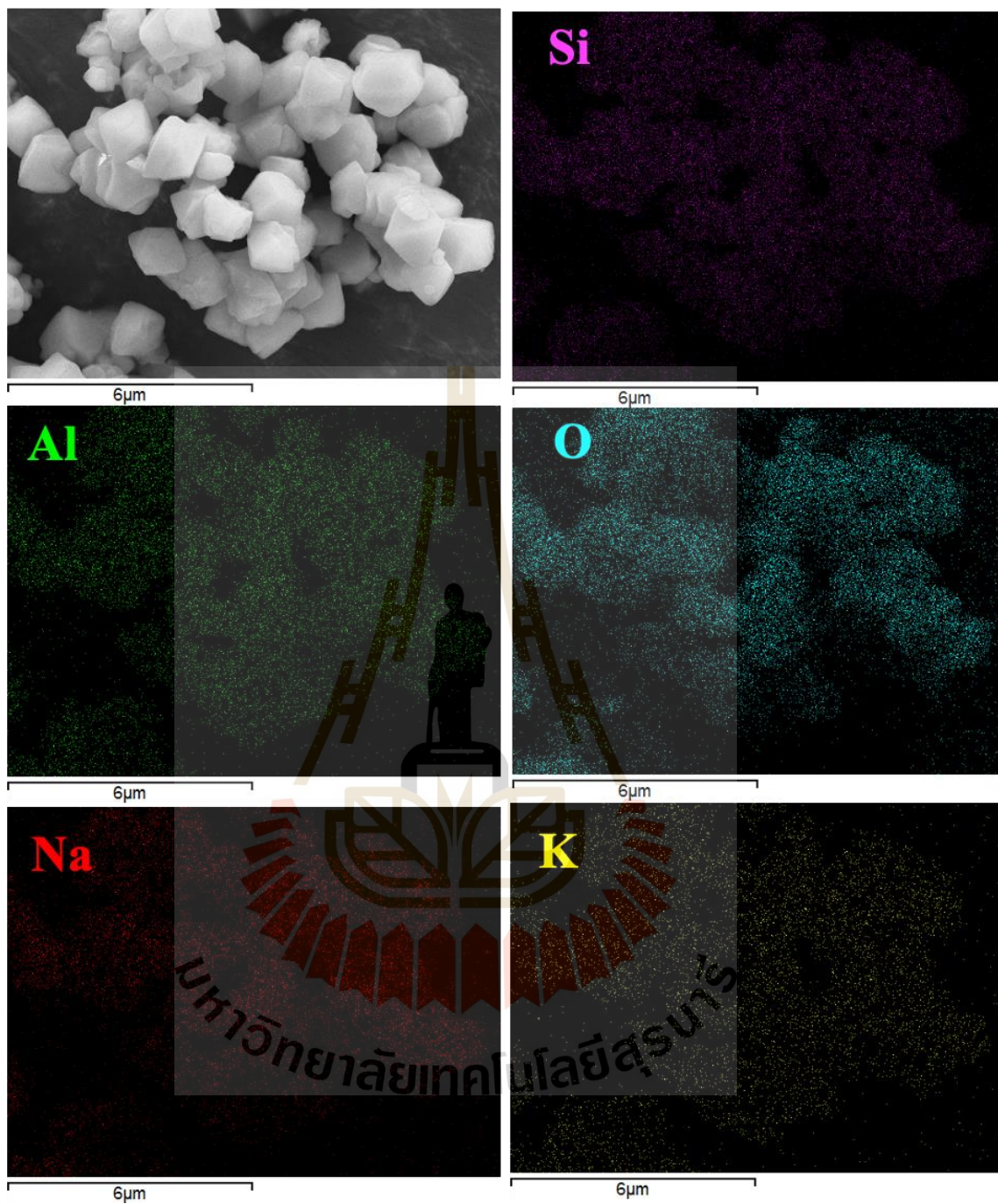


Figure B7 SEM-EDS mapping of fresh K/NaY1.0.



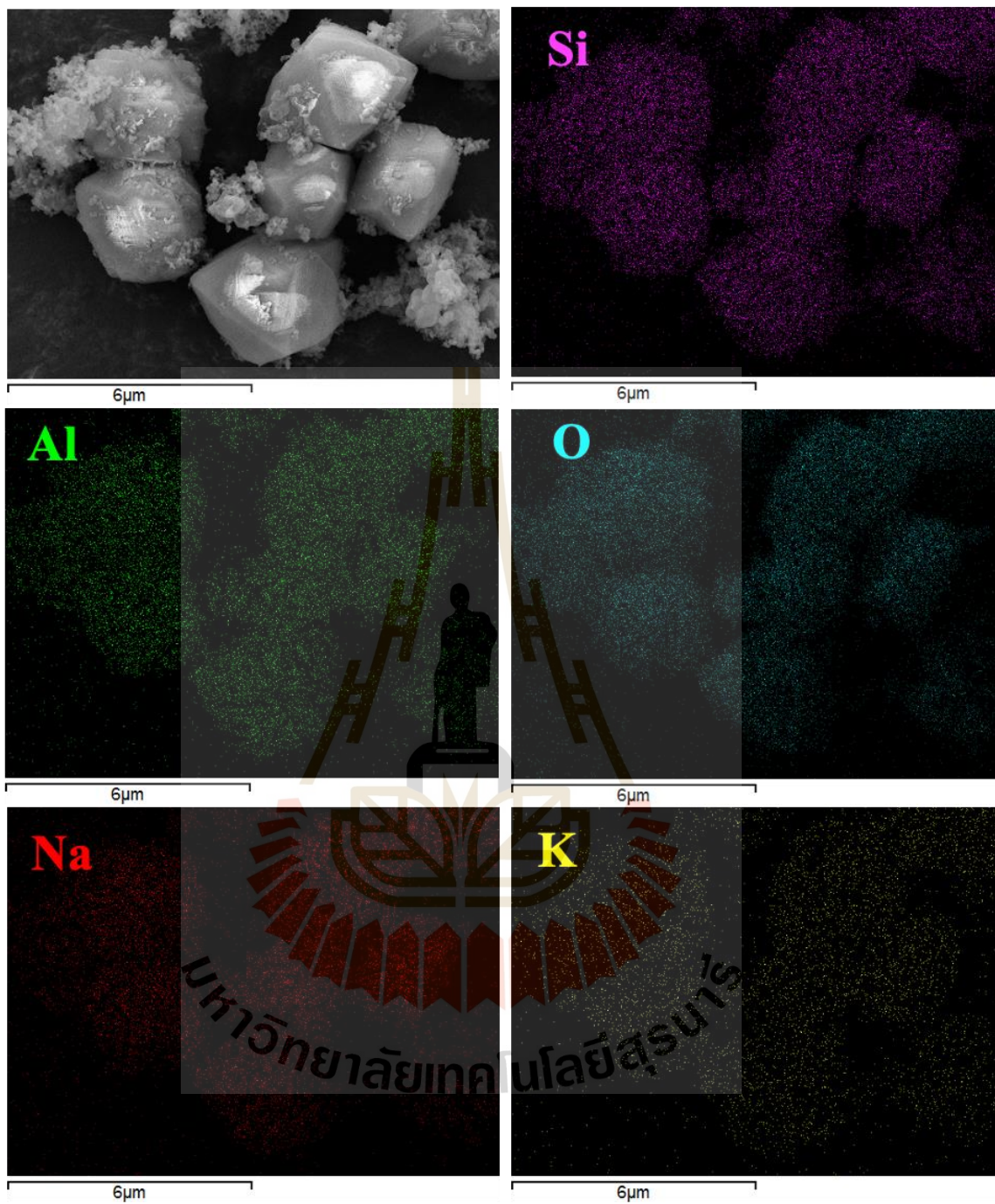


Figure B9 SEM-EDS mapping of fresh K/NaY<sub>2</sub>.O.

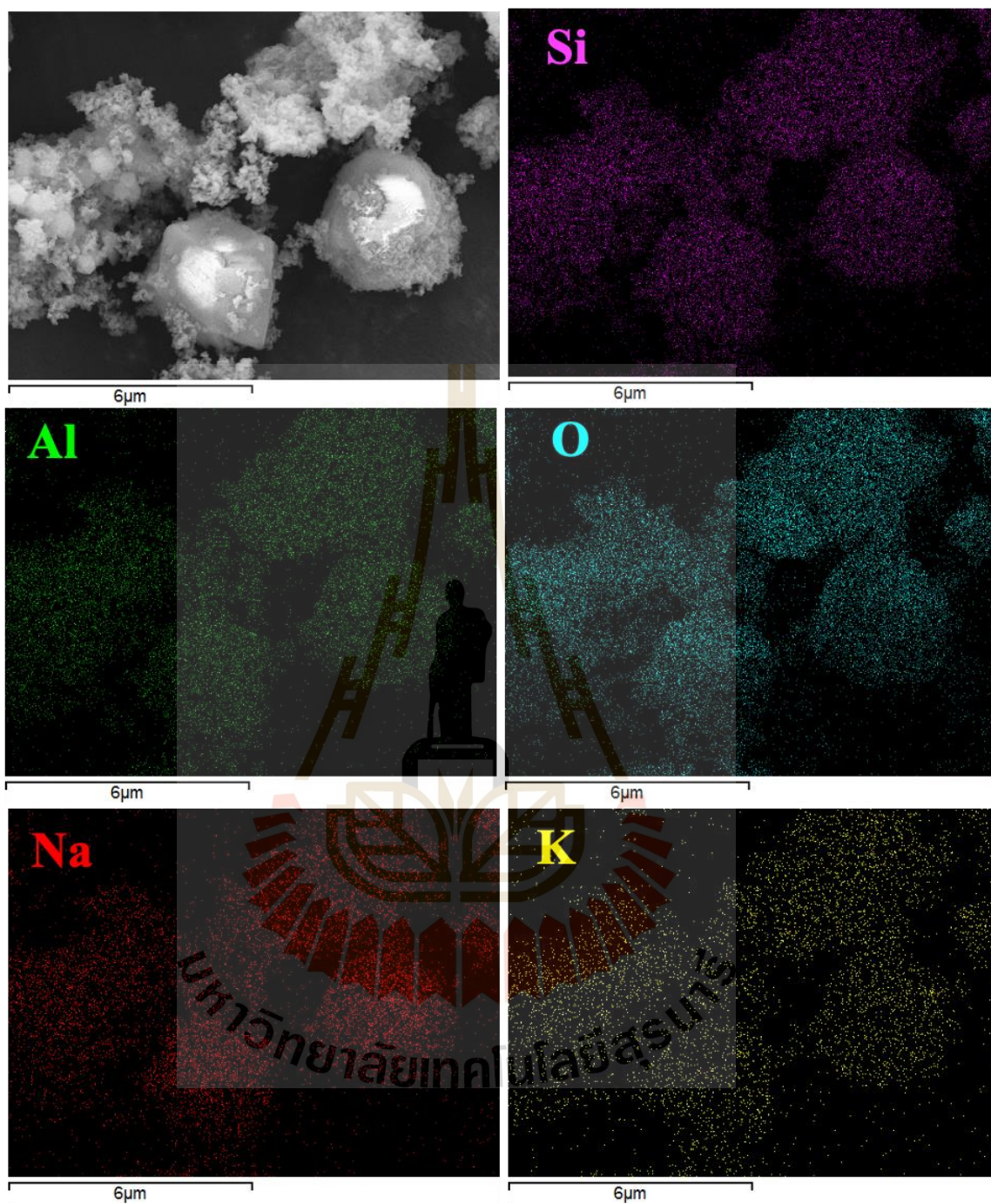


Figure B9 SEM-EDS mapping of spent K/NaY<sub>2</sub>.0.

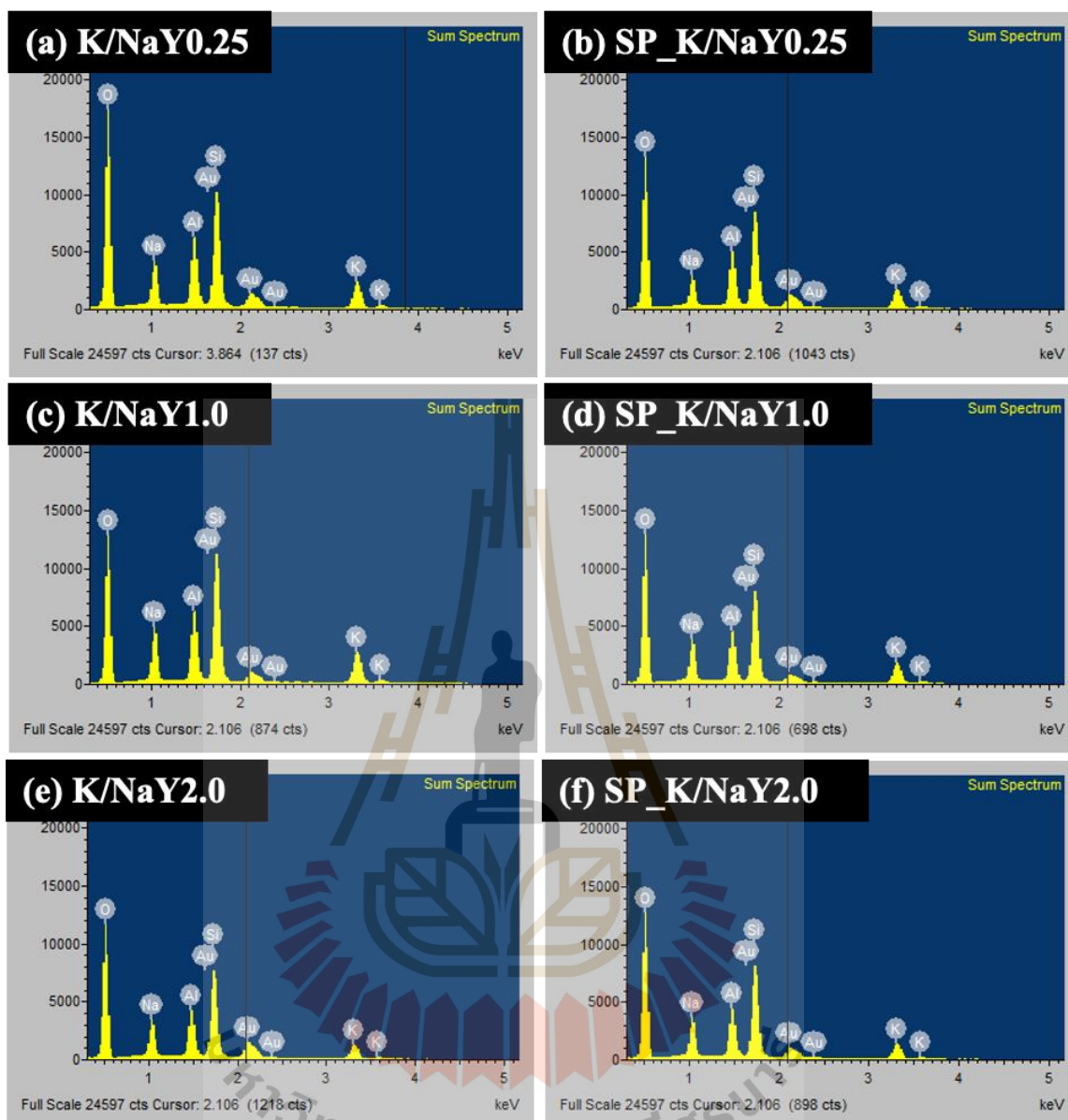


Figure B10 EDS analysis spectra of K/NaY including fresh and spent catalysts.

## CURRICULUM VITAE

**Name** Pakawan Sereerattanakorn

**Place of Birth** Ubon Ratchathani

### Education

2017 B.Sc. in Chemistry (First Class Honors), Ubon Ratchathani

2018 – 2024 Ph.D. student in Chemistry, Suranaree University of Technology, Institute of Science, Thailand

**Publication** Sereerattanakorn, P., Tayraukham, P., Osakoo, N., Krukkratoke, P., Keawkumay, C., Wittayakun, J., Pornnongsan, N., Deekamwong, K., and Prayoonpokarach, S. (2023). The Synthesis of Well-Dispersed and Uniform-Sized Zeolite NaY by Adding Non-Refluxed and Acid-Refluxed Cogon Grass. *Materials*, 16(23).

### Grants and Fellowships

2013 – 2023 Science Achievement Scholarship of Thailand (SAST)

### Position and Place of Work

2018 – 2023 Ph.D. student in Chemistry, Suranaree University of Technology, Institute of Science, Thailand

2023 Graduate research assistant at J.B. Speed School of Engineering, University of Louisville, USA, from May 1<sup>st</sup> to October 31<sup>st</sup>, under the supervision of Assoc. Prof. Dr. Noppadon Sathitsuksanoh